

# CHAPTER 3

## MICROWAVE DIAGNOSTICS

N. C. LUHMANN, Jr.\* *University of California, Davis, California*

H. BINDSLEV *Risø National Laboratory, Roskilde, Denmark*

H. PARK *Princeton Plasma Physics Laboratory, Princeton, New Jersey*

J. SÁNCHEZ *Euratom-Ciemat, 28040 Madrid, Spain*

G. TAYLOR *Princeton Plasma Physics Laboratory, Princeton, New Jersey*

C. X. YU *University of Science and Technology of China, Hefei, China*

Received October 6, 2006

Accepted for Publication March 23, 2007

*Microwave-based diagnostics have found broad application in magnetic fusion plasma diagnostics and are expected to be widely employed in future burning plasma experiments (BPXs). Most of these techniques are based directly on the dispersive properties of the plasma medium that, as shown in the body of the paper, results in the microwave/millimeter wave portion of the electromagnetic spectrum being particularly well suited for a variety of measurements of both magnetic fusion plasma equilibrium parameters and their fluctuations. Electron cyclotron emission provides a measurement of electron temperature and its fluctuations while electron cyclotron absorption potentially can provide a measurement of electron pressure (the product of electron density and temperature) as well as information on the suprathermal electron distribution. Electron Bernstein wave emission is also employed for electron temperature radiometric measurements in devices including reversed field pinches, spherical tori, and higher-aspect-ratio tokamaks and stellarators that operate at high  $\beta$ . The radar-based microwave reflectometry technique measures the electron density profile and its fluctuations by means of the reflection of electromag-*

*netic waves at the plasma cutoff layer. Coherent Thomson scattering in the microwave region yields information on the fast ion population. Wave number resolved microwave collective scattering is also widely employed for measuring nonthermal (turbulent) density fluctuations or coherent electrostatic waves. The approach taken in this review is to address each technique separately beginning with the physical principles followed by representative implementations on magnetic fusion devices. In each case, the applicability to future BPXs is discussed. It is impossible in a short review to capture fully the numerous significant accomplishments of the many clever scientists and engineers who have advanced microwave plasma diagnostics technology over many decades. Therefore, in this paper, we can reveal only the basic principles together with some of the most exciting highlights while outlining the major trends, and we hope it will serve as an exciting introduction to this rich field of plasma diagnostics.*

**KEYWORDS:** *microwave, plasma, diagnostics*

*Note: Some figures in this paper are in color only in the electronic version.*

### Contents—Chapter 3

- I. INTRODUCTION
- II. ELECTRON CYCLOTRON EMISSION/ABSORPTION
  - II.A. Introduction/Review
  - II.B. Theory
  - II.C. Detection Techniques
  - II.D. Calibration Techniques

- II.E. Modern Implementations
  - II.E.1. JT-60 ECE Systems
  - II.E.2. LHD ECE Systems
  - II.E.3. TEXTOR ECE Systems
  - II.E.4. RTP ECA Diagnostic
- II.F. Applicability to a BPX
- III. ELECTRON BERNSTEIN WAVE EMISSION
  - III.A. Introduction/Review
  - III.B. Modern Implementations
  - III.C. Applicability to a BPX

\*E-mail: ncluhmann@ucdavis.edu

- IV. REFLECTOMETRY
  - IV.A. Introduction
  - IV.B. Profile Measurements
    - IV.B.1. Profile Techniques and Implementation
  - IV.C. Fluctuation Measurements
  - IV.D. Doppler Reflectometry
  - IV.E. Applicability to a BPX
- V. COLLECTIVE THOMSON SCATTERING
  - V.A. Introduction
  - V.B. The Inhomogeneous Wave Equation for the Scattered Wave
  - V.C. The Equation of Transfer for a Scattering System
- VI. APPLICATION OF COLLECTIVE SCATTERING TO THE DIAGNOSIS OF MACROSCOPIC OR TURBULENT FLUCTUATIONS
  - VI.A. Wave Number ( $k$ )-Resolved Collective Scattering
    - VI.A.1. Theory
    - VI.A.2. Representative Collective Scattering Systems
  - VI.B. Far Forward Scattering
  - VI.C. Enhanced Scattering
  - VI.D. Cross-Polarization Scattering
- VII. APPLICATION OF COLLECTIVE SCATTERING TO THE DIAGNOSIS OF ION VELOCITY DISTRIBUTIONS THROUGH MEASUREMENTS OF MICROSCOPIC FLUCTUATIONS
  - VII.A. Introduction
  - VII.B. Electromagnetic Model of Microscopic Fluctuations
  - VII.C. Examples of CTS Spectra
  - VII.D. Signal-to-Noise Ratio
  - VII.E. Choice of Probe Frequency
  - VII.F. Assessing the Information Content in CTS Data
    - VII.F.1. The Global Signal-to-Noise Ratio
    - VII.F.2. Nuisance Parameters and Parameters of Interest
    - VII.F.3. Features in the Velocity Distribution That Can Be Resolved
    - VII.F.4. The Resolving Power, A Measure of Information
    - VII.F.5. Practical Examples
- VIII. FAST WAVE INTERFEROMETRY AND REFLECTOMETRY
  - VIII.A. Introduction/Review
  - VIII.B. Examples of Implementations
  - VIII.C. Applicability to a BPX
- IX. IMAGING AND VISUALIZATION DIAGNOSTICS
  - IX.A. Introduction
  - IX.B. Electron Cyclotron Emission Imaging
  - IX.C. Microwave Imaging Reflectometry
  - IX.D. Simultaneous ECEI/MIR System
  - IX.E. Applicability to a BPX
- X. SUMMARY AND OUTLOOK

## I. INTRODUCTION

The microwave/millimeter wave portion of the electromagnetic spectrum is ideally suited for performing a variety of measurements of both magnetic fusion plasma equilibrium parameters and their fluctuations. This is readily seen from, for example, the TEXTOR tokamak characteristic frequencies plotted in Fig. 1, where the abscissa represents the plasma major radius dimension. A detailed description of the so-called characteristic modes may be found in Ref. 1. Basically, in the case of microwave diagnostics, we are most often concerned with the

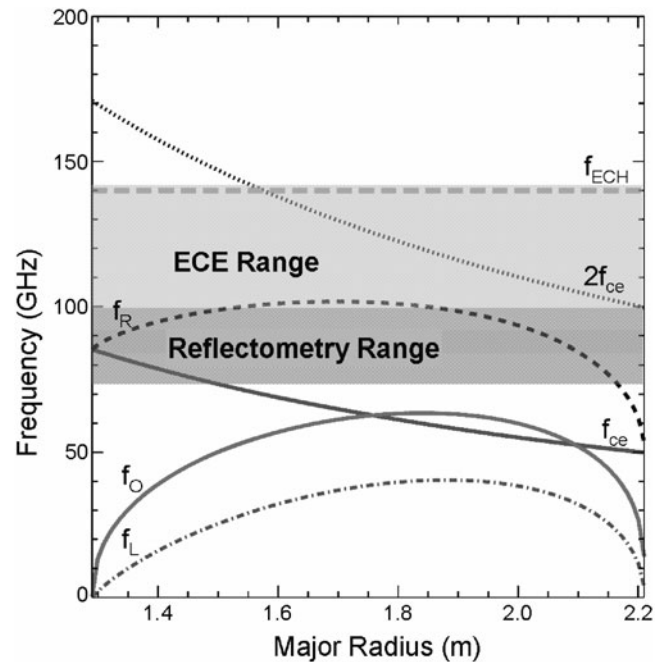


Fig. 1. Characteristic frequencies for the TEXTOR tokamak.

response of the electrons (the ions are massive) to electromagnetic waves propagating transverse to a steady magnetic field  $B_0$ .<sup>a</sup> For E-field polarization parallel to  $B_0$ , the mode is referred to as O-mode with a cutoff frequency  $f_O$  equal to the electron plasma frequency. The case of E-field polarization perpendicular to  $B_0$  is referred to as X-mode and has cutoff frequencies given by  $\omega_{L,R} = (\omega_{ce}/2) \pm ((\sqrt{\omega_{ce}^2 + 4\omega_{pe}^2})/2)$ , where the plus (minus) sign is associated with the so-called R-wave (L-wave) cutoff.<sup>1</sup> Here,  $\omega_{pe} = (4\pi n_e e^2/m_e)^{1/2}$  is the electron plasma frequency, and  $\omega_{ce} = |e| \cdot B/m_e c$  is the electron cyclotron frequency.

Referring to Fig. 1, it is seen that reflectometry (customarily conducted using X-mode at the R-wave cutoff as indicated in Fig. 1 or alternatively O-mode at the plasma cutoff; see Secs. IV and IX) extends from  $\sim 70$  to 100 GHz. For electron cyclotron emission (ECE) measurements (see Secs. II and IX.B) the second harmonic of the electron cyclotron frequency is usually employed, which corresponds to 100 to 170 GHz for TEXTOR. Figure 1 plot also reveals a common problem faced by microwave diagnostics. Specifically, high-power (megawatt-level) electron cyclotron resonance (ECRH) heating (ECRH) power is often employed, which necessitates the use of notch (band rejection) filters in diagnostic systems to protect the detectors from stray ECRH power.<sup>2</sup>

In the case of TEXTOR, the ECRH frequency is 140 GHz, which falls within the region used for ECE

<sup>a</sup>An exception is the case of fast wave interferometry/reflectometry (Sec. VIII).

measurements. In the case of diagnostics such as interferometry, polarimetry, and collective scattering, the need to avoid cutoffs as well as to minimize problems such as beam refraction and diffraction argues for the use of operating frequencies into the THz region although there are competing concerns that result in compromises. Since the principles of many of these techniques depend upon the properties of the anisotropic dielectric medium, the reader is directed to the many excellent references on plasma waves.<sup>1,3-8</sup>

An overview of the plasma parameters that can be measured with the use of microwave diagnostics instrumentation is given in the parameter/technique matrix in Table I.

## II. ELECTRON CYCLOTRON EMISSION/ABSORPTION

### II.A. Introduction/Review

In magnetized plasmas, the gyromotion of electrons results in plasma radiation at the electron cyclotron frequency  $\omega_{ce} = eB/\gamma m_e$  and its harmonics.<sup>9,10</sup> Here,  $B$  is the magnetic field strength,  $e$  is the electron charge,  $m_e$  is the kinetic electron mass, and  $\gamma$  is the familiar Lorentz relativistic factor. When the plasma density and temperature are sufficiently high, the plasma becomes optically thick to some harmonics of the ECE, usually, the first-harmonic ordinary mode and the second-harmonic extraordinary mode.<sup>10-13</sup> Emission from plasmas of magnetic fusion interest is in the Rayleigh-Jeans limit ( $\hbar \ll kT_e$ ) so that the radiation intensity of optically thick ECE harmonics reaches that of blackbody radiation, i.e.,

$$I(\omega) = \omega^2 kT_e / (8\pi^3 c^2) . \tag{1}$$

Therefore, the plasma electron temperature and its fluctuations can be determined by measuring the intensity of ECE. In addition, under the proper conditions, ECE measurements may be employed to determine electron density and its fluctuations in tokamaks as investigated by a number of authors.<sup>14-19</sup>

For contemporary magnetic fusion devices such as tokamaks and stellarators, the magnetic field ranges from  $\cong 2$  to 8 T, so that the ECE radiation is in the millimeter-wave range ( $\cong 50$  to 500 GHz). For these devices, it is seen that the ECE frequency is a monotonically decreasing function of plasma radius toward the outboard side (see Fig. 1), originating from the magnetic configuration of tokamaks, in which the magnetic field strength depends on the plasma minor radius as

$$B(r) = B_0 R_0 / (R_0 + r) , \tag{2}$$

where  $R_0$  and  $r$  are the major radius and minor radius of the tokamak, respectively. In a typical ECE radiometer, a horn antenna receives the ECE radiation at the outboard side, which is separated into different frequency bands,

TABLE I  
Parameter/Technique Matrix for Microwave Plasma Diagnostics

	Electron Density (Profile)	Electron Density Fluctuations	Electron Temperature (Profile)	Electron Temperature Fluctuations	Ion Temperature	Fast Ion Population	Ion Species Mix	Electron Pressure	Suprathermal Population	Plasma Rotation	Magnetic Fluctuations	Described in
Electron cyclotron emission Electron cyclotron absorption Electron Bernstein wave emission Reflectometry Collective Thomson scattering Fastwave interferometry and reflectometry	⊕ ⊕	⊕	● ⊕ ●	●	⊕	●		●	⊕ ◆	⊕		Secs. II and IX.B Sec. II Sec. III Secs. IV and IX.C Sec. VI (fluctuations) and VII (fast ions) Sec. VIII

\* ● = Primary technique, is well suited to the measurement; ◆ = backup technique, provides similar data to the primary but has some limitations; ⊕ = supplementary technique, can provide data that can be used to improve or check aspects of the main measurement but is not complete in itself.

each corresponding to a particular horizontal location in the plasma. Thus, time-resolved one-dimensional (1-D)  $T_e$  profiles can be obtained. As is discussed in Sec. IX.B, in recent years there has been a move toward the use of 1-D imaging detector arrays to provide two-dimensional (2-D) images of temperature fluctuations.<sup>20,21</sup>

The first ECE measurements from a tokamak were performed on the CLEO device using a Michelson interferometer and InSb detector<sup>22</sup> with early theoretical studies providing a sound foundation for measurement and interpretation.<sup>23,24</sup> This was rapidly followed by measurements on devices throughout the world. Today, this is a routine technique for obtaining electron temperature profiles using a variety of instrument configurations.<sup>25,26</sup>

## II.B. Theory

For propagation with wave vector  $\vec{k} \perp \vec{B}$ , the emission is linearly polarized and occurs in both the O-mode and X-mode polarization directions. The differential radiation transport for a single-ray trajectory is determined by the balance between emission and absorption<sup>4,27,28</sup>

$$\frac{d}{ds} \left[ \frac{I(\omega)}{N_r^2} \right] = \frac{1}{N_r^2} [-\alpha(\omega)I(\omega) + j(\omega)] , \quad (3)$$

where

$\alpha(\omega)$  = absorption coefficient

$j(\omega)$  = emission coefficient

$N_r$  = plasma refractive index

$I(\omega)$  = emission intensity.

Integrating from the emission location to the observation position, we have

$$I_{(s)}(\omega) = I_{(s_0)}(\omega) \exp(-\tau_s) + \frac{j(\omega)}{\alpha(\omega)} [1 - \exp(-\tau_s)] , \quad (4)$$

where the optical depth is given by

$$\tau_s = \int_0^s \alpha(\omega) ds . \quad (5)$$

For  $\tau_s \gg 1$ , we have

$$I(\omega, s) = \frac{j(\omega)}{\alpha(\omega)} . \quad (6)$$

In the case of optically thin or “grey” emission, the wall reflections must be taken into account, leading to the following expression<sup>29</sup>:

$$\begin{aligned} I(\omega, T_e) &= I_{BB} \frac{(1 - e^{-\tau})}{(1 - \rho_{refl} e^{-\tau})} \\ &= \frac{\omega^2}{8\pi^3 c^2} k_B T_e \frac{(1 - e^{-\tau})}{(1 - \rho_{refl} e^{-\tau})} . \end{aligned} \quad (7)$$

For the case of X-mode normal emission in the equatorial plane with  $n \geq 2$ , the optical depth in a circular plasma is given by<sup>30</sup>

$$\tau_n^x = 9.5 \times 10^{12} \frac{(R_0 + r)^2 n_e [n^{2n-2} (9.78 \times 10^{-4} T_e)^{n-1}]}{10 R_0 B_\phi(R)(n-1)!} , \quad (8)$$

where

$R_0$  = major radius

$r$  = radial position ( $-a \leq r \leq a$ ) (cm)

$T_e$  = electron temperature (keV)

$n_e$  = electron density ( $\text{cm}^{-3}$ )

$B$  = magnetic field (T)

$n$  = harmonic number.

For the fundamental O-mode emission, the optical depth is given by

$$\begin{aligned} \tau_{n=1}^O &= 9.8596 \left[ \frac{1.16 \times 10^4 k_B T_e}{m_e c^2} \right] \left[ \frac{R_0 \omega_{ce}}{2\pi c} \right] \\ &\times \frac{\omega_{pe}^2}{\omega_{ce}^2} \sqrt{1 - \frac{\omega_{pe}^2}{\omega_{ce}^2}} , \end{aligned} \quad (9)$$

where  $\omega_{pe}$  is the electron plasma frequency.

Other potential complicating effects such as harmonic overlap, relativistic broadening and downshifts, polarization scrambling, and nonthermal populations can occur and are discussed in the literature.<sup>14,15,31-33</sup> In the case of relativistic downshifts, the effect has been suggested as a means of measuring the electron density distribution.<sup>14,15</sup> Here, the relativistic frequency shift is observed using optically thick ECE measurements from the high field side (HFS) together with the low field side (LFS) ECE derived electron temperature profile to obtain the electron density from the frequency shift.

The relativistic Doppler resonance effect is also employed in oblique viewing ECE instruments as a means of probing the electron distribution function.<sup>17,34,35</sup> One proposed use of an oblique view ECE system is to minimize relativistic broadening, which has the desirable consequence of reducing the frequency overlap between second- and third-harmonic ECE (Ref. 36). Here, Sato and Isayama report that in reactor plasmas, oblique viewing will permit second-harmonic, X-mode ECE

measurements up to 24 keV and fundamental, O-mode measurements up to 50 keV.

Recently, an oblique view ECE system has been developed for the JET tokamak where the ECE radiation is detected along lines of sight at a small angle rather than the standard perpendicular view with the aim of probing the low-energy portion of the electron distribution function since departures from a Maxwellian shape have been suggested as the source of the systematic disagreements observed under some conditions between ECE and Thomson scattering diagnostics in JET as well as TFTR (Ref. 37). Specifically, analysis of JET data suggests that in the presence of strong auxiliary heating, the assumption of a Maxwellian bulk distribution may not be justified.<sup>32,38</sup> Earlier measurements of ECE on the FTU device using an oblique viewing system were reported to be consistent with theoretical Fokker-Planck calculations, showing the existence of a deformation of the bulk of the electron distribution function during on-axis ECRH applied on the current ramp-up phase of the discharge.<sup>39</sup>

The new JET oblique view system utilizes two lines of sight at  $\sim 10$  and  $20$  deg, respectively, in the toroidal direction with respect to the perpendicular to the magnetic field permitting the investigation of this issue.<sup>40</sup> The oblique view system employs two of the six newly installed waveguides, arranged in a cluster of  $3 \times 2$  (horizontal  $\times$  vertical). As shown schematically in Fig. 2, the configuration essentially consists of an open-ended circular waveguide whose beam is tilted in the toroidal direction ( $\varphi \sim 10$  and  $20$  deg) by employing a combination of fixed mirrors, where the size of the final beam is controlled by making the last mirror ellipsoidal.<sup>41</sup> A new fast scanning Michelson interferometer (see Sec. II.C) permits the simultaneous measurement of the ECE spectrum at different angles (including  $\varphi \sim 0$  deg) with different polarizations (O-mode and X-mode). This covers the spectral region from 70 to 800 GHz with a spectral resolution of 8.5 GHz and a capability of acquiring a complete spectrum in 9 ms (Ref. 42).

As noted above, since 1974, ECE radiometers have been utilized to measure plasma electron temperature

profiles. In addition, they have been used to measure large amplitude fluctuations such as sawtooth oscillations.<sup>43,44</sup> However, information regarding small amplitude, turbulent temperature fluctuations was not available until 1993, when the intensity interferometric technique was first applied.<sup>45,46</sup> This is due to the coarse temperature resolution limit determined by the intrinsic radiation noise, which is given by

$$\Delta T_{\text{rms}} = (T_e + T_n) / \sqrt{\Delta\omega\tau} ,$$

where

$T_e$  = electron temperature to be measured

$T_n (\ll T_e)$  = overall noise temperature including the antenna contribution

$\Delta\omega$  = bandwidth of the radiation to be collected

$\tau$  = integration time.<sup>27</sup>

For a typical ECE radiometer, the bandwidth is designed to be  $\sim 0.5$  GHz based on spatial resolution considerations; thus, the relative temperature resolution limit is  $\sim 1$  to 3% with a frequency response of 250 kHz. As the relative fluctuation amplitude of microturbulence is typically  $< 1\%$ , the intrinsic radiation noise of an ECE radiometer usually predominates.

The intensity interferometric techniques overcome these difficulties and enable, under certain conditions, the root-mean-square (rms) values of turbulent  $T_e$  fluctuations to be measured.<sup>45,46</sup> The main requirement is to obtain two signals, which have uncorrelated thermal fluctuations, or radiation noise. This decorrelated intrinsic noise can then be averaged out in statistical analysis to reveal the usually smaller plasma  $T_e$  fluctuations due to plasma instabilities, as the latter have different coherence properties from the thermal fluctuations. This is achieved by determining the cross coherence of the two signals<sup>47</sup>

$$\Gamma_{12}(\tau) = \overline{\tilde{S}_1(t)\tilde{S}_2(t+\tau)} \approx c_1 c_2 \overline{\tilde{T}_{e1}(t)\tilde{T}_{e2}(t+\tau)} , \quad (10)$$

where  $c_1$  and  $c_2$  are constant sensitivity coefficients of the detection system channels. If the two signals originate from the same plasma volume,  $T_{e1} = T_{e2}$ , so that local values of  $\tilde{T}_e$  can be obtained. If the two signals emanate from poloidally or radially separated plasma volumes, the poloidal or radial wave number spectra and correlation lengths can be measured.

Thus far, the discussion has focused exclusively on the emission process; however, measurements of electron cyclotron absorption (ECA) also provide valuable information on the electron distribution function.<sup>48-51</sup> The basic principles can be understood by examination of Eq. (7). First, it is apparent that when the large  $\tau$  approximation is not valid, an explicit knowledge of  $\tau$  is required for a determination of  $T_e$ . This problem is addressed

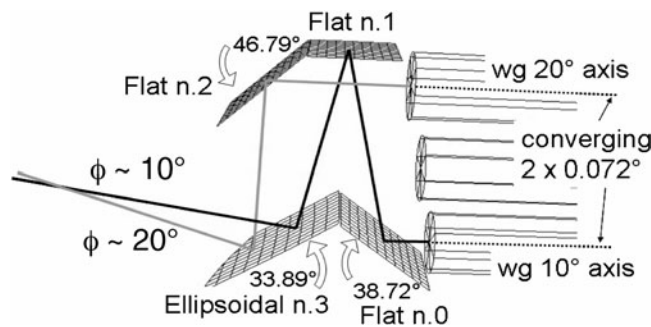


Fig. 2. Optical configuration for JET oblique viewing ECE system. (From Ref. 41)

using the ECA measurement, wherein one measures the fraction of microwave power transmitted through the plasma, thereby determining the optical depth  $\tau$ :

$$P_{trans} = P_{inc} \exp(-\tau) . \quad (11)$$

In the case of the second-harmonic X-mode, as seen from Eq. (8), the optical depth is proportional to the product of the electron density and temperature (i.e., the electron pressure). Consequently, one has a single diagnostic measurement of electron pressure as well as an electron temperature measurement using an independent measurement of electron density. This ECA technique has other diagnostic capability. Specifically, the presence of a population of fast suprathermal electrons in combination with a small optical depth leads to inaccuracies in electron temperature determination. Here, one makes use of the fact that the contribution to the optical depth by a suprathermal population is negligibly small. Consequently, the ECA measurement of electron pressure is relatively insensitive to the existence of suprathermals,<sup>30,50</sup> and in this situation the electron temperature can be determined using the ECA determined pressure together with independent electron density measurements. On the other hand, given independent knowledge of the electron density and temperature, ECA may be employed to measure the suprathermal electron distribution.<sup>49</sup>

## II.C. Detection Techniques

There have essentially been three detection approaches that have been employed in ECE measurements:

1. Fourier transform spectrometer (FTS)
2. Grating polychromator (GPS)
3. Heterodyne ECE receiver (HRS).

In the following, we briefly review the operating principles of each technique.

The first ECE measurements employed Fourier transform spectroscopy.<sup>52</sup> Figure 3 illustrates the configuration. Here, the ECE radiation emerged from the CLEO tokamak into a two-beam polarization-type Michelson interferometer<sup>53</sup> where the interferometer mirrors in one of the arms were scanned over a path difference of 10 mm in 10 ms, thereby resulting in wide frequency coverage albeit at a sacrifice in temporal resolution.<sup>29</sup> Detection was via a cooled (4.2 K) InSb detector [noise equivalent power (NEP) =  $10^{-12}$  W/Hz<sup>1/2</sup>]. Since the detector output is a voltage proportional to the radiation intensity, the spectrometer voltage output is given by

$$V'(x) = \int_0^{\infty} 2S(k) \cos(\pi kx) dk , \quad (12)$$

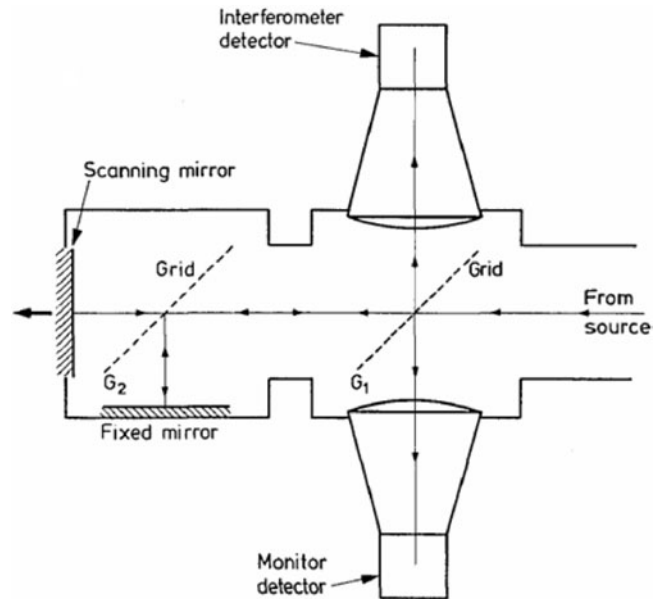


Fig. 3. Rapid-scanning Fourier spectrometer for time-resolved electron cyclotron spectral emission measurements on tokamak plasmas. (From Ref. 22)

where

$V'(x)$  = interferometer function

$x$  = mirror displacement

$S(k)$  = form factor for the emission spectrum that is obtained by digitizing the spectrum and performing a fast Fourier transform of the interferogram.

The spectral resolution is determined by the total scan distance and was 37.5 GHz for these first measurements. Other systems have employed a scanning Fabry-Perot interferometer in place of the Michelson interferometer.<sup>54,55</sup> It should be noted that the FTS technique has a multiplex and a throughput advantage over the other techniques (particularly GPS) in that it can be more easily calibrated with weak sources because all frequencies are measured at all times and the apertures are large and circular.<sup>56</sup>

Improved temporal resolution (as compared with the scanning Michelson interferometer approach) is obtained by use of a multichannel grating polychromator configuration.<sup>57,58</sup> Here, a grating is employed to disperse the ECE radiation onto a number of separate detectors. In the PLT tokamak implementation, the Maryland group<sup>57</sup> achieved fast time resolution ( $\cong 1 \mu s$ ) together with good spectral resolving power ( $\Delta f/f \cong 0.5$ ) using a grating instrument.<sup>57-59</sup>

In the heterodyne ECE approach, one or two levels of heterodyne down conversion are employed<sup>11,13,31,60</sup> to convert the high-frequency signals to a convenient

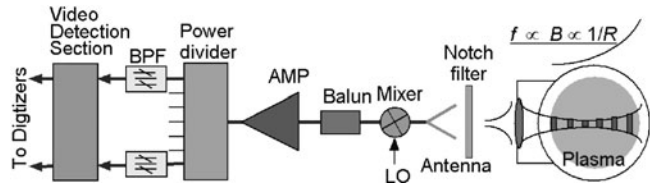


Fig. 4. Schematic of a heterodyne ECE radiometer for a tokamak.

intermediate frequency (IF) for subsequent amplification and signal processing. Of the three ECE measurement techniques, this yields the highest sensitivity and frequency resolution as well as offering the fastest temporal response. The limitation, compared to the other two approaches, concerns the bandwidth or frequency coverage, which is typically limited to a waveguide band or less, thereby dictating the need for a number of receivers to provide the needed spatial coverage. Figure 4 contains a schematic of a typical implementation, where it should be noted that advances in heterodyne receiver technology have made possible implementations at frequencies up to  $\approx 3$  THz, which is relevant for ITER where the ECE spectrum can extend to THz.

#### II.D. Calibration Techniques

In order to provide accurate electron temperature profiles, the ECE receiving system (antennas, transmission lines, detectors, etc.) must be absolutely calibrated. The standard approach is to employ large aperture (to fully illuminate the receiver antenna) black-body sources.<sup>61,62</sup>

More recently, by ramping the toroidal field and detecting coherent features in the measurement spectrum due to small errors in the calibration, researchers at the JET tokamak have been able to reduce the residual systematic, frequency errors in the absolute calibration ( $\approx 5$  to 10% level), thereby improving the relative accuracy.<sup>63,64</sup> Application of this technique has improved both the smoothness and the symmetry of the  $T_e$  profiles.<sup>63</sup>

#### II.E. Modern Implementations

In this section, we consider some representative modern implementations of ECE instruments. Because of length limitations, we have restricted the detailed instrument description to the ECE systems installed on the JT-60 tokamak. This is followed by a brief summary of the parameters of several systems on other devices together with references containing more detailed descriptions.

##### II.E.1. JT-60 ECE Systems

The ECE systems on the JT-60 tokamak, which is located at the Japan Atomic Energy Research Institute

TABLE II  
Specifications of the JT-60 ECE Systems

	FTS	GPS	HRS
Time resolution (maximum)	$\approx 25$ ms	$20 \mu\text{s}$ ( $2 \mu\text{s}$ )	$20 \mu\text{s}$ ( $2 \mu\text{s}$ )
Frequency region (GHz)	100 to 800	100 to 300	176 to 188
Frequency resolution (GHz)	3.66	1.3 to 2	0.5
Spatial resolution ( $B_t = 4$ T)	5.6 cm	2.0 cm	1.2 cm
Number of channels	512	20	12
Calibration	Absolute	Relative	Relative

in Japan, are a good example of a modern implementation. All three types of detection are employed.<sup>62,65–68</sup> Table II lists the specifications of the three separate instruments. An inspection of Table II reveals their different characteristics.

The ECE radiation emerges from two antennas located 60 deg apart in the toroidal direction and is transmitted into the diagnostic room through a 40-m-long transmission system (nominal 11-dB loss) comprising 63.5 mm diameter, low loss corrugated waveguide,<sup>69,70</sup> and smooth-wall rectangular waveguides (WR-284). The radiation enters the FTS, GPS, and HRS instruments after having been split using two power dividers. Stray ECRH power ( $f = 110$  GHz) is rejected by means of a high pass filter (60-dB rejection at 110 GHz). In order to prevent spurious ECE radiation from entering the GPS, grating lowpass filters<sup>71</sup> are installed in the GPS transmission line. All three systems employ second-harmonic ECE ranging from 100 to 300 GHz.

A schematic diagram of the 20-channel grating polychromator system is illustrated in Fig. 5 (Ref. 65), where the frequency difference between adjacent channels is typically 4 GHz when the toroidal field is 4 T. ECE radiation from JT-60 is first dispersed by a cross Czerny-Turner spectrometer, following which it is led to a linear array of cooled (4.2 K) InSb detectors through a silver-plated brass waveguide system comprising a WR-71 ( $12.95 \times 36.48$  mm) rectangular waveguide section followed by a rectangular-to-circular waveguide transition from WR-51 to a 12.7-mm-diam circular guide. The measured insertion losses of the L-shape waveguide and the waveguide transition are 3.8 and 0.1 dB, respectively, at 170 GHz.

The InSb detectors are mounted in an optical integrating cavity behind the f3.5 Winston cone<sup>72</sup> optics, which is simply an off-axis parabola of revolution designed to maximize the collection of the incoming rays that first pass through  $55 \text{ cm}^{-1}$  low pass filters located at the input of the cones. The detector outputs are amplified using direct-current (dc)-coupled preamplifiers ( $10^3$  to  $10^4$  voltage gain) where the offset voltage is canceled by using two signals: the first taken 1 min prior to the discharge and the second at the end of the discharge.

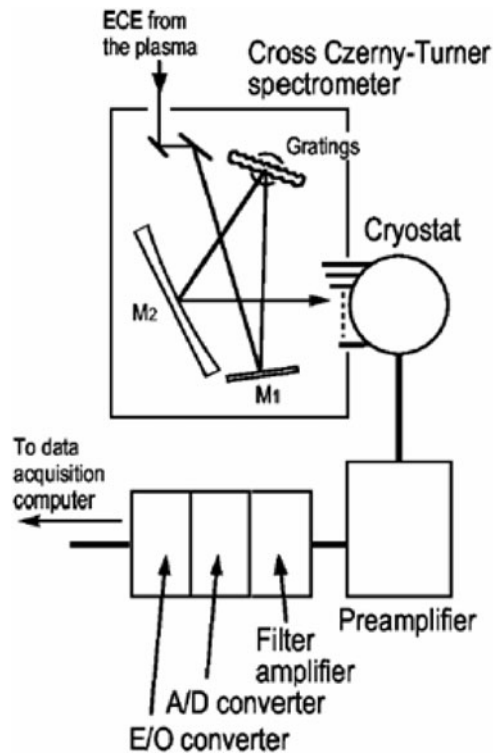


Fig. 5. Schematic of the JT-60 grating polychromator system. (From Ref. 65)

Although the time response of the InSb detector was as fast as  $1 \mu\text{s}$ , the data are only sampled over  $20\text{-}\mu\text{s}$  windows for 15 s because of JT-60 data acquisition system limitations. The measured optical responsivity and NEP are 2.5 to 5.4 kV/W and 0.5 to 1.1 pW/ $\sqrt{\text{Hz}}$  at 1 kHz, respectively. The actual number of measurement channels is 17 because 3 of the 20 channels are employed as reference channels for background noise measurement. The system has been employed both for electron temperature measurements as well as for the study of temperature perturbations near the internal transport barrier (ITB) in reversed shear discharges.

The 512-channel FTS instrument is described in Ref. 73 and covers the spectral region from 100 to 800 GHz with a temporal resolution of  $\sim 25$  ms. This instrument is absolutely calibrated using a liquid nitrogen load and is primarily utilized to determine whether ECE is emitted from thermal electrons and to provide an absolutely calibrated measurement of electron temperature profiles. The GPS and HRS instruments are cross-calibrated against the FTS instrument. In the case of ELMy H-mode plasmas, they employ maximum entropy techniques to obtain estimates of the ECE spectra from incomplete interferograms.<sup>74</sup>

Currently, there are two heterodyne radiometers installed on JT-60. One instrument<sup>75</sup> covers the range from 176 to 188 GHz, while a second instrument spans the

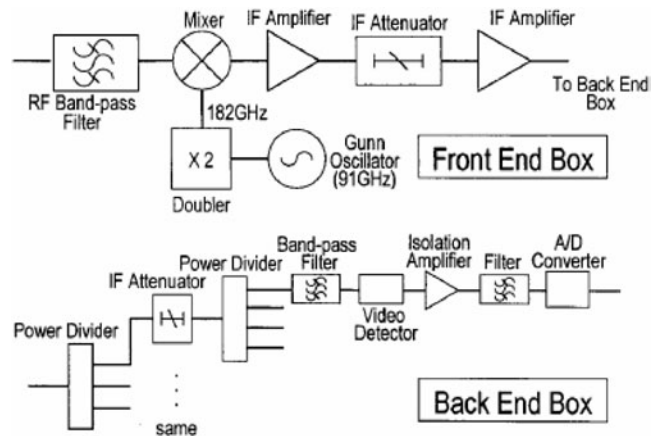


Fig. 6. Schematic diagram of the JT-60 182-GHz heterodyne radiometer. (From Ref. 66)

range 189 to 200 GHz (Ref. 66). Figure 6 illustrates schematically the heterodyne radiometer. The ECE radiation passes through a high pass filter to block the lower sideband (164 to 176 GHz) where it is mixed with the 182-GHz local oscillator (LO) signal produced by a Gunn diode/doubler combination and downconverted to 6 to 18 GHz for subsequent IF amplification. The amplified IF signal is divided into 12 channels, each of which contains a bandpass filter and a video detector. The bandpass filters have a width of  $\pm 250$  MHz about their center frequencies (corresponding to a spatial resolution of  $\sim 0.5$  cm) with their center frequencies spaced from 6.5 to 17.5 GHz at 1-GHz intervals. The receiver noise temperature is  $\sim 4300$  K, and the output linearity is within 5% for signal inputs ranging from  $-50$  to  $-20$  dBm. Following video detection, the signals are sent to an isolation amplifier followed by an analog-to-digital converter (ADC), with the digitized signals transmitted to the data acquisition computer via optical fibers. Two data acquisition systems are employed: a slower sampling system ( $20 \mu\text{s}$ ), which permits recording of the entire 15-s discharge, and a faster sampling system ( $1 \mu\text{s}$ ), where a several-hundred-millisecond-duration window of interest can be sampled at increased rate.

### II.E.2. LHD ECE Systems

Another example of an integrated ECE diagnostic system is represented by the implementation on the Large Helical Device (LHD) in Japan<sup>25,76-78</sup>; LHD is the world's largest heliotron-type device, with a complicated magnetic field configuration produced by  $1 = 2/m = 10$  continuous helical coils and three pairs of poloidal coils. Table III briefly lists the ECE instruments and their relevant characteristics.

Second-harmonic X-mode radiation is measured with both an FTS comprising a fast scanning Michelson



TABLE III  
 Characteristics of the ECE Diagnostics Operating on the LHD\*

	FTS	GPS	72-GHz Radiometer	132-GHz Radiometer	ECEI
Time resolution	25 ms	1 $\mu$ s	1 $\mu$ s	1 $\mu$ s	1 $\mu$ s
Frequency coverage (GHz)	50 to 500	105 to 148	53 to 87	106 to 158	132 to 148
Frequency resolution (GHz)	4.0	2.6 at 150 GHz	1 GHz	1 to 2 GHz	0.3
Number of channels	1	14	32	32	4 (8)
Detector	InSb	InSb	Schottky diode	Schottky diode	Schottky diode

\*Reference 77.

interferometer and with a GPS. The LHD 14-channel Czerny-Turner diffraction GPS is described in Ref. 76. As indicated in Table III, there are two heterodyne radiometers on LHD to monitor emission from both the LFS and HFS (Refs. 25 and 77).

### II.E.3. TEXTOR ECE Systems

A final example of modern ECE implementations is the TEXTOR ECE systems<sup>79</sup> whose characteristics are summarized in Table IV. The array of ECE instruments is intended to provide electron temperature profile measurements with moderate spatial resolution ( $\sim$ 1- to 4-cm vertical spot size and as low as  $\sim$ 1 cm radially for the 11-channel system) and relatively good temporal resolution (up to several hundred kilohertz) for physics studies involving spatially localized structures such as transport barriers, filaments, and magnetohydrodynamic (MHD) islands. As noted earlier, the ECE imaging (ECEI) technique is the subject of Sec. IX.B, where the use of 1-D imaging detector arrays to provide 2-D images of temperature fluctuations is discussed in detail together with the ECEI instrument on TEXTOR (Refs. 20 and 21).

The 11-channel radiometer monitors X-mode emission over the range between 105 and 145 GHz for temperature profile determination and has an IF bandwidth

of 200 MHz. Absolute calibration is achieved through the use of a hot-cold blackbody load that is located within the tokamak vessel during machine venting. The three six-channel spectrometer systems are employed for high spatial resolution, localized measurements of MHD behavior by arranging their viewing frequencies to coincide with the radial positions of the rational q-surfaces. Information concerning fast electrons is obtained from measurements using the combined second-harmonic (110.7-, 113.3-, 116.7-, and 120-GHz) and third-harmonic (166-, 170-, 175-, and 180-GHz) heterodyne radiometer, which permits simultaneous measurement of second- and third-harmonic radiation from four radial positions in the plasma.

As noted in the preceding, simultaneous measurement of the optically thick second-harmonic and optically thin third-harmonic spectra yields information about the velocity distribution of nonthermal electrons. In this instrument, ECE radiation from the LFS is collected by a parabolic antenna located in the equatorial plane where spurious reflections from the opposite wall are minimized through the use of a graphite beam dump. Studies of nonthermal electrons in TEXTOR using this approach are described in Refs. 28, 79, and 80. In addition to the use of third-harmonic emission measurements in the study of nonthermal electrons, third-harmonic ECE measurements were employed to obtain electron temperatures

TABLE IV  
 TEXTOR ECE Systems

	$T_e$ -Profile Radiometer	Spectrometers	Second-/Third-Harmonic Radiometer	16-Channel Tunable Radiometer	ECE Imaging
Number of Channels	11	3 $\times$ 6	4/4	16	16
Frequency range (GHz)	105, 107, 109, 112, 115(5), 145	104 to 114 125 to 130 133 to 148	111 to 120 116 to 118	98 to 146	113 to 145
IF bandwidth (MHz)	200	200 400	200	400 to 3000	550
Sampling rate (kHz)	25	25 to 1000	25	100 to 2000	100 to 2000

under plasma conditions with electron densities exceeding the cutoff for the standard second-harmonic ECE measurement.<sup>81</sup>

The final TEXTOR ECE instrument is a 16-channel frequency-tunable heterodyne system (covering 98 to 146 GHz, divided over the 16 channels with a bandwidth of 3 GHz each), which is derived from the 20-channel radiometer originally employed on the Rijnhuizen tokamak project (RTP) tokamak<sup>82</sup> and which is installed at the same toroidal position as the three high-resolution, six-channel spectrometers.

#### II.E.4. RTP ECA Diagnostic

As an example of the application of the ECA technique, we consider the 20-channel ECA diagnostic, which was demonstrated at RTP (Ref. 50) as an electron pressure profile diagnostic. The instrument simultaneously measured emission and absorption at the second harmonic where the microwaves were injected from the HFS and detected at the LFS in the equatorial midplane. In this study, a 20-channel heterodyne radiometer (86 to 146 GHz) was connected to a receiver antenna on the outboard, LFS. On the HFS, two backward wave oscillators (BWOs) (78 to 118 GHz, 100-mW output; 118 to 150 GHz, 35-mW output) were connected to the HFS transmission line and operated in sweep mode with a sweep time  $>0.5$  ms, covering the bandwidth of the LFS radiometer. Spurious reflections and standing waves were minimized by the use of Macor<sup>®</sup> machinable glass ceramic viewing dumps. Considerable care was devoted to eliminating the complications caused by nonresonant losses such as refraction. A comparison between the ECA derived electron pressure profiles with those obtained from Thomson scattering resulted in good agreement. Here, the authors stressed the need for carefully accounting for the effective attenuation of the probe beam by

processes other than resonant absorption, principally refraction (the major effect) and scattering from density fluctuations. After accounting for these effects, by applying ECA, the pressure profile could be measured with a temporal resolution of 1 ms, while in this case, the Thomson scattering measured only a single profile during the entire discharge.

#### II.F. Applicability to a BPX

ECE measurements are expected to continue to play an important role in next-generation devices such as ITER (Refs. 83, 84, and 85) with instruments providing both core and edge plasma data. In addition to equilibrium temperature and fluctuation data, it is envisioned that estimates of ECE power loss may be made via full-spectrum ECE measurements

Since the electron density and toroidal field values for ITER are comparable to those in existing devices, there exist no major technological development hurdles to be overcome as far as the instruments themselves are concerned. The major challenges derive from the long transmission paths, need for development of a radiation hard calibration source, limited access, hostile environment, and relativistic effects leading to harmonic overlap and accessibility issues. Despite these challenges, designs have been made for the complete ECE system comprising the antenna array mounted on the equatorial port plug, transmission system, and spectrometers. ECE radiation is transmitted out of the vacuum vessel, cryostat, and shield and subsequently enters the spectrometers, which are located in the diagnostic hall. Figure 7 illustrates one of the proposed arrangements for the ITER ECE system. Two Gaussian collection antennas, which are staggered above and below the midplane, provide access to the core for a variety of plasma shapes. The miter bends provide compensation for machine movement.

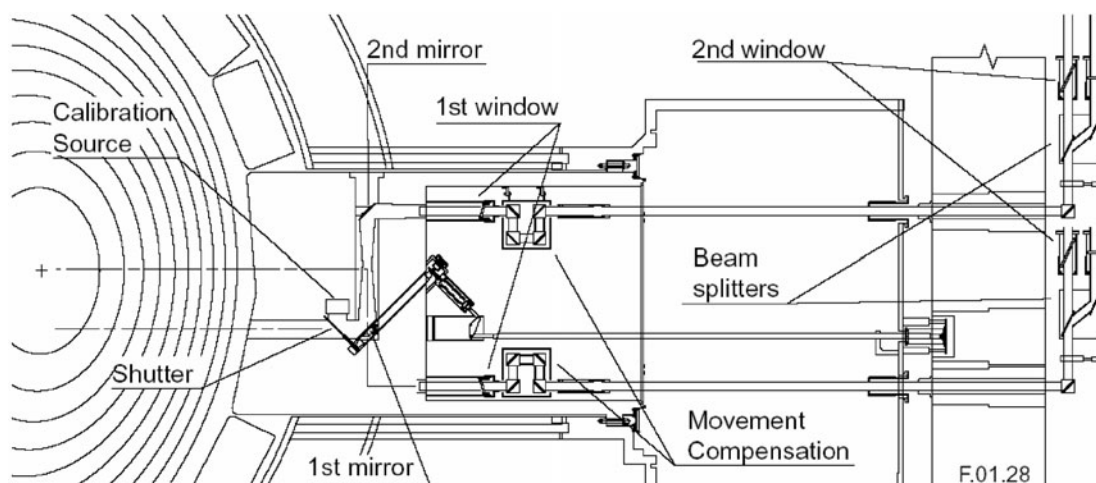


Fig. 7. Layout of envisioned ITER ECE system. (From Ref. 347)

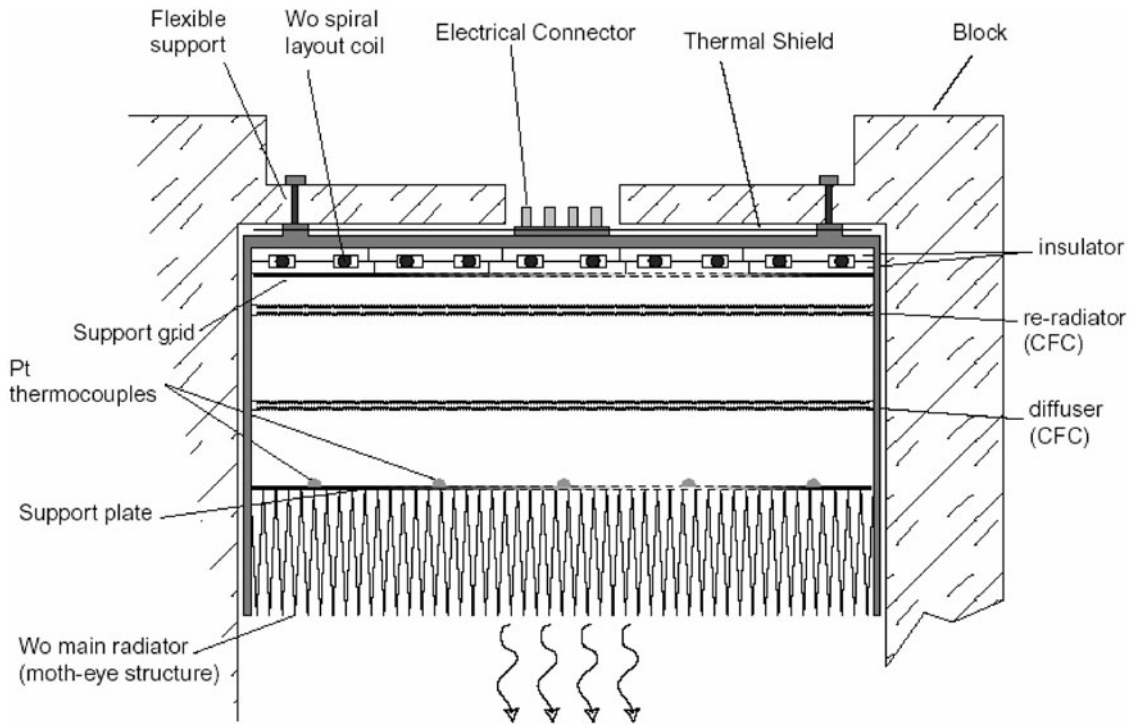


Fig. 8. Sketch of a possible ITER in situ ECE calibration 700°C hot source cross section. The overall diameter of the source is 200 mm. Internal supports not shown. (From Ref. 347)

As noted in the preceding, absolute spectral calibration of the ECE system is essential for independent  $T_e$  measurements. Here, the ITER machine environment requires that a dedicated calibration source be built into the optics in the port plug to ensure that the accuracy of the ECE measurements can be ensured over the operating life of the device (see Fig. 7) (Refs. 86 and 87). The shutter permits the hot source to be brought into view for in situ calibration. Figure 8 illustrates a possible ITER in situ ECE calibration 700°C hot source cross section.<sup>86</sup> Over the range 122 to 366 GHz, the emissivity is required to exceed 0.7, while over 70 GHz to 1 THz, it must exceed 0.5. In order to achieve these values together with the requisite reliability, a careful choice of materials is necessary as well as proper electromagnetic considerations such as the use of the moth-eye arrangement.<sup>88</sup>

In addition to the ECE system, under investigation is the possible development of an ECA system for use in the divertor region.

Table V lists the desired specifications in the measurement of electron temperature for the edge and core regions. The specifications were determined from a consideration of the intended use of the measurements in plasma control and physics studies. For example, steep transport barriers are observed inside the plasma core, and electron temperature pedestals at the edge play a role in analysis of the transport; it is essential to have sufficient spatial resolution to accurately measure them.

TABLE V  
ITER ECE Electron Temperature Measurement Requirements

	Spatial Region	Range (keV)	$\Delta t$ (ms)	$\Delta x$	Accuracy (%)
Core	$r/a < 0.9$	0.5 to 40	10	$a/30$	10
Edge	$r/a > 0.9$	0.05 to 10	10	5 mm	10

The 10-ms time resolution is short compared to times of interest while allowing for study of MHD behavior as well as being sufficiently fast for control purposes (for example, kinetic control of the stored energy or ITB gradient) since this is much faster than the typical core confinement times and of the same order as the heating response time.<sup>89</sup> However, it is noted that the upper required frequency response for the study of low ( $m, n$ ) MHD modes, sawteeth, and disruption precursors is 3 kHz, thus requiring a faster time response.<sup>90</sup> Furthermore, the study of high-frequency instabilities requires even higher-frequency response (up to  $\sim 300$  kHz). These include microturbulence, nonlinear tearing modes, and Alfvén eigenmodes.

Design studies have revealed that the edge plasma spatial resolution goal is extremely challenging and that

the actual resolution possible by ECE measurements may be  $\cong 5$  cm, far from the 5-mm goal.<sup>91</sup> In addition, it is felt that it may prove difficult to measure edge temperature values  $< 1$  to 2 keV, again far from the measurement goal. In consequence, an alternative system based on Thomson scattering is under design for this region (also, see Chapter 4, “Laser-Aided Plasma Diagnostics,” by A. J. H. Donné, C. J. Barth, and H. Weisen, in this special issue of *Fusion Science and Technology*).

### III. ELECTRON BERNSTEIN WAVE EMISSION

#### III.A. Introduction/Review

When  $\omega_{pe} > 1.6\omega_{ce}$  in a magnetically confined plasma, conventional ECE electron temperature radiometric measurements cannot be employed. This regime is often referred to as the overdense regime. This class of plasmas includes reversed field pinches, spherical tori and higher aspect ratio tokamaks, and stellarators that operate at high  $\beta$ . Electrostatic electron Bernstein waves<sup>92</sup> (EBWs) can propagate across the magnetic field and are strongly absorbed and emitted at ECRs in overdense plasmas. The optical depth  $\tau_s$  for EBW emission (EBE) is typically a few hundred to several thousand, well in excess of the optically thick blackbody condition  $\tau_s > 2$ . These characteristics make thermal EBE potentially attractive as a local electron temperature diagnostic in overdense plasmas where conventional ECE radiometry is not possible. However, EBE cannot propagate outside the upper hybrid resonance (UHR) that surrounds an overdense plasma. Consequently, EBE radiometric measurements of local electron temperature using an external antenna employ a mode conversion process in the vicinity of the UHR to couple EBE to electromagnetic waves outside the overdense plasma. EBE can convert to electromagnetic radi-

ation outside the plasma by either coupling to the extraordinary mode (B-X conversion)<sup>93</sup> or to the ordinary mode (B-X-O conversion).<sup>94</sup>

EBE radiometry via B-X conversion is enabled by viewing the plasma normal to the magnetic field and depends on the conversion of EBE to X-mode electromagnetic radiation via the slow X-mode (SX) (Fig. 9a). The left hand cutoff of the SX, the UHR, and the right hand cutoff of the fast X-mode (FX) form a cutoff-resonance-cutoff triplet allowing the SX to tunnel through the UHR to the X-mode electromagnetic wave. The maximum B-X conversion efficiency for  $N_{\parallel} = 0$  (where  $N_{\parallel} = ck_{\parallel}/\omega$ ;  $k_{\parallel}$  is  $2\pi$  divided by the radiation wavelength parallel to the magnetic field direction, and  $\omega$  is the wave frequency) is given by<sup>93</sup>

$$C_{\max} = 4e^{-\pi\eta}(1 - e^{-\pi\eta}) , \quad (13)$$

where  $\eta$  is the tunneling parameter. For magnetic scale lengths much greater than the density scale length at the UHR,

$$\eta \approx [\omega_{ce}L_n/ca](\sqrt{1+a^2}-1)^{1/2} , \quad (14)$$

where

$$a = [\omega_{pe}/\omega_{ce}]_{\text{UHR}}$$

$$L_n = \left| \frac{n_e}{dn_e/dR} \right|_{\text{UHR}}$$

$\omega_{ce}, \omega_{pe}$  = electron cyclotron and plasma frequencies, respectively

$n_e$  = electron density

$c$  = velocity of light.

EBE radiometry via B-X-O conversion (Fig. 9b) requires the coincidence of the X-mode and O-mode cutoffs, which is accomplished with an oblique view of the

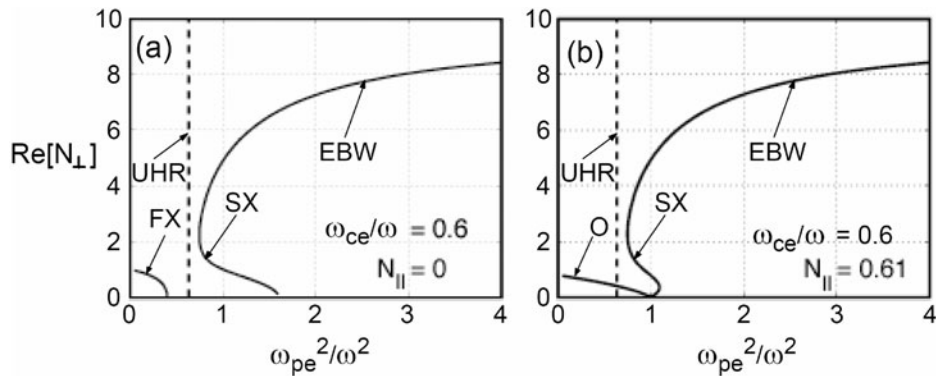


Fig. 9. EBW and electron cyclotron wave roots of the real part of  $N_{\perp}$  as a function of  $\omega_{pe}^2/\omega^2$  for (a) perpendicular (B-X;  $N_{\parallel} = 0$ ) launch and (b) oblique (B-X-O;  $N_{\parallel} = N_{\parallel, \text{opt}} = 0.61$ ) launch. (Adapted from J. Decker, “Electron Bernstein Wave Current Drive Modeling in Toroidal Plasma Confinement,” PhD Thesis, Massachusetts Institute of Technology, p. 33, Fig. 1–4, 2005)

plasma at a specific angle to the magnetic field at the mode conversion layer. The B-X-O emission leaves the plasma through an angular transmission *window* with a width that depends on  $L_n$  at the X-mode and O-mode cutoffs, given by [E. MJØLHUS, “Coupling to Z Mode Near Critical Angle,” *J. Plasma Phys.*, **31**, 7 (1984)] [F. R. HANSEN, J. P. LYNOC, C. MAROLI, and V. PETRILLO, “Full Wave Calculations of the O-X Mode Conversion Process,” *J. Plasma Phys.*, **39**, 319 (1988)]

$$T(N_{\perp}, N_{\parallel}) = \exp\{-\pi(\omega L_n/c)\sqrt{Y/2}\} \\ \times [2(1+Y)(N_{\parallel, opt} - N_{\parallel})^2 + N_{\perp}^2] \}, \quad (15)$$

where

$$Y = (\omega_{ce}/\omega) \\ N_{\parallel, opt}^2 = [Y/(Y+1)] \\ N_{\perp} = ck_{\perp}/\omega.$$

Once the conditions for efficient coupling of thermal EBE to electromagnetic radiation have been resiliently established in the vicinity of the UHR, the technology used for EBE radiometry is identical to that used for conventional ECE radiometry. EBE radiometry has the potential to measure the evolution of the electron temperature profile with excellent temporal and spatial resolution at relatively little expense, compared to, say, a Thomson scattering diagnostic. The high optical depths typical of EBWs can allow inexpensive localized electron temperature measurements in even relatively cool, dense process plasmas. However, in order to deduce the plasma radial electron temperature from the EBE radiation spectrum, EBW ray tracing must be used to determine the location of the source of the emission. The deduced emission location depends sensitively on the  $N_{\parallel}$  of the EBWs, and the variation of  $N_{\parallel}$  as the EBWs propagate from the emission source to the EBW radiometer antenna depends on the local magnetic field and the electron density. Consequently, detailed magnetic equilibria and electron density profile measurements are required in order to deduce the electron temperature profile from the measured EBE spectrum. The radial resolution of an EBE electron temperature diagnostic can be significantly degraded as a result of the Doppler broadening resulting from intrinsic EBW  $N_{\parallel}$  broadening in the plasma. Also, because the measured EBW radiation temperature includes the EBW mode conversion efficiency, the EBW mode conversion process must be modeled. This modeling requires a good measurement of the electron density gradient scale length in the vicinity of the EBW mode conversion; this is particularly the case for EBE measurements that use B-X conversion.

One issue that can limit the temporal resolution of EBW radiometry is the presence of electron density fluctuations

in the EBW mode conversion region. The edge region of magnetically confined plasmas can exhibit rapid fluctuations in electron density. If the EBW mode conversion layer happens to lie near the edge of the plasma, as is often the case for fundamental and second-harmonic EBE conversion in plasmas where  $\omega_{pe} \gg \omega_{ce}$ , then these density fluctuations will modulate the measured EBE radiation temperature, effectively limiting the temporal resolution.

### III.B. Modern Implementations

The electron temperature profile evolution was first measured successfully with EBE radiometry via B-X-O conversion on the Wendelstein-7AS stellarator<sup>95,96</sup> (W7-AS). The elliptical O-mode polarization detected along an oblique angle to the magnetic field was changed to linear polarization by an elliptical waveguide that provided a quarter-wave phase shift (Fig. 10a). A 66- to 78-GHz heterodyne microwave receiver measured the time evolution of the emitted power spectrum. The electron temperature profile was derived from the emitted EBW spectrum (Fig. 10b) by mapping to the radial location of the EBE source with a three-dimensional (3-D) EBW ray-tracing code. Good agreement between the electron temperature profile measured by EBE radiometry and Thomson scattering was obtained (Fig. 10c). The W7-AS EBW radiometer diagnostic was successfully applied to measurements of edge-localized modes (ELMs) and to heat wave propagation to determine local heat transport coefficients during modulated second-harmonic EBW heating.

EBE radiometry via B-X-O and B-X conversion has also been studied on the Mega Amp Spherical Torus<sup>97,98</sup> (MAST) between 16 and 60 GHz. The main features of the B-X-O emission from a MAST plasma discharge are summarized in Fig. 11. EBE from the first three electron cyclotron harmonics is clearly seen during the initial stage of the discharge (darker areas correspond to higher-intensity EBE). The gaps in the spectrum between harmonics are always present and correspond to the plasma layers where the cyclotron harmonics coincide with the UHR. The plasma enters H-mode at 88 ms, and the EBW mode conversion layer shifts from the bulk plasma outward toward the last closed flux surface (LCFS). The increase in the edge density gradient as the plasma enters the H-mode results in an increase in EBE intensity at all harmonics.

Recently, ~80% fundamental-harmonic B-X-O conversion was measured on the National Spherical Torus Experiment (NSTX) with a quad-ridged horn antenna and dual-polarization radiometry.<sup>99</sup> The time evolution of the EBE radiation temperature agreed well with predictions using 3-D ray tracing and a 1-D full-wave mode conversion model.<sup>100</sup>

EBW emission via B-X conversion has been studied on the COMPASS-D tokamak between 53 and

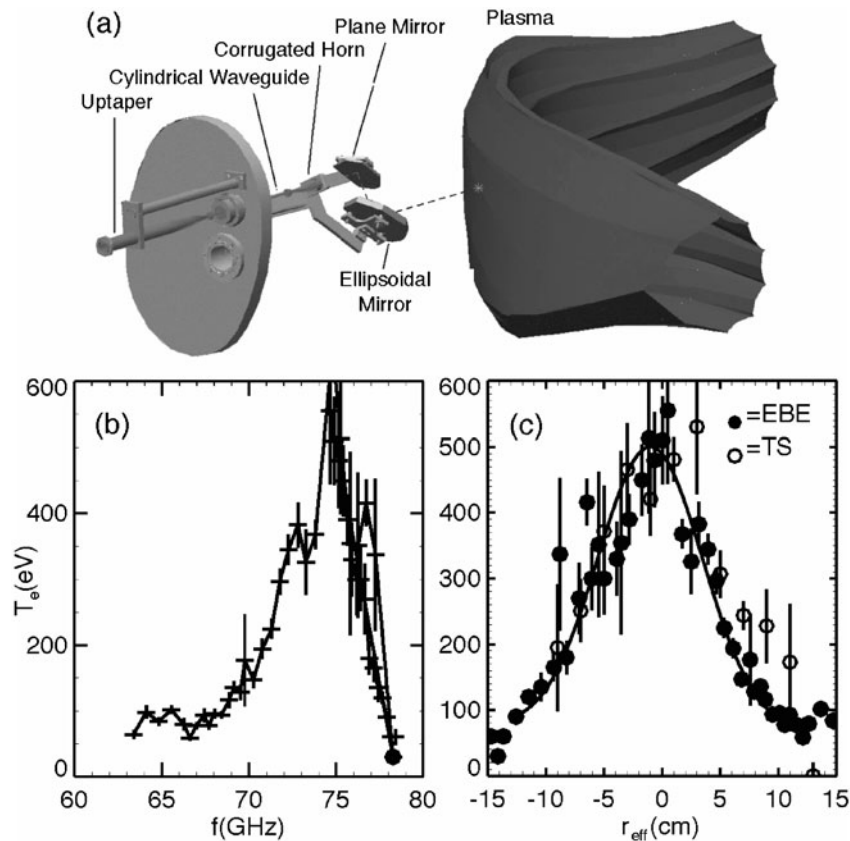


Fig. 10. (a) Gaussian-optical EBE antenna installed in W7-AS, consisting of an ellipsoidal mirror and a corrugated horn. (b) Spectrum of EBW emission at first harmonic. (c) Electron temperature profile reconstructed with the aid of an EBW ray-tracing code (solid circles). Thomson scattering data are also shown for comparison (open circles). (From Ref. 96)

66.5 GHz with a 14-channel heterodyne radiometer.<sup>101</sup> EBE increased by an order of magnitude at the transition to H-mode, and the EBW conversion efficiency increased from a few percent to 15% as a result of the H-mode-induced density gradient steepening at the B-X mode conversion layer. Similar increases in B-X conversion efficiency have been reported to occur at the transition to H-mode on NSTX [G. TAYLOR et al., “Enhancement of Mode-Converted Electron Bernstein Wave Emission During National Spherical Torus Experiment H-Mode Plasmas,” *Phys. Plasmas*, **9**, 167 (2002)]. Measurements of B-X EBE on the Madison Symmetric Torus (MST) reversed field pinch yielded intrinsic B-X conversion efficiencies up to  $\sim 75\%$  (Fig. 12). EBE from MST was confirmed to be predominantly X-mode polarized, as expected.<sup>102</sup>

As can readily be seen from Eqs. (13) and (14), the tunneling associated with B-X conversion is sensitively dependent on the density scale length at the B-X conversion layer. Since fundamental- and low-harmonic EBE often mode converts outside the LCFS, it is possible to resiliently achieve B-X conversion efficiency approaching 100% by steepening the density gradient at the B-X

mode conversion layer with a local limiter. A local limiter surrounding a quad-ridged antenna (Fig. 13) was successfully used on the Current Drive Experiment–Upgrade (CDX-U) to produce  $\sim 100\%$  B-X conversion.<sup>103</sup> The CDX-U 4- to 12-GHz, B-X radiometer measured the electron temperature profile evolution, the electron thermal diffusivity,<sup>104</sup> and the magnetic field profile.<sup>105</sup> A local limiter was also employed on NSTX to enhance the fundamental-harmonic B-X conversion efficiency to  $\sim 40\%$  (Ref. 106). On both CDX-U and NSTX, the measured dependence of B-X mode conversion efficiency on  $L_n$  was in good agreement with B-X mode conversion theory (Fig. 14) (Ref. 93).

On the TST-2 spherical torus, a B-X EBE diagnostic combining a heterodyne radiometer and a reflectometer measured emission between 5 and 12 GHz and the density profile in front of the radiometer antenna (Fig. 15a) (Ref. 107). B-X mode conversion efficiencies of 50 to 80% were estimated with the help of a 1-D full-wave calculation. An electron temperature profile was reconstructed from the fundamental- and second-harmonic EBE. A clear correlation between the measured reflectivity and the calculated B-X conversion efficiency was observed (Fig. 15b).

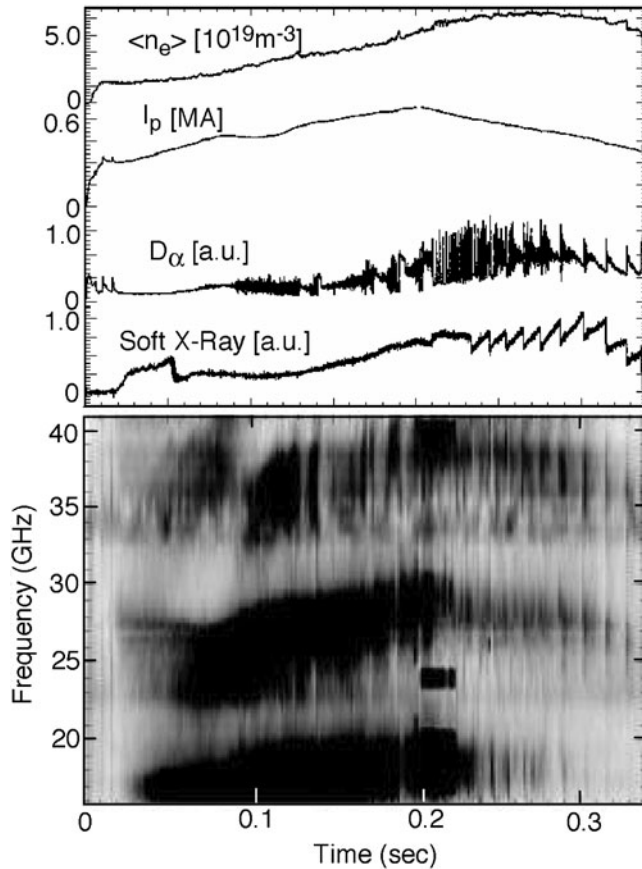


Fig. 11. EBW emission spectrum from MAST measured in a plasma with plasma current rampdown. Darker areas correspond to higher EBW emission intensity. (Reproduced from Ref. 97)

### III.C. Applicability to a BPX

EBE diagnostics have limited applicability for future burning plasma experiments (BPXs). Large-aspect-ratio burning plasmas, such as ITER and ARIES-AT, are not suitable candidates for an EBE diagnostic since they are not projected to operate in the overdense regime ( $\omega_{pe}/\omega_{ce} \sim 0.6$  for ITER and  $\sim 0.8$  for ARIES-AT). While small-aspect-ratio, high  $\beta$  burning plasma devices such as ARIES-ST would operate within the overdense regime (for ARIES-ST  $\omega_{pe}/\omega_{ce} \sim 2.5$ ), the combination of the small aspect ratio and high  $\beta$  of these devices (ARIES-ST aspect ratio  $\sim 1.6$ ,  $\beta_t \sim 50\%$ ) will significantly constrain the radial access of an EBE diagnostic. Even at fundamental EBE frequencies, where harmonic overlap may be minimal, the presence of a deep magnetic field well at high  $\beta$  will restrict radial access. In addition, the finite  $N_{||}$  spectrum typically collected by an EBE diagnostic antenna will lead to potentially significant Doppler broadening of the imaged cyclotron resonances that will further constrain radial access and radial resolution. One poten-

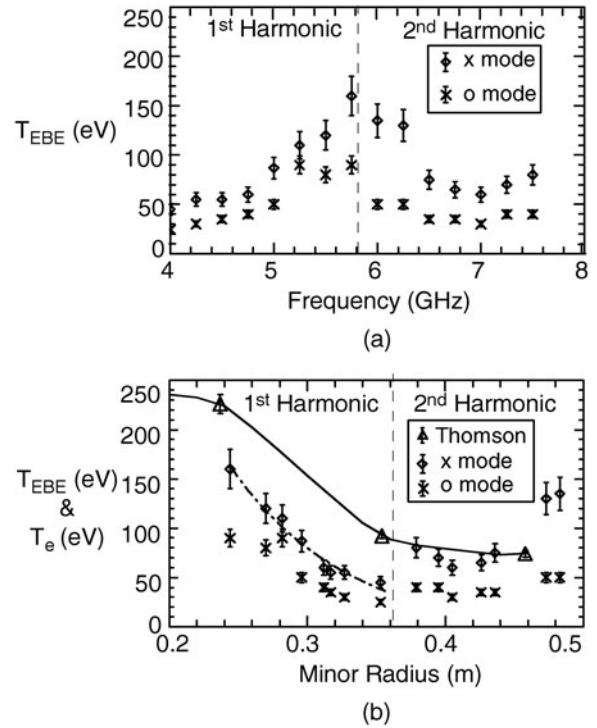


Fig. 12. (a) Measured O-mode and X-mode EBE radiation temperature versus emission frequency. (b) Spectrum for O-mode and X-mode EBE radiation temperature mapped to minor radius. Also shown are the electron temperature data from Thomson scattering. The vertical dashed line separates emission from two cyclotron harmonics. (Reproduced from Ref. 102)

tial application for EBE in a BPX is for diagnosing the electron temperature in the divertor region, where the plasma will be very dense and operating well into the overdense regime. The viability of EBE radiometry for this application will, however, depend on establishing resilient coupling between the EBWs and the EBE antenna as the magnetic field geometry and density profile changes in the divertor.

## IV. REFLECTOMETRY

### IV.A. Introduction

Reflectometry is a radar technique intended to measure the electron density profile and its fluctuations by means of the reflection of electromagnetic waves at the plasma cutoff layer, when the refraction index goes to zero for the particular wave frequency. The technique was originally employed for measurements of the ionospheric structure<sup>108,109</sup> and initiated a rapid development as a fusion plasma diagnostic by the mid-1980s (Refs. 110, 111, and 112). Today, it has become a well-documented and well-understood diagnostic for density profile

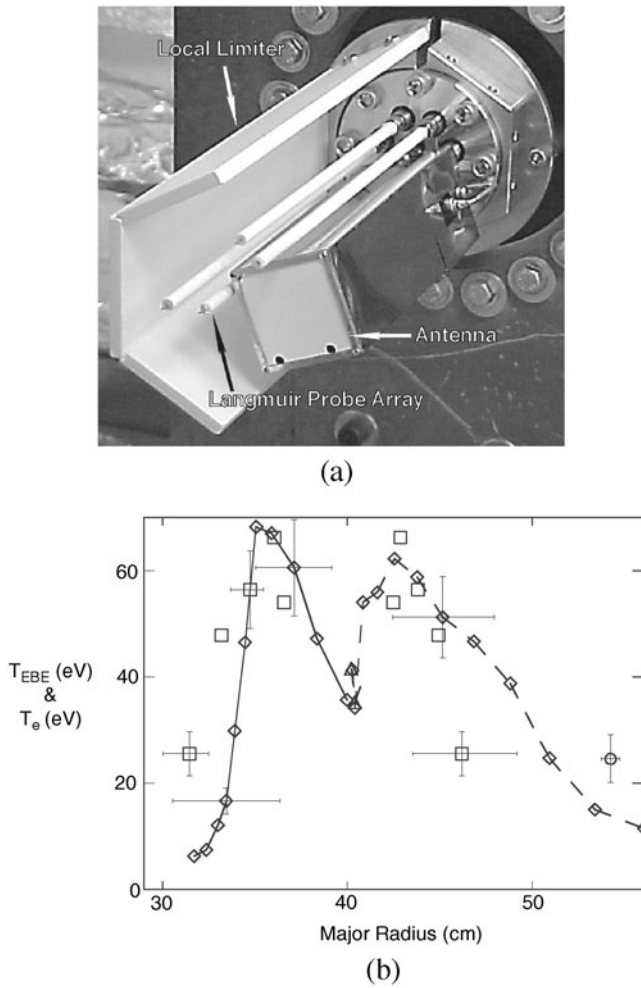


Fig. 13. (a) Photograph of the CDX-U EBW diagnostic antenna that combined a quad-ridged horn antenna to measure emission, a moveable local limiter (half shown) to modify  $L_n$  in front of the antenna to optimize B-X conversion, and a Langmuir probe array to measure  $L_n$ . (b) The EBE radiation temperature mapped to major radius at the midplane of CDX-U with the local limiter producing  $L_n$  for  $\sim 100\%$  EBW conversion. The fundamental EBE (diamonds, solid line) and second-harmonic EBE (diamonds, dashed line) are plotted together with the  $T_e$  data measured by Thomson scattering (square). (Adapted from Ref. 103)

measurements, whereas it is still developing its ability to measure localized density fluctuations.

The fundamentals of reflectometry have been explained in a number of publications, and we will concentrate here only on basic principles; a comprehensive description can be found in Ref. 10, and an overall review of the technique is available in Ref. 113. As noted earlier, if we assume a plasma in slab geometry with a wave propagating perpendicular to the external magnetic field  $B$ , we have two particular cases for which the re-

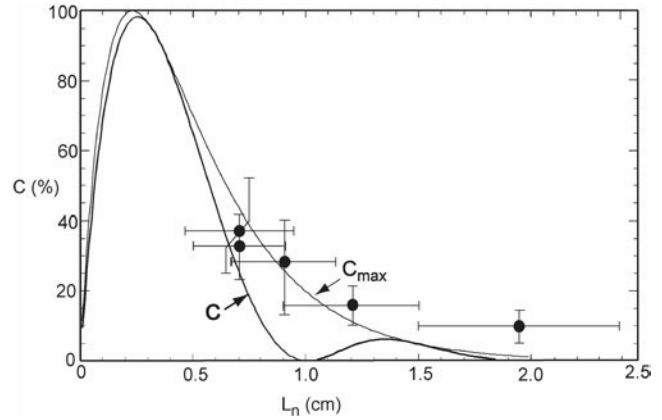


Fig. 14. The measured  $T_{EBE}/T_e$  from an NSTX B-X emission measurement versus the  $L_n$  measured by reflectometry at the B-X mode conversion layer, for 11.6-GHz EBE (filled circles). Error bars indicate the fluctuation amplitude of  $T_{EBE}$  and  $L_n$  within the analysis time window. Experimental results are compared to the theoretical maximum B-X mode conversion efficiency ( $C_{max}$ , thin line) and the theoretical B-X mode conversion efficiency ( $C$ , thick line). (Reproduced from Ref. 106)

fractive index has a simplified dependence on the plasma electron density and the external magnetic field: the “ordinary” wave (O-mode) with  $E \parallel B$  and the “extraordinary” wave (X-mode) with  $E \perp B$ . The cutoffs will be  $\omega_o = \omega_p$  (O-mode cutoff) and  $\omega_x = \omega_{ce}/2 \pm (\omega_{ce}^2 + 4\omega_{pe}^2)^{1/2}/2$  [right-hand X-mode cutoff for plus (+) and left-hand X-mode cutoff for minus (-)]. Typical values are  $\omega_p/2\pi = 30$  GHz for  $n_e = 10^{19} \text{ m}^{-3}$  and  $\omega_{ce}/2\pi = 28$  GHz for  $B = 1$  T; the relevant frequencies for reflectometry ranging from 10 to 150 GHz (below 10 GHz implementation becomes very difficult because of the large size of the required antennas and large beam diameters).

The above expressions are valid for moderate electron temperatures. For values of  $T_e$  above 1 keV, relativistic effects can appear, being more important for the X-mode.<sup>114</sup>

Another relevant element is that the waves would be (partially or totally) absorbed when they cross layers where the refractive index goes to infinity (“resonances”). The relevant resonances in reflectometry are the harmonics of the cyclotron frequency  $\omega_{ce}, 2\omega_{ce}, \dots$  and the “upper hybrid” frequency  $\omega_{UH} = (\omega_{ce}^2 + \omega_p^2)^{1/2}$ . Figure 16 shows some of the relevant frequencies for a typical scenario in JET.

One of the limitations of reflectometry is that we need a positive gradient of the cutoff frequency when we move away from the launcher; this limits the accessible range in many occasions to half the profile. However, in some particular cases, depending on the B-field



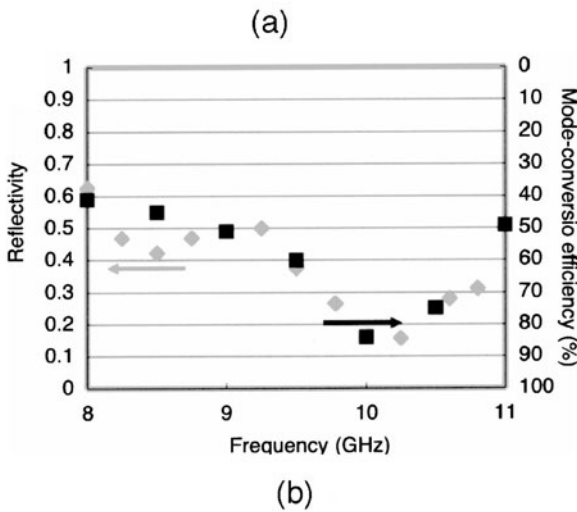
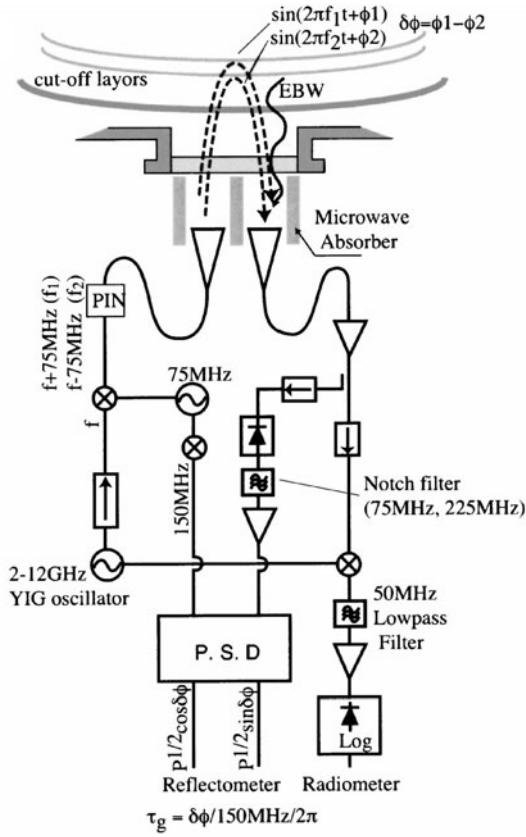


Fig. 15. (a) Block diagram of the radio reflectometer on TST-2. The frequency coverage is from 5 to 12 GHz, corresponding the fundamental-, the second-, and the third-harmonic emissions. (b) Comparison between the measured reflectivity and the calculated EBW mode conversion efficiency. (Reproduced from Ref. 107)

magnitude, density, and gradient of  $B$ , the X-mode can be used to reach the entire profile.

The parameters measured in reflectometry are the phase delay  $\phi$  of a wave reflected at the cutoff and its

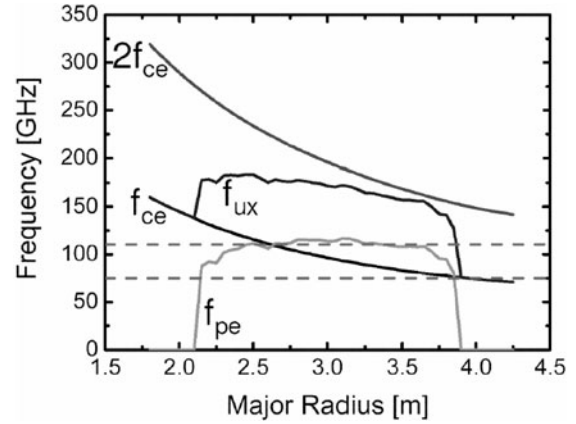


Fig. 16. Relevant frequencies for the JET tokamak. A typical density profile is taken, with  $B$  scaled to 3.5 T. The picture shows the O-mode ( $f_{pe}$ ), the right-hand X-mode ( $f_{ux}$ ) cutoffs, and the first and second harmonics of the cyclotron frequency ( $f_{ce}$ ,  $2f_{ce}$ ). A shadow region appears for X-mode access to the inner part of the plasma, due to strong absorption by the second  $f_{ce}$  harmonic. (Courtesy of P. Varela)

derivative  $\partial\phi/\partial\omega$ , which, in fact, is the time delay  $\tau$  of a narrowband pulse at frequency  $\omega$  traveling to the plasma and back. The phase delay  $\phi$  is related to the cutoff layer movements (density fluctuations) and  $\tau$  to the absolute cutoff position (density profile).

The solution to the problem of determining the phase delay of a wave that propagates through the inhomogeneous plasma and reflects at the plasma cutoff layer was proposed by Ginzburg.<sup>109</sup> It uses the WKB solution of the wave equation for the region where the refraction index is finite (and varies a small fraction when advancing one wavelength) and matches it to an exact solution in the vicinity of the critical layer, assuming a linear dependence of the dielectric permittivity  $\epsilon$  with distance for this region. This leads to

$$\phi(\omega) = \frac{2\omega}{c} \int_{r_c(\omega)}^{r_i} \eta(r) \cdot dr - \frac{\pi}{2}, \quad (16)$$

where

$r_i$  = radius at the plasma edge

$r_c(\omega)$  = position of the cutoff layer (also called “critical layer”) for the wave at frequency  $\omega$

$\eta$  = refractive index.

Equation (16) basically gives the delay along the two-way propagation path plus the negative shift  $\pi/2$ , which accounts for the reflection at the cutoff layer. This solution requires  $\epsilon$  to be linear in a region sufficiently wide for the Wentzel-Kramers-Brillouin (WKB) solution to be applicable. The width of this region  $\Delta r$  is referred to as

the so-called “thickness of the reflecting layer” in the literature<sup>109,110,115</sup> and is given by

$$\Delta r = 5 \left( \frac{c}{\omega} \right)^{2/3} \left[ \left( \frac{d\epsilon}{dr} \right)_{r_c} \right]^{-1/3} \quad (17)$$

for the general case and

$$\Delta r = 1.5 \times 10^5 \left[ \left( \frac{dn_e}{dr} \right)_{r_c} \right]^{-1/3} \quad (18)$$

for the O-mode (in SI units).

From Eq. (18), a typical gradient of  $10^{20} \text{ m}^{-4}$  would lead to  $\Delta r \approx 3 \text{ cm}$ . As we will discuss later, this value, which is set to provide 1% accuracy in the E-field amplitude, is relatively conservative if we want to take it as the theoretical radial resolution of the technique.

#### IV.B. Profile Measurements

Density profile determination is based on the measurement of the time delay of the reflected wave  $\tau$ . If we measure  $\tau(\omega)$  for a series of  $\omega$  values ranging from those reflecting at the plasma edge  $\omega_e$  to the ones reflecting at a given depth, the corresponding density profile can be derived by an inversion of Eq. (16). In the particular case of the O-mode, the solution<sup>110</sup> coincides with the formalism of an Abel inversion:

$$r(\omega_c) = \frac{c}{\pi} \int_{\omega_e}^{\omega_c} \tau(\omega) \cdot \frac{d\omega}{\sqrt{\omega_c^2 - \omega^2}}. \quad (19)$$

This expression provides the position for each value of the critical frequency. For the extraordinary mode, a wide variety of numerical inversion methods have been developed, many of them evolving from the original one proposed in Ref. 111.

One of the requirements for the profile inversion is that, in principle, we need to start the reconstruction from  $n_e = 0$ ; this is difficult for the X-mode (requires very high accuracy in the edge value of  $B$ , tunneling to the UHR for very low densities) and is impossible for the O-mode where the lowest feasible frequency is limited by technical issues as well as by the applicability of the WKB solution. This “initialization problem” has been studied in depth for the O-mode,<sup>116</sup> showing that as a general rule, the profile can be obtained, with an error of initialization that becomes negligible (compared to other sources) for  $n_e$  in excess of ten times that of the initial measuring point.

The analysis method described above has been the basis of density profile reflectometry for the last two decades, and contrary to the case of fluctuation reflectometry, it has been shown to work surprisingly well despite its simplicity and the assumptions involved. On the experimental side, a large number of reflectometers installed in fusion devices show routinely good quanti-

tative agreement with other diagnostics (Thomson scattering, multichannel interferometry, atomic beams). On the theoretical side, two of the assumptions have been tested: the 1-D model implicit in Eq. (19) and the use of the WKB solution. Simulations of profile reflectometry with 2-D turbulent density structures<sup>117</sup> have shown that by proper averaging of the reflected E-field at the receiving antenna, the perturbation due to 2-D effects can be minimized (at the cost of a loss of radial resolution, which for most scenarios is negligible). Concerning the use of the WKB solution, simulations have been performed<sup>118</sup> in order to compare the profile inversion based on a full-wave 2-D formalism (without turbulence) and the one based on the 1-D WKB assumption. The results show errors in the position for a given density layer on the order of a small fraction of the lowest probing wavelength. This work indicates that using  $\Delta r$  defined in Eq. (17) as the spatial resolution of profile reflectometry was too conservative.

##### IV.B.1. Profile Techniques and Implementation

The experimental approach to profile reflectometry employs different practical implementations to determine the  $\tau(\omega)$ . They can be grouped into four main families: frequency modulation (FM), amplitude modulation (AM), short pulse radar (PR), and ultrashort pulse systems, all of them using both the O-mode and right-hand X-modes. Other design choices are the use of homodyne or heterodyne receivers or a single antenna versus two antennas (separate launcher/receiver). Single-antenna systems are easier to calibrate and require less space for access; however, they are more sensitive to parasitic reflections from the antenna, windows, waveguide, etc. A comprehensive comparative study is given in Ref. 115.

Frequency modulation systems use fast temporal sweeping of a single frequency (50 GHz in 10  $\mu\text{s}$ ) in order to determine  $\phi(\omega)$ , from which  $\tau(\omega)$  is obtained. A fast sweep is required in order to overcome the temporal phase oscillations due to plasma turbulence, as well as Doppler shift effects caused by the fast rotation of density structures. Phase detection can be accomplished by means of both heterodyne or homodyne systems (the latter using as a carrier the fast phase increase originated during the sweep by the path difference between probing and reference beams), and parasitic reflections can be discriminated by spectral filtering. FM systems are operating at ASDEX Upgrade (Ref. 119), D-IIID (Refs. 120 and 121), Tore Supra (Ref. 122), and MAST (Ref. 123). Recently, a new FM system, operating with a broadband low-loss corrugated waveguide system, was installed at JET (Ref. 124).

Amplitude modulation systems launch an amplitude modulated signal (spectrally, one carrier plus two sidebands in phase) that allows one to measure directly  $\tau(\omega)$  (an important fact that simplifies the signal processing). A moderate speed sweep (50 GHz in 0.1 to 2 ms) of the

system central frequency provides the profile coverage. This technique is more resilient to turbulence effects and uses relatively simpler hardware. It requires two antennas because of the intrinsic difficulty to discriminate parasitic reflections. AM systems are used currently in Alcator C-MOD (Ref. 125) and TJ-II (Refs. 126 and 127). An essentially similar approach, used at TFTR (Refs. 128 and 129), is to launch simultaneously a couple of frequencies (with a separation on the order of 1 GHz) to measure  $\tau(\omega)$ .

Pulse radar systems utilize pulses of  $\sim 1$ -ns duration ( $\sim 1$  GHz wide) centered at the relevant probing frequencies. The system measures  $\tau(\omega)$  directly in the time domain. This technique provides a direct measurement and can easily discriminate parasitic reflections (by selecting the time window of the pulse reflected at the plasma). It also has access to high-power single-frequency sources. One of the drawbacks, however, is that those systems are difficult to sweep; thus, spatial sampling of the profile is limited to a number of discrete channels. A PR system has been operating for years in TEXTOR (Ref. 130).

A new technique, called ultrashort pulse reflectometry (USPR), was proposed in the mid-1990s (Ref. 131). The idea is to generate short voltage pulses (in the sub-ns range) with a broad spectrum (centered at  $\omega = 0$  instead of having a carrier as do the short pulse systems) that can directly cover a significant part of the density profile. The time of flight ( $\sim 1$  to 15 ns depending upon the device) is measured at a number of frequencies by using a filter array. The accuracy and robustness of profiles obtained using this technique have been investigated by Cohen et al.,<sup>132</sup> who incorporated O-mode and X-mode reflectometry simulation packages into the CORSICA plasma equilibrium and transport code and who carried out USPR simulations for the DIII-D tokamak and the SSPX spheromak.

One further step in the technique has been the use of dispersive waveguides to generate chirped pulses (different frequencies in the original pulse are differently delayed in time) and then use high-frequency amplifiers to generate a broadband IF signal. Typical parameters for the initial pulse are 5V, 65 ps such that after chirping and amplification, IFs on the order of 10 GHz result. The IF signals are then up-converted with different mixers and LOs, in order to provide full profile coverage.<sup>133</sup> Ultrashort pulse systems have been developed for LHD (Refs. 134 and 135) and SSPX (Ref. 136). A recent paper by Mase et al.<sup>137</sup> describes the system on LHD including its remote operation.

In the last 10 yr, technology has evolved in such a way that a number of the original limitations of some of these techniques have been clearly overcome and the differences between them have been removed to some extent: Fast inexpensive data acquisition allows for a simplification of the hardware (very sophisticated signal processing is performed digitally from a high-frequency sampled signal), new solid-state sources with

high spectral quality, high-frequency amplifiers, and a variety of developments. A discussion of novel applications of different data-processing technologies is presented in Ref. 138. The authors analyze different FM reflectometer analysis techniques: frequency discriminator, complex demodulation, maximum entropy method, “best path” technique, and “burst” analysis (whose original feature is to process together several profiles consecutive in time rather than individual ones).

Concerning the physics obtained from profile reflectometry, the last 10 yr has witnessed a very positive evolution. From a situation in which reflectometers were basically diagnostics “under development” targeted for their own technical improvement, currently density profiles from reflectometry are routinely available measurements, useful for the device exploitation. Results of ELM studies<sup>139</sup> and perturbative studies, like cold pulse propagation<sup>140</sup> and plasma position monitoring<sup>141</sup> (of interest for ITER), are particular examples, which can be added to the basic role of providing high-resolution (time and radius) density profiles available for every discharge.

In order to illustrate the quality and resolution of the density profiles obtained with reflectometry, we could take some representative examples. Figure 17 shows the time evolution of the density profile measured from the HFS on the ASDEX Upgrade device,<sup>119</sup> and Fig. 18 shows the changes in the density profile during the development of an ITB on the DIII-D tokamak.<sup>142</sup> Similarly, Fig. 19 shows the time evolution of the line-average density and the density profiles measured at different instants during a transition to improved confinement in the TJ-II stellarator.<sup>126</sup>

#### IV.C. Fluctuation Measurements

Reflectometry was from its very beginning an attractive candidate as a density fluctuation diagnostic, based on the conceptual idea of relating the oscillations of the reflected signal with displacements of the cutoff layer position. This interest was due to its modest requirements for access (single line of sight, small antennas) and hardware investment and to the potential for very high temporal and density resolution. The time resolution can easily achieve tens of MHz (active diagnostic with many photons launched and received), and the density resolution is linked to the capability of detecting very small displacements of the cutoff (as an illustration, in the ideal case of a mirror, displacements of a small percent of a wavelength, that is, a few microns, are measurable).

Another element of interest was derived from the difficulty to implement alternate methods for the measurement of density fluctuations inside the plasma. This has led to the paradox that most of the physics findings of reflectometry have been for years those related to qualitative fluctuation measurements (for example, the observation of turbulence suppression in the H-mode

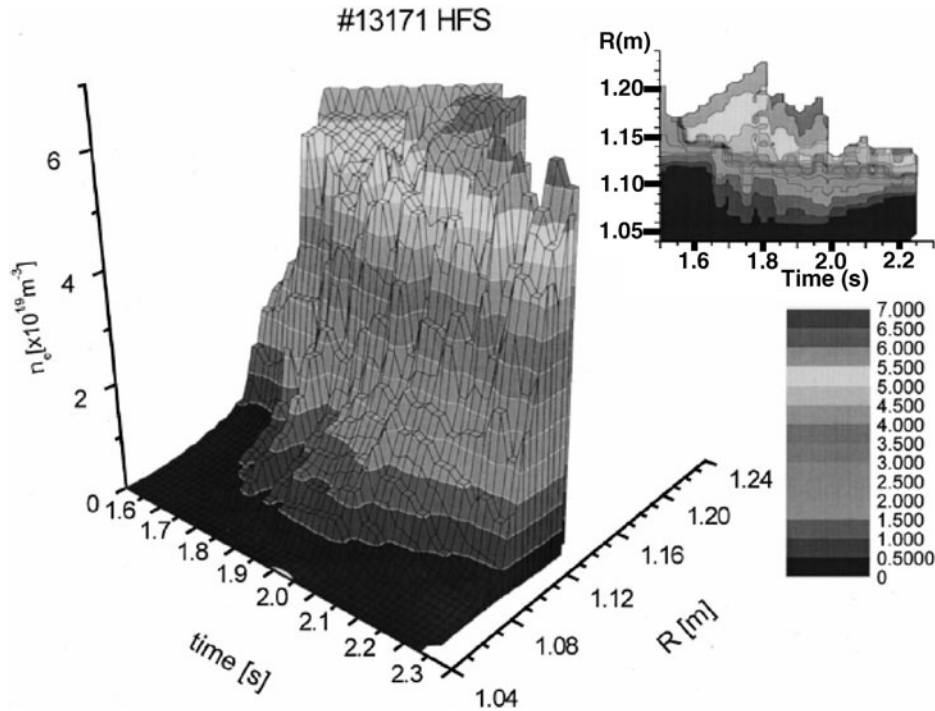


Fig. 17. Time evolution of the electron density profile measured with reflectometry from the HFS in ASDEX Upgrade. (From Silva et al., Rev. Sci. Instrum., Vol. 72, 2001)

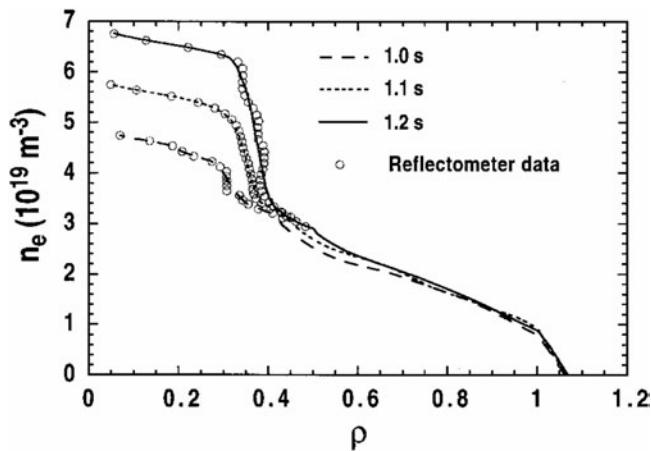


Fig. 18. Density profiles measured with reflectometry at different instants during the formation of an ITB on DIII-D. (From Zeng et al., Rev. Sci. Instrum., Vol. 72, 2001)

transition<sup>143–146</sup>) and not to profile reflectometry, which was much better understood from the theoretical aspect.

The basic measurement uses a fixed frequency with homodyne detection (see Fig. 20), which provides a signal of the type  $A \cdot \cos \phi$ , being the amplitude  $A$  (the product of the reference and received E-field amplitudes) and  $\phi$  (the phase delay of the probing beam). A second step is the use of heterodyne or homodyne quadrature detection

to measure separately the phase and amplitude of the reflected wave, and a further development is the use of two beams that reflect at nearby positions in order to perform correlation studies (either radial, by using collinear beams at nearby frequencies, or poloidal/toroidal, by using several lines of sight at the same frequency). In all approaches, a stepwise frequency sweep or a multi-channel system is used to probe different radial positions.

The interpretation based on Eq. (16) has been subject to significant controversy. The simplest approach of a “moving mirror,” suitable for fluctuations with long poloidal wavelength  $\Lambda_\theta$  (toroidal  $\Lambda_\phi$  is supposed to be large in all scenarios) and moderate radial wavelength  $\Lambda_r$  (several vacuum wavelengths of the probing beam), is compatible with Eq. (16). In this case, the density fluctuation  $\delta n$  is, even for large amplitudes, nearly linear with the phase fluctuations  $\delta\phi$ , and the spectra are similar. The fluctuation amplitude can be derived from Eq. (16) under some assumptions.<sup>113,147,148</sup> This moving mirror approach has been the basis for the successful observation of macroscopic fluctuations (Alfvén modes, MHD, etc.) either from single-frequency systems; multichannel systems; or even, in the more modern approaches, observation of radial macroscopic fluctuations by fast sweeping of a broad part of the profile (a by-product from fast profile measurements).

The moving mirror approach for microscopic turbulence has been challenged from several points. First, 1-D full-wave solutions of the wave equations,<sup>149</sup> as well as

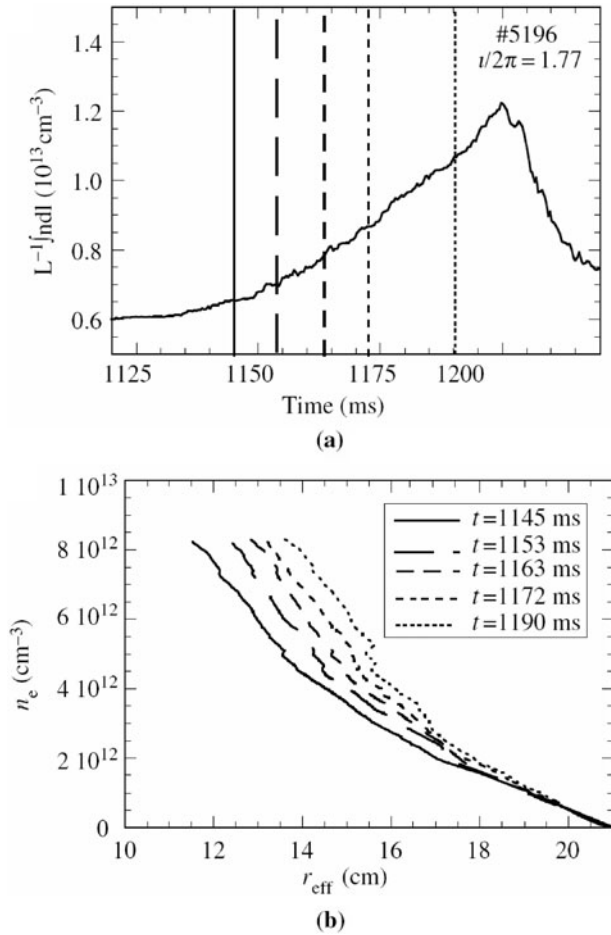


Fig. 19. Time evolution of (a) the line-average density and (b) the density profiles measured with reflectometry at different instants during a transition to improved confinement in the TJ-II stellarator. (From Estrada et al., *Plasma Phys. Control. Fusion*, **43**, 2001)

Born approximation models, show the traditional properties of wave scattering: Reflection is not perfectly localized at the cutoff layer, structures along the propagation path lead to local Bragg scattering away from the cutoff etc. Second, there is no reason for assuming a purely radial turbulence: Density structures are at least 2-D (radial/poloidal), and in most cases, even if the radial resolution of the system is sufficiently good (few mm for the X-mode for typical scenarios), the poloidal extension of the launched beam (several cm) is of the size of several wavelengths of the turbulence.

The first clear experimental observation of 2-D effects was the so-called “phase runaway,” a Doppler shift of the reflected beam caused by rotating density structures.<sup>150–152</sup> This requires a small departure of the beam from the ideal perpendicular geometry, which easily appears as soon as the plasma evolves. A second indication is the observation of anomalous short correlation

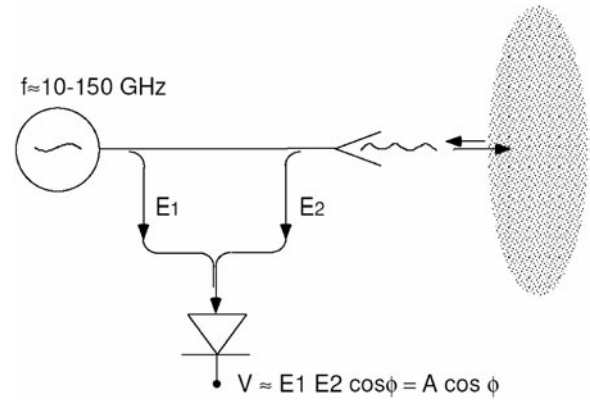


Fig. 20. Scheme of a homodyne reflectometer. A reference beam (E1) and the received probing beam (E2) are mixed at the detector diode to provide a signal whose alternating-current component is proportional to  $\cos \phi$  ( $\phi$  being the phase difference between reference and probing beams).

lengths for the radial turbulence, which can also be explained by the existence of 2-D structures.<sup>153</sup>

A number of studies have analyzed the effects of 2-D turbulence from different approaches: WKB multiray tracing,<sup>117</sup> physical optics,<sup>154</sup> phase screen,<sup>155</sup> and full-wave 2-D solutions either numerical<sup>156</sup> or analytical.<sup>157–159</sup> Most of them agree that the 1-D approach can work when the poloidal wavelength of the turbulence  $\Lambda_\theta$  is larger than the diameter  $D$  of the reflecting spot (area of the cutoff surface that contributes to the received reflected beam) or when, even with  $\Lambda_\theta < D$ , the amplitude of the density oscillations  $\delta n$  is small enough to generate small phase oscillations  $\delta \phi \ll 2\pi$  (thus keeping reflections from different positions of the reflecting spot coherent). A number of studies are devoted to determine, from the analysis of the reflectometer signal itself, whether or not the scenario is consistent with the simplified moving mirror interpretation.

For scenarios of strong turbulence with  $\Lambda_\theta < D$ , the information integrated at a single detector is clearly not sufficient to determine the entire description of the turbulence. Under these conditions, neither the turbulence amplitude nor its spectrum (which tends to appear broader for  $\delta \phi$  than it is for  $\delta n$ ) can be measured, and even qualitative measurements could be wrong (radial trends, etc). One way forward could be to aim for less demanding goals, like trying to derive integrated statistical properties of turbulence (speculative examples could be to determine the spectral width, average spectral frequency, or average wavelength of the turbulence). This would require in-depth studies with full-wave models, which still today are too time-consuming to run a full multiparameter dependence study with enough statistics. One established example of this line of work is the measurement of the Doppler shift of a tilted beam to

determine the rotation speed of the turbulence.<sup>160</sup> This has led during the last decade to an extensive field of research, “Doppler Reflectometry,” applied to plasmas (see Sec. IV.D).

The other way is to simplify the physics of the problem by using large aperture imaging systems, able to concentrate the beam in a small spot at the reflecting layer and to image this spot back at the detector. With such a system, the signal at the detector  $\delta\phi$  is again close to linear with the local density amplitude  $\delta n$ . This technology has been thoroughly analyzed and also implemented in several devices. The results are in line with the expectations. In practical terms, implementation of large aperture systems adds significant complexity to the diagnostic; increases the demand for access; and still has limitations concerning its capability to have a proper focus, which, in addition, needs to be displaced if several radial locations are to be probed. However, still the proposal is of high value if we are interested in a detailed description of the turbulence (see Sec. IX for details on microwave imaging reflectometry).

#### IV.D. Doppler Reflectometry

The Doppler shift of the reflected signal, caused by the existence of rotating corrugated structures at the cut-off layer, could be used to determine the plasma rotation velocity, thus opening a significant diagnostic potential. The fundamentals of the technique are derived from the same phenomenon that causes the phase runaway described above. In a first qualitative interpretation, the phase runaway would require either a nonperpendicular alignment of the antenna or a nonsymmetrical turbulence structure (sawtooth-like shape, for instance). In addition, it is assumed that fluctuations have zero average radial velocity, which agrees with experimental findings.

First attempts to provide a quantitative interpretation of the effect were made in Refs. 160 and 161. The corrugated layer behaves as a diffraction grating. The zeroth-order reflection will carry no Doppler shift, but the higher orders are reflected at nonsymmetric angles, therefore leading to a Doppler shift of the beam as seen by the receiver. Figure 21 shows a simplified scheme of the process.

In order to get the  $-1$ st order back to the receiver, with a tilt angle  $\theta_{\text{tilt}}$ , we need the Bragg condition to be fulfilled:  $K_{\perp} = 2k_0 \sin(\theta_{\text{tilt}})$ , where  $k_0$  is the wave vector of the beam and  $K_{\perp}$  is the wave vector of the turbulence. The Doppler shift at the receiver would be  $\Delta\omega = -2k_0 \sin(\theta_{\text{tilt}})v_{\text{perp}}$ ; thus, the fluctuation velocity  $v_{\text{perp}}$  can be determined from the measurement of  $\Delta\omega$  and the knowledge of the other parameters. Even though both  $\theta_{\text{tilt}}$  and the effective  $k_0$  at the reflecting point will be different from the vacuum values, both parameters evolve in such way that their variations cancel in the Bragg expression  $K_{\perp} = 2k_0 \sin(\theta_{\text{tilt}})$  and the value of  $K_{\perp}$  is unaffected in first order of approximation.<sup>160</sup>

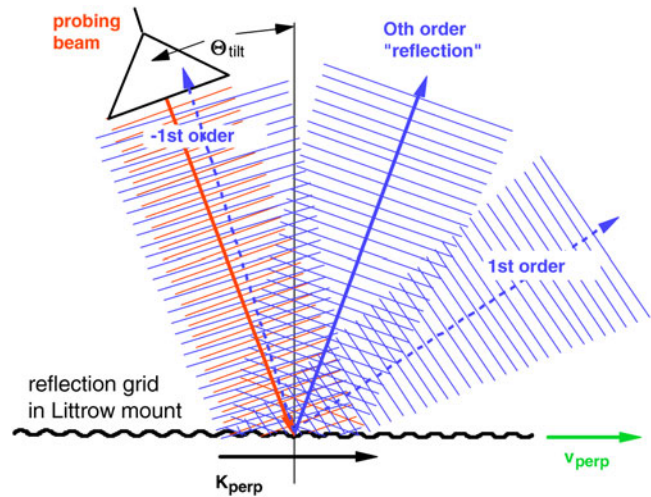


Fig. 21. The plasma cutoff as a moving diffraction grating: basic scheme. (From Ref. 161)

A more serious difficulty could come from the superimposition of several orders of diffraction (several  $K_{\perp}$  values reflecting with the same angle from different orders). This would not necessarily preclude the measurement of  $v_{\text{perp}}$ , since the relevant parameters are  $k_0$  and  $\theta_{\text{tilt}}$ , but a strong reflection from the zeroth order could reach the receiver because of the finite angular width of the antenna pattern. In this case, the level of perturbation would depend on the relative amplitude of this signal and that of the selected order at the receiver (typically  $-1$ st) and on the spectral width of the different phase spectra recorded. Actions that would minimize the effect would be the use of narrower beams and the increase of  $\theta_{\text{tilt}}$ , in order to avoid the strong zeroth order. On the other hand, a too narrow beam would reduce the resolution of the equivalent diffraction grating. This would not be very important concerning  $v_{\text{perp}}$  measurements, since only a good accuracy of  $\theta_{\text{tilt}}$  matters, but it would decrease the signal level from the nonzeroth orders, with the potential complete loss of the Doppler signal.

Typical values used in experiments are  $\theta_{\text{tilt}} \approx 10$  deg and the beam for frequencies 30 to 90 GHz ( $k_0 \approx 10 \text{ cm}^{-1}$ ) aiming at Bragg reflections for  $K_{\perp} \approx 5 \text{ cm}^{-1}$ , which are within the expected range  $K_{\perp} \rho_s \approx 0.5$ , traditional values for drift waves and ion temperature gradient (ITG) instabilities.<sup>162</sup>

The complex interplay of all the parameters have led to the development of comprehensive simulation codes<sup>161,163</sup> as well as analytical developments.<sup>164,165</sup> On the experimental side, different antenna configurations (monostatic versus bi-static antennas, normal horns versus Gaussian focused beams, symmetrical launchers, etc.) and detection technologies (homodyne, heterodyne, spectral filters, etc.) have been used. Of particular interest are the devoted experiments carried out in the W7-AS device,<sup>160,161,166,167</sup> using several antennas at different tilt

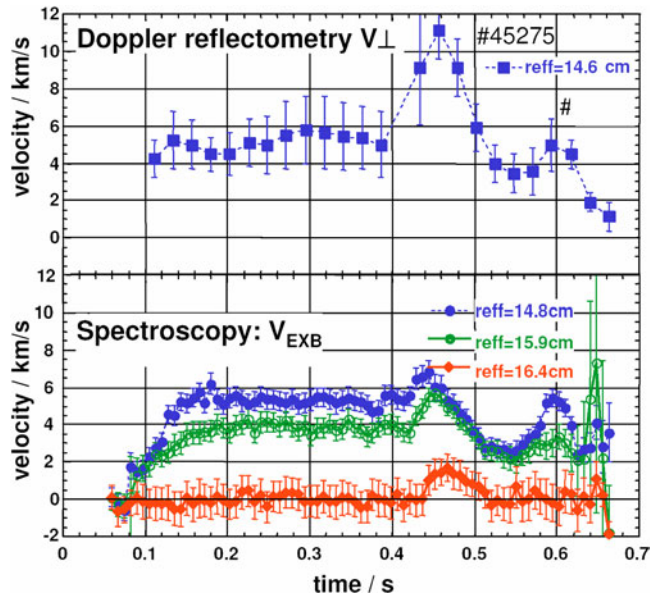


Fig. 22. Experiment in W7-AS. Comparison of perpendicular fluctuation rotation velocity measured by Doppler reflectometry and  $E \times B$  velocity measured by spectroscopy. Radial position of the different measurements is indicated. (Courtesy of M. Hirsch)

angles and showing the capabilities of the system to provide meaningful plasma rotation profiles (see Fig. 22). One of the added features was the use of two symmetrical launchers in order to separate phenomena (possible effects of “tilted” structure of the turbulence, as in a “blazed” diffraction grating) and also to improve the determination of the actual tilt angle. Also significantly relevant were the experiments in TUMAN3 (Ref. 168), ASDEX Upgrade (Ref. 162), Tore Supra (Ref. 169), and TJ-II (Ref. 170). As a summary, the experiments show good agreement between the reflectometry measurements of rotation and those obtained from other methods [charge-exchange recombination spectroscopy (CXRS) mainly]; good approximation between the fluctuation velocity and the fluid velocity (the “phase velocity” of the waves in the fluid is usually small compared to the  $E \times B$  drift velocity); and good resolution, both temporal (several  $\mu\text{s}$ , enough to see H-L back transitions<sup>166</sup>) and radial (on the order of 1 cm, able to resolve the velocity shear layer<sup>169</sup>). On the other hand operational limits for the system are observed. In some of the relevant physics scenarios, like H-mode or ITBs, regions of the plasma could not be measured because of the absence of turbulence (or significant reduction of it to  $K_{\perp}$  values too small to reflect the  $-1\text{st}$  order at finite angles.)<sup>162</sup>

#### IV.E. Applicability to a BPX

Reflectometry, as does other microwave diagnostics, offers significant advantages for a BPX. Access require-

ments are moderate, and the performance of plasma-facing components (metal antennas, with vacuum windows far away from the plasma) is not affected significantly by neutron radiation or sputtering due to the particles leaving the plasma.

There are specific difficulties related to the access to the plasma on a BPX. H-mode scenarios tend to have flat density profiles (which preclude reflection at the plasma center for the O-mode), and also, operation at very high  $T_e$  (with central  $T_e$  on the order of 30 keV) will create hollow profiles of the X-mode right-hand cutoff (thus creating “shadow” areas for the reflectometer) and lead to an enlargement of the frequency range where ECA takes place. In the particular case of ITER (Refs. 85 and 171), access to the plasma core in the H-mode is only possible for the left-hand X-mode, launched from the HFS (which is a problem even for the moderate access required).

In addition to the traditional applications of density profile and fluctuation measurements, there exist operation-related measurements like position control (as a backup to the magnetics, which might suffer from drifts in long pulses), density changes during ELMs, and MHD mode detection. Another application would be plasma rotation measurements, from Doppler reflectometry, which is of particular interest for a BPX, where rotation measurements from beam-based CXRS are difficult.

Finally, a potential application that has unfortunately not yet been thoroughly tested is the use of reflectometry in the divertor for the determination of the density profile along several lines and to derive the position of the ionization front. The main challenges here are the very high densities expected (with strong gradients) requiring frequencies above 300 GHz and the difficult access for a system that should have several parallel measurement lines.

## V. COLLECTIVE THOMSON SCATTERING

Sections V, VI, and VII are focused on the important technique of collective Thomson scattering (CTS). The fundamentals are contained in Ref. 10 while a detailed treatment of the formalism may be found in Ref. 172 together with experimental implementations.

### V.A. Introduction

Collective Thomson scattering is sensitive to a broad range of plasma parameters and hence is potentially capable of diagnosing these parameters. These parameters include electron density (fluctuations and absolute value), magnetic field (fluctuations, absolute value, and orientation), electron and ion temperatures, relative densities of ion species, and finally the ion velocity distributions. The broad range of sensitivities presents special challenges when analyzing CTS data. We return to this in Sec. VII.F. At millimeter-wave frequencies,

the interaction between waves and plasma are particularly strong, thereby enhancing the sensitivities of CTS to plasma parameters. Consequently, although CTS systems also employ far-infrared (FIR) frequencies, it is appropriate to also discuss CTS as a millimeter-wave diagnostic. In Sec. V, we sketch the theory of CTS and then proceed to discuss the diagnostic capabilities.

A plasma is a dielectric medium that can modify the propagation of electromagnetic waves substantially as compared with the situation in vacuum. The dielectric properties of the plasma depend on the state of the plasma, which, in the most general formulation, is given by the phase-space<sup>b</sup> distribution of ions and electrons, and the electric and magnetic fields. In the case of millimeter-waves in magnetically confined fusion plasmas, where the frequencies of the considered electromagnetic waves  $\omega$  are in the ranges of the electron cyclotron frequency  $\omega_{ce}$  and electron plasma frequency  $\omega_{pe}$ , the state of the ions does not significantly affect the dielectric properties of the plasma and can be ignored. However, the state of the ions does affect the state of the electrons, in particular their fluctuations. We will return to this point in Sec. VII. In the cold plasma approximation, the dielectric properties of the plasma depend only on the electric and magnetic fields and on the particle density and flux, i.e., the first two moments of the velocity distribution. In a more complete model, the dielectric properties depend also on higher-order moments of the velocity distribution; however, the sensitivity is highest to the lowest-order moments. Waves propagating in a plasma are associated not only with variations in the electric and magnetic fields, the electromagnetic fields of the wave, but also with variations in the distributions of particles. Thus, a wave in a plasma perturbs the dielectric properties of the plasma, giving the dielectric properties the same spatial and temporal variation as possessed by the wave. A millimeter-wave propagating across a plasma with a density wave in it would see a plasma with a spatially and temporally varying density, and hence ditto varying dielectric properties. The interaction of the millimeter-wave with the varying dielectric properties sets up a new wave, the scattered wave, satisfying the Bragg condition

$$\mathbf{k}^s = \mathbf{k}^i + \mathbf{k}^\delta$$

and

$$\omega^s = \omega^i + \omega^\delta, \quad (20)$$

where

$\mathbf{k}, \omega$  = wave vector and angular frequency, respectively

$s, i, \delta$  = scattered wave, the incident millimeter-wave, and the density wave, respectively.

<sup>b</sup>Phase-space is the six-dimensional space spanning position and velocity.

Here, we have suggested that the millimeter-wave was scattered off the density wave, but we might as well have considered that the density wave was scattered by the millimeter-wave. The millimeter-wave is largely transverse (the electric field of the wave is largely orthogonal to the wave vector) and is associated with very minor density fluctuations. However, its electric field perturbs significantly the dielectric properties the density wave experiences. Rather than viewing the process as that of one wave being scattered off the other, it is fruitful to recognize that the plasma has a slightly nonlinear dielectric response because the electromagnetic fields of the waves interact not only with the equilibrium particle distributions to give the linear dielectric response but also with the wave-induced perturbations to the particle distributions to give nonlinear responses. Because of this nonlinearity, waves do not propagate independently but interact and set up new waves.

### V.B. The Inhomogeneous Wave Equation for the Scattered Wave

To give us a rigorous starting point for the mathematical formulation of scattering, consider a collisionless plasma described by the Vlasov equation

$$\partial_t f + \mathbf{v} \cdot \partial_{\mathbf{r}} f + \mathbf{a} \cdot \partial_{\mathbf{v}} f = 0, \quad (21)$$

where the acceleration of a particle is given by

$$\mathbf{a} = \frac{q}{m} (\mathbf{E} + \mathbf{v} \times \mathbf{B}), \quad (22)$$

where  $\mathbf{v}$ ,  $q$ , and  $m$  are the particle velocity, charge, and mass, respectively. Assume that in the plasma there are two waves denoted by  $i$  and  $\delta$  that perturb all equilibrium quantities, denoted by superscript 0, by small amounts. Assume further that the equilibrium electric field is zero.

To first order in the small quantities, associated with waves  $i$  and  $\delta$ , we find the standard linear dielectric response, which for the  $i$ 'th wave is written

$$\mathcal{L} f^i = -\mathbf{a}^i \cdot \partial_{\mathbf{v}} f^{(0)}. \quad (23)$$

Here, we have introduced the operator

$$\mathcal{L} = \partial_t + \mathbf{v} \cdot \partial_{\mathbf{r}} + \frac{q}{m} (\mathbf{v} + \mathbf{B}^{(0)}) \cdot \partial_{\mathbf{v}}, \quad (24)$$

representing the time derivative along the unperturbed orbit of a particle. In the discussion of the interaction of two waves, we will need operators representing the linear dielectric response of the plasma. To obtain these, we solve for  $f^i$  in Eq. (23) by integrating along characteristics to get  $f^i = \mathcal{L}^{-1} \{-\mathbf{a}^i \cdot \partial_{\mathbf{v}} f^{(0)}\}$ . Multiplying by charge and velocity and integrating over velocity, we obtain the current induced in the plasma by the wave  $\mathbf{j}^i = \sigma^i \{\mathbf{a}^i \cdot \partial_{\mathbf{v}} f^{(0)}\}$ , where



$$\boldsymbol{\sigma}'\{\cdot\} = -q \int \mathbf{v} \mathcal{L}^{-1}\{\cdot\} d\mathbf{v} . \quad (25)$$

Assuming that the wave electric field is  $\mathbf{E}^i(\mathbf{r}, t) = \mathbf{E}^{i\omega} \exp\{i(\mathbf{k}^i \cdot \mathbf{r} - \omega^i t)\} + cc$  ( $cc$  is short for complex conjugate) and similarly for other wave quantities, then the current can be written

$$j_n^{i\omega} = \sigma_{nj} E_j^{i\omega} , \quad (26)$$

where the conductivity tensor  $\sigma_{nj}$  is given by

$$\sigma_{nj} e^{i(\mathbf{k}^i \cdot \mathbf{r} - \omega^i t)} = \sigma_n' \{ a_{lj}^i \cdot \partial_{v_l} f^{(0)} e^{i(\mathbf{k}^i \cdot \mathbf{r} - \omega^i t)} \} . \quad (27)$$

Summations over repeated lower indices are assumed. The tensor  $a_{lk}^i$  is defined by

$$(\mathbf{a}^{i\omega})_l = \frac{q}{m} \left( \mathbf{E}^{i\omega} + \frac{1}{\omega^i} \mathbf{v} \times (\mathbf{k}^i \times \mathbf{E}^{i\omega}) \right)_l = a_{lj}^i E_j^{i\omega} . \quad (28)$$

In the subsequent discussion, we will not retain the notation with superscript  $\omega$  to indicate complex amplitude; whether complex amplitude or real quantity is meant can be deduced from the context.

We will also need the wave tensor

$$\Lambda_{ij} = \varepsilon_{ij} + N^2 (\hat{k}_i \hat{k}_j - \delta_{ij}) , \quad N = \frac{kc}{\omega} \\ \varepsilon_{ij} = \delta_{ij} + \chi_{ij} , \quad \chi_{ij} = \frac{i\sigma_{ij}}{\omega \varepsilon_0} , \quad (29)$$

which enters the linear wave equation

$$\Lambda_{ij}^i E_j^i = 0 . \quad (30)$$

Turning now to the formulation of scattering, we retain terms to second order in the Vlasov equation giving

$$\mathcal{L} f^{(2)} + \mathbf{a}^{(2)} \cdot \partial_{\mathbf{v}} f^{(0)} = -(\mathbf{a}^i + \mathbf{a}^\delta) \cdot \partial_{\mathbf{v}} (f^\delta + f^i) , \quad (31)$$

where the quantities with upper index 2 are of second order and represent waves resulting from interaction of first-order terms. These terms include the interaction of a wave with itself, described by  $\mathcal{L} f^{(2i)} + \mathbf{a}^{(2i)} \cdot \partial_{\mathbf{v}} f^{(0)} = -\mathbf{a}^i \cdot \partial_{\mathbf{v}} f^i$  and similarly for  $f^{(2\delta)}$ . The second-order terms resulting from interaction between the two waves  $i$  and  $\delta$  are given by

$$\mathcal{L} f^s + \mathbf{a}^s \cdot \partial_{\mathbf{v}} f^{(0)} = -\mathbf{a}^i \cdot \partial_{\mathbf{v}} f^\delta - \mathbf{a}^\delta \cdot \partial_{\mathbf{v}} f^i , \quad (32)$$

where  $f^s = f^{(2)} - f^{(2i)} - f^{(2\delta)}$ . Solving for  $f^s$ , integrating to obtain the associated plasma current, and entering this in Maxwell's equations for the fields of wave  $s$ , we obtain the inhomogeneous wave equation for the scattered waves, that is, a wave equation with driving terms

$$\Lambda^s \mathbf{E}^s = \frac{-i}{\omega^s \varepsilon_0} \mathbf{j}^\sigma \quad (33)$$

with the source current given by

$$\mathbf{j}^\sigma = \boldsymbol{\sigma}' \{ \mathbf{a}^i \cdot \partial_{\mathbf{v}} f^\delta + \mathbf{a}^\delta \cdot \partial_{\mathbf{v}} f^i \} . \quad (34)$$

Comparing Eqs. (32) and (23), or Eqs. (33) and (30), we note that in addition to the linear plasma response to the waves  $s$ , there are additional driving terms due to the bilinear interaction of the waves  $i$  and  $\delta$ . The wave  $s$  is produced by these driving terms. It is the result of scattering. We note that the drive is due to the fields of one first-order wave driving second-order currents by acting on the first-order velocity distribution perturbations associated with the other first-order wave.

To find the wave vectors and frequencies of the scattered waves, we separate out the phasors of the interacting waves in Eq. (33) and find

$$(\exp\{i(\mathbf{k}^i \cdot \mathbf{r} - \omega^i t)\} + cc)(\exp\{i(\mathbf{k}^\delta \cdot \mathbf{r} - \omega^\delta t)\} + cc) \\ = (\exp\{i(\mathbf{k}^{s+} \cdot \mathbf{r} - \omega^{s+} t)\} + cc) \\ + (\exp\{i(\mathbf{k}^{s-} \cdot \mathbf{r} - \omega^{s-} t)\} + cc) , \quad (35)$$

where

$$\mathbf{k}^{s\pm} = \mathbf{k}^i \pm \mathbf{k}^\delta ; \quad \omega^{s\pm} = \omega^i \pm \omega^\delta . \quad (36)$$

Thus, we find that  $s$  consists of two waves with wave vectors and frequencies that are, respectively, the sum and the differences of the wave vectors and frequencies of the interacting waves. In scattering experiments, one of the interacting waves is typically injected into the plasma as a probe; let this be wave  $i$ , to obtain information about another wave (often part of a distribution of waves); let this be wave  $\delta$ . The information is obtained by detecting one of the two scattered waves  $s$ . Inferences about  $\delta$  are, in principle, not affected by which of the scattered waves is detected. In such experiments,  $(\mathbf{k}^i, \omega^i)$  and  $(\mathbf{k}^\delta, \omega^\delta)$  are controlled and presumed to be known. This resolves the wave in the plasma with the wave vector and frequency

$$(\mathbf{k}^\delta, \omega^\delta) = \pm(\mathbf{k}^s - \mathbf{k}^i, \omega^s - \omega^i) . \quad (37)$$

Note that  $(\mathbf{k}^\delta, \omega^\delta)$  and  $(-\mathbf{k}^\delta, -\omega^\delta)$  are of course the same wave, so the  $\pm$  is dropped.

In the limit where thermal effects can be ignored at the frequency and wave vector of the scattered wave (for a more precise definition of the conditions, see Ref. 114), the integrand in the velocity integrals in the operator  $\boldsymbol{\sigma}'$ , defined in Eq. (25), can be expanded in powers of velocity and the integrals carried out to yield the following expression for the source current involving only zeroth and first-order moments of  $f^i$  and  $f^\delta$ :

$$j_i^\sigma = \frac{\sigma_{il}^s}{n^{(0)}} \left\{ n^i E_l^\delta + n^\delta E_l^i + \epsilon_{lmn} (\Gamma_m^i B_n^\delta + \Gamma_m^\delta B_n^i) + Y_{imn}^s \frac{1}{c} (\Gamma_m^i E_n^\delta + \Gamma_m^\delta E_n^i) \right\}. \quad (38)$$

The lowest-order moments entering here are defined as

$$n^{i,\delta} = \int f^{i,\delta} d\mathbf{v},$$

and

$$\Gamma_i^{i,\delta} = \int v_i f^{i,\delta} d\mathbf{v}. \quad (39)$$

The tensor  $\epsilon_{lmn}$  is the Levi-Cevita symbol (equal to 1 if  $lmn$  is a positive permutation of 1 2 3,  $-1$  if  $lmn$  is a negative permutation and 0 otherwise). The tensor  $Y_{imn}^s$ , which depends on  $\omega^s$ ,  $\mathbf{k}^s$ , and  $\omega_{ce}$ , is given in Ref. 173. For typical CTS setups with millimeter-waves, it is generally of order unity.

Consider again a transverse millimeter-wave used as the probe wave  $i$  scattering off, or interacting with, a density wave  $\delta$ . In this case, the dominant term in the source current expression Eq. (38) is the one representing the electric field of the probe wave interacting with the density perturbation of the density wave, and the source current would take the simple approximate form

$$j_i^\sigma \approx \sigma_{ii}^s n^\delta E_l^i / n^{(0)}. \quad (40)$$

This result could almost be derived from a simple cold fluid picture where the field of the probe wave interacts with a cold plasma with a density perturbation—*almost* because this approach, unless additional considerations outside the cold plasma description are introduced, leads to the result that the conductivity tensor should be evaluated at the frequency and wave vector of the probe wave.<sup>114</sup>

In many situations, this difference is small. Consider now a situation where the wave  $\delta$  is the fast magnetosonic wave. In this wave, both the density and magnetic field fluctuate significantly, and it turns out<sup>174</sup> that the terms in the source current associated with the density and magnetic field fluctuation in  $\delta$  can be of similar amplitude. Note that it is the induced particle flux  $\Gamma^i$  of the probe wave that probes the magnetic fluctuations of the wave  $\delta$ . The phase relation between the induced particle flux and the electric field of wave  $i$  depends on the mode (O-mode or X-mode) of wave  $i$  and the frequency relative to the cyclotron frequency. For X-mode at a frequency below the electron cyclotron frequency, this phase relation is such that for scattering off the fast magnetosonic wave, the terms  $n^\delta E_l^i$  and  $\epsilon_{lmn} \Gamma_m^i B_n^\delta$  are almost exactly out of phase for scattering into X-mode (expressions accounting for the mode being scattered into follow below). Moreover, the two terms are almost equal in

amplitude so that the sum is much smaller than its parts. This was the situation experienced with the fast ion CTS at TFTR, and this effect caused a reduction in the scattering cross section of approximately two orders of magnitude<sup>174</sup> as compared with the scattered power predicted if only scattering off density perturbations was included or the scattering of density and magnetic fluctuations is considered uncorrelated. In this situation, several of the remaining terms in the source current expression Eq. (38) must be retained.

### V.C. The Equation of Transfer for a Scattering System

We turn now to extending the expressions to account for the coupling of the source current to propagating modes in the plasma, for the propagation of the probe from the launching antenna to the scattering volume, and for the propagation of the received scattered radiation from the scattering volume to the receiving antenna. Scattering, of course, takes place all along the probe, but the received scattered radiation comes from a limited volume, the scattering volume, where the probe and receiver beam patterns intersect.

To derive these expressions, we solve for  $\mathbf{E}^s$  in Eq. (33) and take the ensemble average of the square of  $\mathbf{E}^s$ , which reflects the fact that in experiments we generally only measure the spectral power density of the scattered waves, not the fields with phase information. This also allows us to reduce the complexity of the description of the fluctuations  $\delta$  to ensemble averages of squared terms, i.e., the spectral power density of the fluctuations. We then account for the transfer of power through an anisotropic, inhomogeneous plasma in the WKB approximation.<sup>27</sup> Finally, we rewrite  $n^i$ ,  $\mathbf{B}^i$ , and  $\Gamma^i$  in terms of  $\mathbf{E}^i$ . Through these steps, we find that the equation of transfer for a scattering system<sup>114</sup> giving the spectral power density received by a diffraction limited receiver is given by

$$\frac{\partial P^s}{\partial \omega^s} = P^i O_b (\lambda_0^i)^2 r_e^2 n^{(0)} \frac{1}{2\pi} \Sigma, \quad (41)$$

where

$P^i$  = incident power

$\lambda_0^i = \omega^i / c$

$r_e = q_e^2 / 4\pi\epsilon_0 m_e c^2$  and is the classical electron radius

$O_b$  = beam overlap and is the spatial integral of the product of the normalized beam intensities [ $\mathcal{I}(P^i \mathcal{I}^i(\mathbf{r}))$  is the local power density in the probe beam], where

$$O_b = \int \mathcal{I}^i(\mathbf{r}) \mathcal{I}^s(\mathbf{r}) d\mathbf{r}. \quad (42)$$

$O_b$  will have some frequency dependence because of re-fraction, but most of the frequency variation is in the scattering function  $\Sigma$  defined as

$$\Sigma = \sum_{\alpha\beta} \Sigma_{\alpha\beta} , \quad \Sigma_{\alpha\beta} = \frac{(\omega^s)^4}{\omega_{pe}^4} \frac{1}{S^i S^s} \hat{G}_i^{(\alpha)} \langle \alpha_i \beta_j \rangle \hat{G}_j^{(\beta)*} \quad (43)$$

with  $\alpha_i, \beta_i = n, E_i, B_i, \Gamma_i$  the fluctuation quantities associated with the waves  $\delta$ . Not to burden the notation, we drop the superscript  $\delta$ . The coupling operators  $\hat{G}_i^{(\alpha)}$  account for how efficiently the source currents, associated with interaction of the probe wave with a given part of the fluctuations (e.g., the density  $n$ ), radiate a scattered wave. The coupling operators are given by

$$\hat{G}_k^{(n)} = (e_i^s)^* \chi_{il}^s e_l^i , \quad (44)$$

$$\hat{G}_k^{(B)} = (e_i^s)^* \chi_{ij}^s \epsilon_{jmk} \frac{i\omega^i \epsilon_0}{q_e} \chi_{ml}^i e_l^i , \quad (45)$$

$$\hat{G}_k^{(\Gamma)} = (e_i^s)^* \chi_{ij}^s \left( \epsilon_{jkm} \epsilon_{mnl} \frac{k_n^i}{\omega^i} + Y_{jkl}^s \frac{1}{c} \right) e_l^i , \quad (46)$$

and

$$\hat{G}_k^{(E)} = (e_i^s)^* \frac{i\epsilon_0}{q_e} \chi_{ih}^s \left( \delta_{hk} k_j^i + Y_{hjl}^s \frac{\omega^i}{c} \right) \chi_{jl}^i e_l^i . \quad (47)$$

The normalized flux and normalized field vectors are given by

$$S = N |\hat{\mathbf{k}} - \text{Re}\{(\hat{\mathbf{k}} \cdot \mathbf{e}) \mathbf{e}^*\}| ,$$

$$\mathbf{e} = \mathbf{E}/|\mathbf{E}| ,$$

and

$$\hat{\mathbf{k}} = \mathbf{k}/k , \quad k = |\mathbf{k}| , \quad N = kc/\omega . \quad (48)$$

All quantities in  $\Sigma$  refer to the conditions in the scattering volume.  $\langle \alpha_i \beta_j \rangle$  is the ensemble average of two quantities in the fluctuations from which the probe is scattering. The diagonal terms in the scattering function, e.g.,  $\Sigma_{nn}$  or  $\Sigma_{BB}$ , are positive definite, whereas the off-diagonal terms, e.g.,  $\Sigma_{nB}$ , can be negative. It is the off-diagonal elements in the sum in Eq. (43) that account for the phase relationships between scattering off different types of fluctuations. These terms were negative in the case discussed above where X-mode with  $\omega^i < \omega_{ce}$  was scattered off the fast magnetosonic wave.

Consider now the scattering function accounting only for scattering off density fluctuations. From Eqs. (43) and (44), we see that it has the form

$$\Sigma_{nn} = \frac{(\omega^s)^4}{\omega_{pe}^4} \frac{1}{S^i S^s} |(e_i^s)^* \chi_{il}^s e_l^i|^2 \langle nn \rangle . \quad (49)$$

For a scattering geometry where both the probe and received scattered radiation propagate perpendicular to the magnetic field in the scattering volume and where one is in O-mode and the other in X-mode, then  $|(e_i^s)^* \chi_{il}^s e_l^i| = 0$ , and the scattering off density fluctuations, normally the dominant term, vanishes. In this case, fluctuations in other quantities, in particular the magnetic field, can be measured even if these are not particularly strong as in the case of fluctuations associated with the fast magnetosonic wave. From the expressions Eqs. (43) and (45), we can write the scattering function accounting for scattering off magnetic fluctuations only:

$$\Sigma_{BB} = \frac{(\omega^s)^4}{\omega_{pe}^4} \frac{1}{S^i S^s} \left( \frac{\omega^i \epsilon_0}{q_e} \right)^2 \{ (e_i^s)^* \chi_{ij}^s \epsilon_{jmk} \chi_{ml}^i e_l^i \} \times \langle B_k B_{k'} \rangle \{ (e_i^s)^* \chi_{ij}^s \epsilon_{jmk'} \chi_{ml}^i e_l^i \}^* . \quad (50)$$

It should be noted that scattering off flux or electric field fluctuations can also dominate and hence determine what can be measured with a particular scattering arrangement. The expressions in Eqs. (43) through (48) can be used to determine which is the case and thereby form the basis for interpretation of data.

## VI. APPLICATION OF COLLECTIVE SCATTERING TO THE DIAGNOSIS OF MACROSCOPIC OR TURBULENT FLUCTUATIONS

### VI.A. Wave Number ( $k$ )-Resolved Collective Scattering

#### VI.A.1. Theory

In the vast majority of collective scattering experiments for measuring nonthermal (turbulent) density fluctuations or coherent electrostatic waves, the scattered radiation is detected using the well-known method of optical mixing. By mixing the scattered signal with an LO, the amplitude and phase of the scattered radiation are preserved, and the frequency spectrum is transformed down to a convenient frequency range, where it can be analyzed by numerical or electronic processing with good spectral resolution. Theoretical treatments of coherent detection of collectively scattered radiation have been given by a number of authors.<sup>175–178</sup> In the following, a brief review of the primary theoretical result of CTS with coherent detection is presented. This will permit a correct assessment of the performance of such scattering experiments together with the interpretation of scattering results. For more details, the reader is referred to the excellent references listed above as well as Chapter 4, “Laser-Aided Plasma Diagnostics,” by A. J. H. Donné, C. J. Barth, and H. Weisen, in this special issue of *Fusion Science and Technology*, for laser implementations.

The geometry of a typical scattering experiment employing coherent detection is shown in Fig. 23.

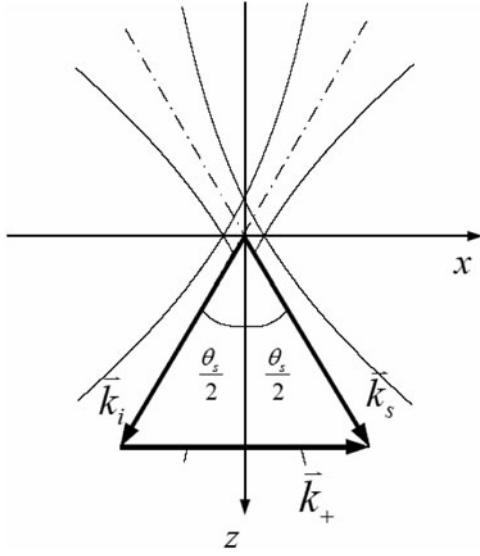


Fig. 23. Schematic of a scattering experiment with coherent detection.

An incident electromagnetic wave characterized by angular frequency  $\omega_i$ , wavevector  $\vec{k}_i$ , and electric field  $\vec{E}_i(\vec{r}) = \vec{E}_{i0} U(\vec{r}) e^{i\vec{k}_i \cdot \vec{r}}$  is scattered by electron density fluctuations  $\tilde{n}(\vec{k}, \omega)$ . The scattered radiation  $(\vec{k}_s, \omega_s)$  propagating along the antenna beam wave vector  $\vec{k}_l$  ( $k_l \approx k_s$ ) of the coherent (homodyne or heterodyne) receiver is received and mixed with the LO, ( $\vec{E}_l(\vec{r}) = \vec{E}_{l0} U_l(\vec{r}) e^{i\vec{k}_l \cdot \vec{r} - i\omega_l t}$ ), in a nonlinear element (the mixer). For the sake of simplicity, it is assumed here that the incident and scattered waves are both ordinary mode (O-mode) with frequencies well above the O-mode cut-off frequency,  $\omega_{i,s,l} \gg |\omega_l - \omega_i|, |\omega_s - \omega_i|$ , and  $\vec{k}_s$  is perpendicular to  $\vec{E}_i$ . The spectral power density of the beating current of the mixer output is then given by

$$P(\omega) = \frac{\gamma^2}{T} \{ |\hat{n}(\vec{k}_+, \omega - \omega_\Delta)|^2 + |\hat{n}(\vec{k}_-, -\omega - \omega_\Delta)|^2 \}, \quad (51)$$

where

$$\begin{aligned} \gamma &= \frac{1}{2} r_e \lambda_i R_d \sqrt{\frac{\epsilon_0}{\mu_0}} E_{i0} E_{l0}, \\ \vec{k}_+ &= \vec{k}_s - \vec{k}_i, \quad \vec{k}_- = -\vec{k}_+ = \vec{k}_i - \vec{k}_s, \\ \omega_\Delta &= \omega_l - \omega_i, \\ \hat{n}(k_+, \omega) &= \int d\vec{r} n(\vec{r}, \omega) U(\vec{r}) e^{-i\vec{k}_+ \cdot \vec{r}} \\ &= \int \frac{d\vec{k}}{(2\pi)^3} n(\vec{k}, \omega) W(\vec{k} - \vec{k}_+), \end{aligned} \quad (52)$$

$$\begin{aligned} n(\vec{k}, \omega) &= \int dt e^{i\omega t} \int d\vec{r} \tilde{n}(\vec{r}, t) e^{-i\vec{k} \cdot \vec{r}} \\ &= \int d\vec{r} \tilde{n}(\vec{r}, \omega) e^{-i\vec{k} \cdot \vec{r}}, \end{aligned} \quad (53)$$

$$W(\vec{k}) = \int d\vec{r} U(\vec{r}) e^{-i\vec{k} \cdot \vec{r}}, \quad (54)$$

and

$$U(\vec{r}) = U_i(\vec{r}) U_l^*(\vec{r}). \quad (55)$$

In the above,  $r_e, \lambda_i, R_d, \sqrt{\mu_0/\epsilon_0}, U_i(\vec{r}), U_l(\vec{r})$  are, respectively, the classical electron radius, incident wavelength, detector responsivity, characteristic impedance of free space, and normalized profiles of incident and antenna beams.

Introducing the scattering volume  $V_s = \int d\vec{r} |U(\vec{r})|^2$ , the spectral power density can be rewritten as

$$P(\omega) = r_e^2 \lambda_i^2 R_d^2 n_0 V_s \frac{P_i P_l}{A_i A_l} \hat{S}_{UT}(\vec{k}, \omega), \quad (56)$$

where

$$\begin{aligned} \hat{S}_{UT}(\vec{k}, \omega) &= \frac{1}{n_0 V_s T} \{ |\hat{n}(\vec{k}_+, \omega - \omega_\Delta)|^2 \\ &\quad + |\hat{n}(\vec{k}_-, -\omega - \omega_\Delta)|^2 \} \end{aligned} \quad (57)$$

is the dynamic form factor relative to the scattering volume  $V_s$  observed during the time interval  $T$ ,  $n_0$  is the mean density in the volume  $V_s$ , and  $P_i/A_i (P_l/A_l)$  is the mean intensity of the incident (antenna) beam in the volume. Note that the proportionality of the current power spectrum  $P(\omega)$  to  $\lambda_i^2$  derives from the antenna theorem for a coherent detection receiver, which states that the integrated effective aperture for a coherent detection receiver is limited by  $A_R \Omega_R \approx \lambda^2$  (Ref. 179). Equation (56) shows the important features of coherent detection in scattering experiments where the spectral power density  $P(\omega)$  reproduces the spectrum of density fluctuations at a wave vector  $\vec{k}_+$  fixed by the scattering geometry and the fluctuations propagating in opposite directions can be distinguished from the spectrum by a frequency offset  $\omega_\Delta \neq 0$  (heterodyne detection). Moreover, it should be noted from Eq. (52) that the measured fluctuation spectrum is convolved with the weighting function  $W(\vec{k})$ . Thus, the measured spectrum  $\hat{S}(\vec{k}, \omega)$  in a scattering experiment will normally cover a range of  $\vec{k}$ -vectors determined by the weighting function  $W(\vec{k} - \vec{k}_+)$ . It can be seen from Eq. (54) that only in the limiting case of  $V_s \rightarrow \infty$  and  $U(\vec{r}) = 1$  does the weighting function  $W(\vec{k} - \vec{k}_+)$  reduce to a delta function  $(2\pi)^3 \delta(\vec{k} - \vec{k}_+)$  so that a single wave vector  $\vec{k} = \vec{k}_+$  in the spectrum  $\hat{S}_{UT}(\vec{k}, \omega)$  is measured. Hence, the weighting function  $W(\vec{k} - \vec{k}_+)$  can be regarded as a bandpass

filter in  $\vec{k}$ -space with an effective bandwidth  $\vec{k}_+ \pm \Delta\vec{k}$ , and the measured spectrum  $\hat{n}(\vec{k}_+, \omega)$  of fluctuations is an average of  $n(\vec{k}, \omega)$  within the bandwidth. Here,  $\Delta\vec{k}$  is the wave number resolution that is defined as the distance in  $\vec{k}$ -space between the maximum of  $|W(\vec{k} - \vec{k}_+)|^2$  and its  $1/e$  value. Since the weighting function  $W(\vec{k} - \vec{k}_+)$  is related to the weighting function  $U(\vec{r})$  in real space via a Fourier transform, the wave number resolution is determined by the dimensions of the scattering volume.

When the weighting function  $U(\vec{r})$  is known, quantitative expressions for the weighting function  $W(\vec{k})$  can be calculated. For microwave coherent scattering, the antenna radiation pattern is given to a good approximation by a Gaussian function.<sup>180,181</sup> Thus, it is assumed here that both the incident and receiver antenna beams have Gaussian profiles with the same beam waist  $w$  at the scattering volume center and their wave fronts in the scattering volume are approximately planar. Using the scattering geometry and coordinate system illustrated in Fig. 23, the weighting function in real space can be written as

$$U(\vec{r}) = \exp\left[-\frac{2}{w^2}\left(x^2 \cos^2 \frac{\theta_s}{2} + y^2 + z^2 \sin^2 \frac{\theta_s}{2}\right)\right]. \quad (58)$$

Since the scattering volume is determined by the intersection of the incident beam and receiver antenna beam, the transverse spatial resolution is determined by the beam waist diameter  $2w$ , and the longitudinal spatial resolution is determined by the scattering length along the  $\vec{k}_i$  direction,  $l_s = 2w/\sin \theta_s \approx 2w/\theta_s$  (for  $\theta_s \leq 30$  deg). Substitution of Eq. (58) into Eq. (54) and subsequent integration gives the weighting function  $W(\vec{k} - \vec{k}_+)$  as

$$\begin{aligned} W(\vec{k} - \vec{k}_+) &= \frac{\pi^{3/2} w^3}{\sqrt{2} \sin \theta_s} \\ &\times \exp\left[-\frac{w^2(k - k_{+x})^2}{8 \cos^2(\theta_s/2)} - \frac{w^2 k_{+y}^2}{8} - \frac{w^2 k_{+z}^2}{8 \sin^2(\theta_s/2)}\right], \end{aligned} \quad (59)$$

where it is assumed that the measured wave vector  $\vec{k}$  is aligned along the  $x$ -axis. The weighting function  $W(\vec{k} - \vec{k}_+)$  represents the wave vector matching condition. In the case of scattering from a coherent wave, this simply means that the scattered power approaches a maximum for the case of perfect matching ( $k_{+x} = k$  and  $k_{+y} = k_{+z} = 0$ ) and decays as a Gaussian function as the wave vector of the plasma wave diverges from the wave vector  $\vec{k}_+$  set by the scattering geometry ( $\vec{k} \neq \vec{k}_+$ ). From Eq. (59), it can be seen that the 1-D wave number resolution is given by

$$\Delta k_x = \pm 2 \cos(\theta_s/2)/w \approx \pm 2/w \quad (\text{for } \theta_s \leq 30 \text{ deg}),$$

$$\Delta k_y = \pm 2/w,$$

and

$$\Delta k_z = \pm 2 \sin(\theta_s/2)/w \approx \pm \theta_s/w \quad (\text{for } \theta_s \leq 30 \text{ deg}).$$

(60)

Thus, the transverse wave number resolution is determined by the beam size (waist radius  $w$ ) and is independent of the beam wavelength chosen. This is precisely the same wave number extent determined by the divergence angle  $\Delta\theta_s = \theta_d = \lambda_i/(\pi w)$  of a Gaussian beam due to diffraction effects. The longitudinal wave number resolution is determined by the length of the scattering volume and is dependent upon the beam wavelength chosen through the Bragg condition. Therefore, the spatial resolution cannot be improved arbitrarily by reducing the beam size without loss in the transverse wave number resolution and the measurable minimum wave number  $k_{\min} \approx 4/w$ . However, the spatial resolution in the  $\vec{k}_i$  direction can be improved by increasing the probe beam wavelength and thus the scattering angle without loss in  $k_{\min}$  and the wave number resolution. The choice of a long-wavelength microwave or millimeter wave signal as the probe beam results in a good compromise between spatial resolution and wave number resolution. The resultant large scattering angle permits the realization of a multichannel system in those devices where the requisite spatial access is available. Moreover, a long-wavelength probe beam also results in an improvement in the signal-to-noise ratio.<sup>175</sup> For the ordinary mode (O-mode), the wavelength is limited by a cutoff at the plasma frequency and refraction from density gradients, which causes distortion of the ray paths. However, in recent years there has been interest in using the extraordinary mode (X-mode) as the probe beam to overcome the limitation imposed by the O-mode cutoff.<sup>182</sup> The use of a long-wavelength X-mode probe beam allows the scattering system to operate in higher-density plasmas than possible with O-mode, in addition to the improvement in the spatial resolution. The single-particle scattering cross section of the X-mode is no longer the familiar dipole radiation pattern, because of its elliptically polarized nature. Its scattering cross section depends upon the propagation angle of the incident and scattered beams to the local magnetic field and the ratios  $\omega_{pe}/\omega_i$  and  $\omega_{ce}/\omega_i$  ( $\omega_{pe}$ ,  $\omega_{ce}$  being the electron plasma and cyclotron frequency, respectively).<sup>183–186</sup> In addition, beam refraction must be accounted for in determining the location of the scattering volume, the detected  $k$  value, and the apparent solid angle. In this case, the effects of the plasma dielectric properties should be taken into account. Hughes and Smith have derived a generalized coherent scattering formula<sup>187</sup> that includes cases where the incident and scattered waves are near frequencies corresponding to resonances

or cutoffs and both waves are not necessarily the same mode.

As discussed above, the major disadvantage of collective scattering measurements is the poor longitudinal spatial resolution, especially at small wave numbers. Although it can be improved by using a long-wavelength probe beam, it is still unsatisfactory for spatially localized measurements of density fluctuations in large tokamaks, in particular in devices such as ITER, where most of the turbulent activity occurs at relatively low wave numbers. For advancing our understanding of plasma turbulence and transport, further improvement in the longitudinal spatial resolution is needed. Various methods for modifications of the basic collective scattering technique have been proposed and demonstrated with the aim of improving the spatial resolution of the measurements. The Tore Supra group<sup>188,189</sup> has used a technique that is based upon the variation of the magnetic pitch angle along the plasma diameter in the poloidal plane, combined with the fact that the turbulent wave vectors are dominantly oriented in a direction perpendicular to the local magnetic field, to improve the spatial resolution of small angle scattering measurements.

According to the wave vector matching condition, only when the wave vector  $\vec{k}_+$  (set by the scattering geometry) coincides with the turbulence wave vector  $\vec{k}$  will the turbulence be detected with maximum sensitivity. Variations of magnetic field pitch angles  $\theta_p$  result in rotation of the plane of the turbulence wave vector  $\vec{k}$  along the probe beam. Thus, the scattering power for the observed wave vector  $\vec{k} = \vec{k}_+$ , which is at an angle  $\beta$  to the poloidal plane, is given by

$$P(k, \beta) = \int dz |n(k, z)|^2 \exp[-(\beta - \theta_s(z))^2 / \Delta\beta^2], \quad (61)$$

where  $\Delta\beta = \Delta k/k = 2/(wk)$  is the effective angular resolution. It can be seen that for the localization to be possible, it is required that the inequality  $\theta_p > \Delta\beta$  be satisfied. The technique can produce quite good spatial resolution at larger wave numbers associated with the electron temperature gradient (ETG) mode in toroidal magnetically confined plasmas. However, the spatial resolution is wave number dependent and remains poor at the small wave numbers associated with the ITG mode. Moreover, the technique is very advantageous for infrared or FIR laser scattering experiments.

Another technique utilizes the effect of an inhomogeneous radial electric field on the scattered spectra to obtain improved spatial resolution for turbulence measurements. When the scattered frequency is dominated by the local  $\vec{E}_r \times \vec{B}$  Doppler shift, the large and inhomogeneous Doppler shift can be used to localize the measurement and thereby deduce the spatial profile of the turbulent fluctuation level when the profile of the radial

electric field is measured. The spatial resolution of this technique is determined by the scale length of the radial electric field. This technique was used to distinguish edge fluctuations from core fluctuations in DIII-D H-mode discharges.<sup>190–192</sup> However, it can only be applied to discharges with a large gradient in the radial electric field.

Recently, Mazzucato<sup>193</sup> proposed a new approach for high-spatial-resolution measurements that relies upon changes in the direction of the toroidal magnetic field along the tangential direction of the magnetic flux surface in the equatorial plane, combined with the turbulent wave vectors being locally perpendicular to the magnetic field. The spatial resolution depends on the factor  $R/(wk)$ , where  $R$  is the toroidal curvature radius of the magnetic flux surface. Moreover, the spatial resolution is best when the range of scattering angles for the measured wave number spectra of fluctuations is small, which means that for a given wave number to be measured, the smaller the scattering angle, the better the spatial resolution. This favors the use of a high-frequency probe wave, such as a millimeter wave source or FIR laser (perhaps even infrared laser). This technique can result in highly localized fluctuation measurements even at longer turbulent wavelengths. A microwave scattering system employing this method for high-resolution measurements of  $\rho_e$  scale turbulence has been installed on NSTX for ETG studies<sup>194,195</sup> and recently commissioned.

The scattered radiation can be detected by either heterodyne or homodyne detection methods. In the heterodyne detection scheme, the scattered radiation is mixed with an LO reference that is frequency shifted with respect to the probe beam. The spectral power density of the output beam current is proportional to  $\hat{S}(\vec{k}_\pm, \pm\omega - \omega_\Delta)$  so that the propagation direction of the fluctuations can be inferred by the frequency range of  $|\pm\omega - \omega_\Delta| > |\omega_\Delta|$  or  $|\pm\omega - \omega_\Delta| < |\omega_\Delta|$ . However, sensitive heterodyne measurements require extreme frequency stability of both oscillators since the signal appears as a sideband at the IF. The signals of interest for studies of turbulent density fluctuations are generally  $< 1$  MHz; however, these oscillators can drift by several or even tens of MHz even after warming up. Consequently, a feedback control system is needed to stabilize the frequency difference of the two sources. The superheterodyne receiver system configuration used on the PDX and TFTR tokamaks employed a feedforward tracking technique so that both source frequencies can drift slightly without changing the final carrier frequency.<sup>196</sup> In the heterodyne receiver of the FIR scattering system for DIII-D (Ref. 197), a phase lock frequency synchronizing system was used to control the LO source (a frequency-doubled klystron at 280.2 GHz) for eliminating the long-term drift and the FM source noise, combined with the feedforward tracking technique for preventing frequency pulling of the sources from degrading the heterodyne signal. In the homodyne detection scheme, the LO is unshifted in frequency with respect to the probe beam. In this

arrangement, the power spectrum of the output beat current is proportional to  $\hat{S}(\vec{k}_{\pm}, \omega)$  so that the propagation direction cannot be determined without a second mixer. A dual homodyne detection method, referred to as “homodyne spectroscopy,”<sup>198–200</sup> which employs two mixers with the LO phase shifted relative to one another by  $\phi = \pi/2$ , can be utilized to provide information concerning wave propagation direction.

#### VI.A.2. Representative Collective Scattering Systems

The first detailed measurements of turbulent density fluctuations in the interior of tokamaks using the CTS method were carried out by Mazzucato<sup>201–204</sup> and by Surko and Slusher<sup>205</sup> on the ATC and PLT tokamaks. Since then, microwave or laser CTS techniques have been used to study the turbulent density fluctuations in numerous tokamaks as well as other magnetically confined plasma devices. Scattering experiments have yielded the most significant contributions to the understanding of the turbulent mechanisms driving anomalous transport in magnetic confinement devices. There have been several excellent review papers on microwave or laser collective scattering experiments.<sup>11,206–212</sup> The interested reader is referred to the review papers and cited references. Here, we briefly describe some typical systems and their major results.

The TEXT multichannel scattering system,<sup>208</sup> using the configuration shown in Fig. 24, could scan the scattering volume vertically and horizontally and permitted the mapping of the microturbulence distribution over essentially the entire poloidal cross section as shown in Fig. 25. The apparatus simultaneously collected the scattered radiation at six angles corresponding to  $0 \leq k \leq 15 \text{ cm}^{-1}$ . A twin frequency FIR laser source ( $P_i \approx 14 \text{ mW}$ ,  $\lambda_i = 1222 \mu\text{m}$ , with the frequency difference of two sources  $\omega_{\Delta}/2\pi \approx 1 \text{ MHz}$ ) and a heterodyne detection system permitted resolution of the wave propagation direction. Using this apparatus, a variety of physical phenomena has been observed including a strong up-down asymmetry in fluctuation amplitude,<sup>213</sup> a quasi-coherent mode ( $\Delta\omega/\omega \leq 0.2$ ,  $\Delta k_{\perp}/k_{\perp} \approx 0.7$ ) in the inner equator,<sup>214,215</sup> experimental evidence for ion pressure gradient driven turbulence or  $\eta_i$ -modes,<sup>216,217</sup> experimental evidence for coupling of plasma particle and heat transport,<sup>218</sup> observation of confinement degradation and enhanced microturbulence as long-time precursors to high-density-limit disruptions,<sup>219</sup> and the effect of tearing modes on the spectrum and magnitude of microturbulence and experimental evidence for electron drift turbulence.<sup>220,221</sup>

The multichannel FIR scattering system on the DIII-D tokamak<sup>197,222</sup> utilized a special radial geometry to overcome the problem of poor access to the plasma. The radiation from the probe beam source is reflected from a carbon tile on the machine inner wall. A carcinotron source operating at 290 GHz with output power of 300 mW is

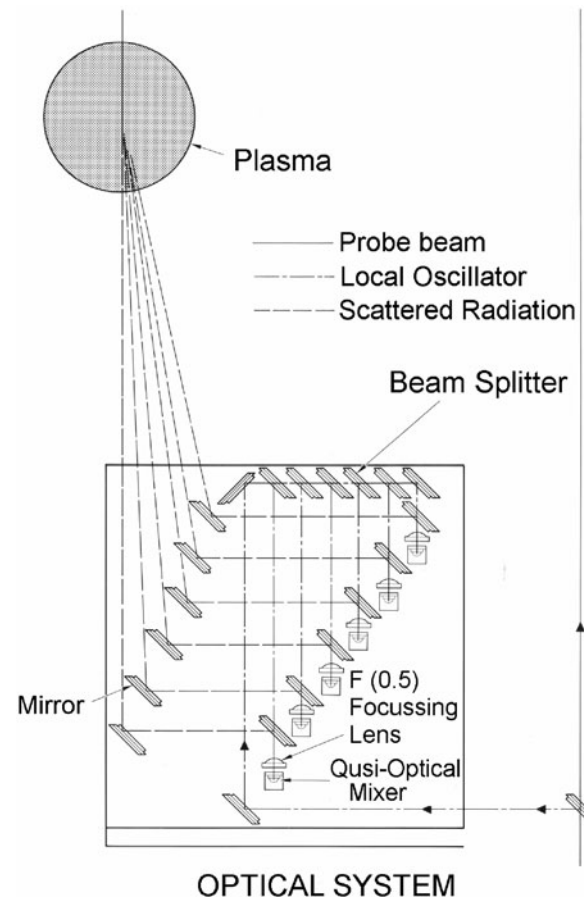


Fig. 24. Arrangement for multichannel FIR collective scattering apparatus on the TEXT tokamak. (From Brower et al., 1988)

employed as the probe beam source. Heterodyne detection is provided using a frequency-doubled klystron as the LO source, with the differential frequency jitter compensated by the employment of feedforward tracking techniques. Three receiver channels are available to study the  $k_{\theta}$  spectra of fluctuations in the range of  $k_{\theta} \approx 2$  to  $16 \text{ cm}^{-1}$  ( $0.2 \leq k_{\theta} \rho_s \leq 2.0$ ). The system was successfully applied to demonstrate the sheared flow suppression of turbulence at the L-H transition.<sup>191,192</sup> Recently, the FIR scattering system has been upgraded to probe low- $k$  ( $0$  to  $2 \text{ cm}^{-1}$ ) and intermediate- $k$  ( $8$  to  $15 \text{ cm}^{-1}$ ) fluctuations, and a high- $k$  ( $\sim 35 \text{ cm}^{-1}$ ) backscattering system has been added to address anomalous electron and ion transport.<sup>223</sup> The backscattering system employs a high-power (200-mW) solid-state source operating in X-mode at 94 GHz as the probe beam. The backscattering observes principally the radial wave number because of the 180-deg backscattering geometry. The  $2f_{ce}$  resonance in the incident radiation path acts as an internal “beam dump” absorbing both the incident and forward scattered radiation from low- $k$  turbulence. The location of this beam

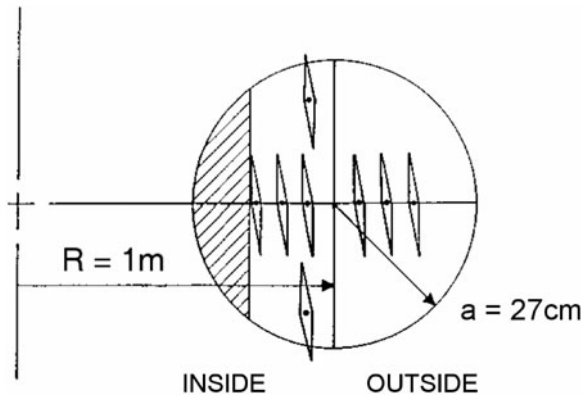


Fig. 25. Schematic of TEXT plasma cross section and scattering volumes for  $k_{\perp} = 12 \text{ cm}^{-1}$ . The shaded region is inaccessible because of port constraints. (From Brower et al., 1987)

dump can be varied by changing the toroidal magnetic field strength.

As a final example, the spatially scanning microwave scattering system, operating in the X-mode at 60 GHz, on the TFTR tokamak<sup>182,224</sup> is shown in Fig. 26. A Gunn source at 59.7 GHz is utilized as the LO for heterodyne measurements in the wave number range  $2.0 \leq k \leq 25 \text{ cm}^{-1}$ , with stabilization of the differential

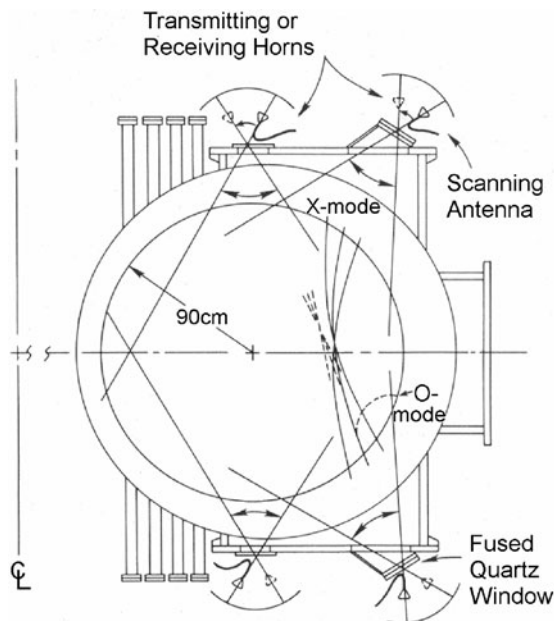


Fig. 26. TFTR plasma cross section showing the physical position of the X-mode scattering antenna and their scanning range. Each of the four scanning antennas consists of a Pyrex mirror and a microwave horn that pivots about the window. The scanning range of each antenna is  $\pm 30 \text{ deg}$ . (From Bretz et al., 1988)

frequency accomplished using the feedforward tracking technique.<sup>196</sup> The system was successfully applied to measure short-wavelength fluctuations with  $k \sim \omega_{pe}/c$  in enhanced reversed shear plasmas.<sup>225</sup>

### VI.B. Far Forward Scattering

In the preceding discussion, it was tacitly assumed that the scattering angle is larger than the divergence angle of the probe beam. Thus, the maximum measurable wavelength  $\lambda_{\text{max}}$  of fluctuations is limited by  $\lambda_{\text{max}} = \pi w_i/2$  via the criterion for minimum scattering angle  $\theta_{s,\text{min}} = 2\theta_d$ . Efforts to measure density fluctuations for all range of wave numbers have pushed scattering systems beyond this limit. There are three primary methods proposed for detecting long-wavelength fluctuations: far forward scattering, phase scintillation imaging, and phase contrast imaging. They all are based on the fact that an electromagnetic wave traversing the refractive plasma medium undergoes phase and amplitude modifications that are related to the wavelength, frequency, amplitude, and position of phase fluctuations in the medium. They differ only by how and where the desired information contained in the diffracted wave fronts is extracted.

The far forward scattering technique<sup>226</sup> detects modifications of the probe beam induced by density fluctuations in the far field. The scattering geometry is illustrated in Fig. 27. The Gaussian probe beam propagating in the z-direction is diffracted by the plasma wave (propagating transverse to the beam in the x-direction), which acts as a moving sinusoidal phase grating  $\phi(x) = \tilde{\phi}_0 \sin(kx - \Omega t)$ . As a result of passing through the wave, the beam acquires intensity components at the wave frequency and its harmonics. The component at the wave frequency, i.e., the first-order diffracted beam, corresponds to the IF signal from the heterodyne detector. Its intensity distribution in the front focal plane is given by

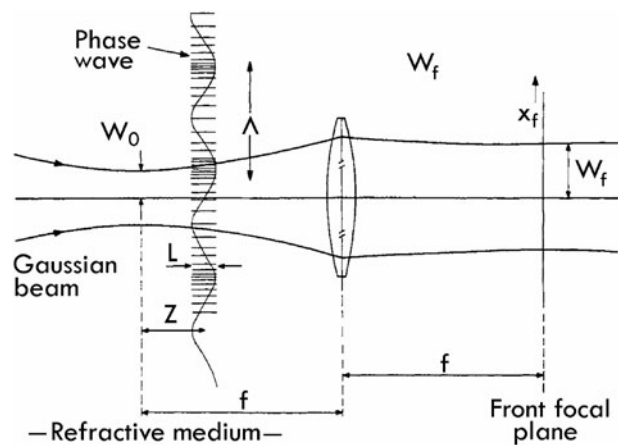


Fig. 27. Schematic of arrangement for far forward scattering. (From Evans et al., 1982)



$$I_1(u) = \frac{I_0}{\sqrt{\pi w_i}} \times \{ \tilde{\phi}_0 e^{-v^2/4} [e^{-A_-^2} \cos(\zeta v A_- - \Omega t) - e^{-A_+^2} \cos(\zeta v A_+ - \Omega t)] \} ,$$

where the dimensionless parameters are defined as follows:  $u \equiv x_f/w_f$ ,  $v \equiv kw_0$ ,  $A_{\pm} \equiv u \pm v/2$ ,  $\tilde{\phi}_0 \equiv r_e \lambda_i L \tilde{n}_0$ , and  $\zeta \equiv z/z_r$  ( $z_r$  is the Rayleigh length with the beam waist radius  $w_0$ ). This intensity distribution can be interpreted as the result of the two scattering terms  $\tilde{\phi}_0^2 e^{-(u-v)^2/4}$  and  $\tilde{\phi}_0^2 e^{-(u+v)^2/4}$  beating with the unperturbed term  $e^{-u^2}$ , which plays the role of an LO. This implies that the scattering occurs in the Raman-Nath regime; i.e., the inequality  $Lk^2/k_i \ll 1$  is satisfied.<sup>227</sup> Because of its time-dependent feature, the  $I_1(u)$  term can be easily distinguished from the unperturbed term under experimental conditions. The wave number of the fluctuations can be deduced from the envelope profile of  $I_1(u)$ . This technique has been used to measure long-wavelength turbulence on the TOSCA tokamak<sup>228</sup> and the TEXTOR tokamak<sup>229</sup> and the RFC-XX-M mirror machine.<sup>230</sup> This method has several attractive features. It is insensitive to vibrations and has experimental simplicity. However, it is quite sensitive to any minute departure from the assumed Gaussian beam profile. The technique is particularly useful for measuring long-wavelength coherent waves, which are difficult to resolve with conventional scattering systems, and is also suitable for long-wavelength microturbulence measurements. In addition to wave dispersion, this technique has been successfully employed to measure wave damping in laboratory experiments.<sup>231</sup>

A related technique to the far forward scattering technique is phase scintillation imaging, which is similar to that used in radio astronomy to measure interplanetary and interstellar fluctuations.<sup>232–234</sup> This technique differs from far forward scattering in that the measurements of phase fluctuations are made in the near field where the measured phase fluctuation spectrum bears a direct relation to that of the plasma density fluctuation. Since the phase modulation of the probe beam wave front is usually measured by using a two-path interferometer, the technique is inherently sensitive to airborne sound waves and mechanical vibrations. This technique is not fundamentally different from the far forward scattering because they both can be treated by a generalized theory of diffraction as discussed in the literature.<sup>235,236</sup> These techniques correspond, respectively, to the near-field and far-field detection of radiation diffracted by density fluctuations.

Phase contrast imaging<sup>237–239</sup> is also a near-field detection technique for measuring phase fluctuations of the probe beam wave front. Its difference from phase scintillation imaging derives from the fact that a phase con-

trast plate is employed to provide an internal phase reference. Thus, the technique requires only a single probe beam and has obvious advantages in its relative immunity to mechanical vibrations. Since the technique utilizes a phase plate, the maximum wavelength that can be discriminated against is less than the half-waist radius of the probe beam (see Chapter 4, “Laser-Aided Plasma Diagnostics,” by A. J. H. Donné, C. J. Barth, and H. Weisen, in this special issue of *Fusion Science and Technology*, for a detailed discussion of this technique).

### VI.C. Enhanced Scattering

The enhanced scattering approach, first described by Piliya,<sup>240</sup> Novik and Piliya,<sup>241</sup> Fidone,<sup>242</sup> and Fidone and Granata,<sup>243</sup> is a variant of conventional collective scattering. The technique is based on the scattering of an extraordinary electromagnetic wave (X-mode) from density fluctuations in the vicinity of the UHR defined by  $\omega_i^2 = \omega_{pe}^2(x_r) + \omega_{ce}^2(x_r)$ , where the inhomogeneity is assumed to be in the  $x$ -direction and  $x_r$  is the resonance position. In the backscattering case, which occurs if the Bragg condition  $q = 2k_i$  (where  $q$  is the wave number of fluctuations) is satisfied, this method is similar to reflectometry (see Sec. IV). Since the interaction of electromagnetic waves with density fluctuations occurs close to the resonance, the wave numbers of the incident and scattered waves increase rapidly up to values much larger than the vacuum wave number  $k_0 = \omega_i/c$  of the probing wave, i.e.,  $k_i(x) \gg k_0$ . This provides a way to detect small-scale fluctuations. The amplitudes of the incident and scattered waves increase together with the wave numbers with a scaling of  $\sim k_i^{3/2}$ , thus considerably enhancing the scattered power. Since this process occurs at a distance  $\Delta x = [2\omega_{ce}(x_r)/cq]^2 L \ll L$  (where  $L$  is the scale length of the inhomogeneity of the refraction index) from the resonance, the backscattering signal originates locally in the immediate vicinity of the resonance. Therefore, this technique is a suitable diagnostic for studying small-scale ( $q > 2\omega_i/c$ ) density fluctuations and waves in magnetically confined plasmas. When the technique is applied to a tokamak, the probe beam is launched from the high magnetic field side of the torus in the equatorial plane for accessibility, and radial wave numbers  $q_r > 2\omega_i/c$  are measured. The technique possesses the merits of high spatial resolution in the direction of the plasma inhomogeneity, enhanced scattering cross section, and experimental simplicity—a single antenna for launching and receiving waves. The method also permits measurement of the spatial distribution of density fluctuations by scanning the probing frequency or the magnetic field strength to displace the resonance position. However, the method has suffered from poor wave number resolution, due to the strong variation of the incident wave number near the UHR and a wide range of fluctuation wave numbers contributing to the backscattering signal.

During the last decade, several schemes have been developed to improve the wave number resolution of the enhanced scattering diagnostic. The time-of-flight technique for enhanced scattering<sup>244–247</sup> is based on the fact that the X-mode group velocity decreases as it approaches the UHR and the group delay time of the signal scattered from the UHR depends linearly on the fluctuation wave number  $q_r$  as

$$\tau_d = 2q_r \omega_i \left| \frac{\partial \omega_{pe}^2}{\partial r} + \frac{\partial \omega_{ce}^2}{\partial r} \right|_{\text{UHR}}^{-1} + \tau_0, \quad (62)$$

where  $\tau_0$  is the time delay due to propagation in waveguides and plasma far from the UHR. Thus, the group delay time is simply proportional to the radial wave number, and the temporal evolution of the scattered signal can be used to determine the  $q_r$  spectrum of turbulence. The turbulence can be measured by a sequence of short microwave pulses with duration  $\tau_p$  and repetition time  $T_p$  when the inequality  $\omega_i^{-1} \ll \tau_p \ll \tau_d \ll T_p$  is satisfied. This technique has been successfully applied to study small-scale turbulence on the FT-1 tokamak.<sup>248,249</sup> Figure 28 shows the UHR radar scattering system on the FT-1 tokamak. The 20-W X-mode probe beam operating at 28.05 GHz is launched into the plasma from the high magnetic field side of the torus. The probe beam amplitude is modulated with a half-power width of 5 ns and a

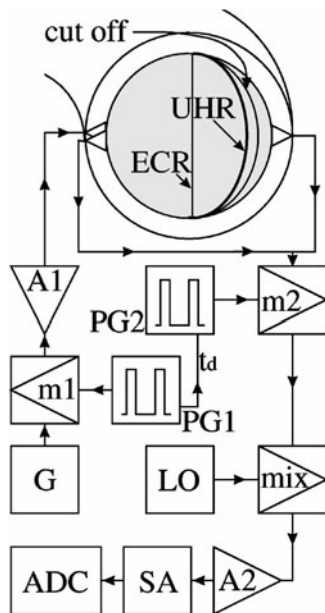


Fig. 28. Schematic of the UHR Radar scattering system on the FT-1 tokamak. Here, the components are G, 28-GHz generator; m1 and m2, modulators; PG1 and PG2, pulse generators; A1, microwave amplifier; LO, local oscillator; mix, microwave mixer; A2, rf amplifier; SA, spectrum analyzer; ADC, data acquisition. (From Bulyginitskiy et al., 2001)

repetition time of 70 ns. The gate technique is used for measuring the time delay of the backscattering signal. The fluctuation spectra are measured for different delay times of the backscattering signal. It is observed that the frequency spectra broaden substantially and the width of the spectra increase with the delay time and thus the fluctuation wave number. As suggested by the results of simulations and experiments, this behavior of the spectra may stem from the effect of multiple small angle scattering of both the incident and scattered beams by large-scale density fluctuations along their paths.<sup>157,249</sup> However, the technique has a drawback in that the signal-to-noise ratio is small in comparison with that of the stationary enhanced scattering technique.

The cross-correlation enhanced scattering scheme<sup>250,251</sup> is based on the fact that the phase of the enhanced scattering signal is determined by the fluctuation phase in the UHR as given by  $\Phi_s \approx qx_r(\omega_i)$  based on the WKB estimate. This technique measures the phase difference between two enhanced scattering signals, which are different in probing frequency and thus emanate from different resonance positions, by using the cross-correlation technique. The fluctuation wave number can be deduced from the cross phase, as given by

$$q = \frac{\Delta\Phi_s}{\Delta x_r} \approx \frac{\Delta\Phi_s}{(\omega_1 - \omega_2)\partial x_r / \partial \omega}. \quad (63)$$

Assuming the density fluctuations to be statistically stationary and homogeneous, the frequency and wave number spectra of fluctuations can be reconstructed by correlation techniques. This technique has been applied to investigate turbulent density fluctuations in laboratory plasmas with cylindrical and tokamak-like geometries<sup>251,252</sup> as well as the FT-1 tokamak.<sup>253</sup> The experimental results demonstrate that the technique is suitable for diagnosing small-scale turbulence with a reasonable wave number resolution.

The interferometer enhanced scattering scheme<sup>250</sup> is also based on the dependence of the enhanced scattering signals on the phase of fluctuations in the UHR position. The technique is suitable for the measurement of coherent waves launched into plasmas. In the case of coherent density fluctuations, the enhanced scattering signal amplitude is a periodic function of the incident frequency. By measuring its period using the interferometer enhanced scattering technique, the fluctuation wave number can be estimated. The technique has been employed to study the propagation of lower hybrid waves.<sup>254–256</sup> Both the wave number spectrum and the spatial distribution of density fluctuations are in reasonable agreement with those measured locally by the radio-frequency (rf) probe.

#### VI.D. Cross-Polarization Scattering

A technique called cross-polarization scattering<sup>184,257–262</sup> (CPS) has been proposed for diagnosing

magnetic fluctuations in magnetically confined plasmas. The technique relies on the fact that the vectorial magnetic fluctuations can induce cross-polarization (mode) scattering, that is, scattering of X-mode waves to O-mode waves and vice versa, while the scalar density fluctuations cannot. The scattering by magnetic fluctuations can be significant only when the incident frequency is near the electron cyclotron frequency, i.e.,  $\omega_i \sim \omega_{ce}$ . In conventional collective scattering, the magnetic fluctuation effect on wave scattering can normally be neglected since the incident frequency is sufficiently high,  $\omega_i \gg \omega_{pe}, \omega_{ce}$ , so that the effect of the plasma dielectric property on the wave propagation is negligible. CPS is performed in the plane perpendicular to the magnetic field  $\vec{B}$ . In this case, the O-mode is linearly polarized along the field, while the X-mode is elliptically polarized perpendicular to the field. Only the perpendicular components of magnetic fluctuations  $\vec{B}_\perp$  can induce CPS, so that the scattering from density and magnetic fluctuations can be distinguished by their polarizations. Since in magnetically confined plasmas the expected magnetic fluctuation level is several orders of magnitude less than that of density fluctuations, the wave cutoff or resonant effect should be exploited as a “polarization filter” to reject the signal scattered by density fluctuation from the total scattered signal.

The first experiment using the technique to measure internal magnetic turbulence was implemented on the Tore Supra tokamak.<sup>263,264</sup> Figure 29 shows the experimental arrangement. An X-mode wave from an extended interaction oscillator (EIO) source operating at 60 GHz with a power level of 70 W is launched vertically with its cutoff layer located within the plasma. The X-mode cutoff layer is used as a polarization filter to reflect the incident X-mode wave and the X-mode wave scattered by  $\vec{n}$ . Any X-mode wave mode converted to O-mode

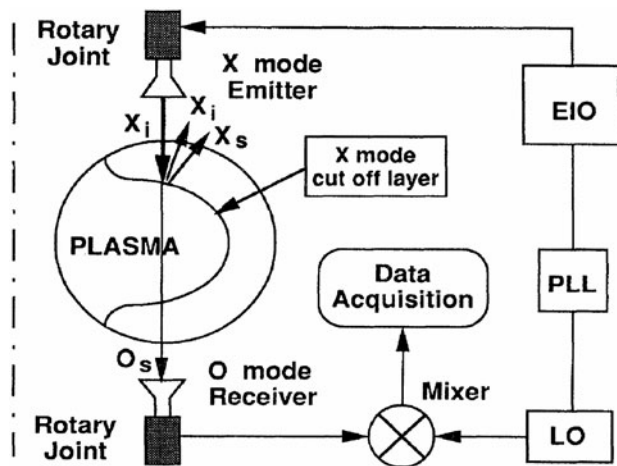


Fig. 29. Schematic of the CPS apparatus on the Tore Supra tokamak. (From Zou et al., 1995)

wave via scattering from magnetic turbulence then continues to propagate through the plasma and is detected by the receiver antenna positioned at the bottom of the torus. In order to optimize the polarization selection, high mode purity is required for both the transmitter and receiver antennas. This is achieved by an accurate positioning system with a motorized rotary joint that allows the antenna electric field direction matching to the direction parallel or perpendicular to the total magnetic field at the plasma edge with a precision of 0.36 deg. In this configuration, the radial wave numbers of magnetic fluctuations are primarily measured. Since the incident wave is strongly enhanced in the vicinity of the cutoff layer, this effect provides some spatial localization in the vicinity of the cutoff layer for the CPS signal. Figure 30 shows a typical turbulence spectrum obtained with the CPS configuration. It is observed that the spectrum of magnetic turbulence is significantly broader than that of density fluctuations and possesses no coherent features and that the fluctuation levels increase with the heating power and the poloidal beta number  $\beta_p$  in the L-mode confinement regime. This CPS technique has also been employed on the Gamma-10 mirror device to measure magnetic fluctuations.<sup>265</sup> However, the technique still suffers from some drawbacks including poor wave number resolution.

Recently, an alternative variant of the CPS diagnostic based on the mode conversion scattering effect in the vicinity of the UHR has been proposed.<sup>157,266,267</sup> In this scheme, the X-mode wave is launched from the HFS in the equatorial plane. The wave traverses the ECR region with slight damping and reaches the UHR position. In the vicinity of the UHR, the wave number and electric field

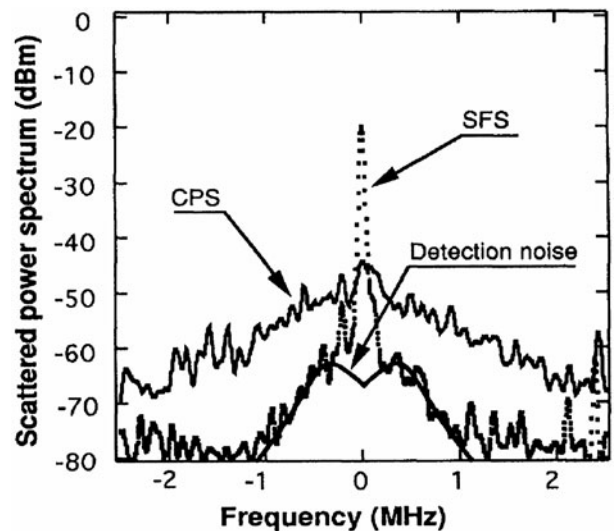


Fig. 30. Frequency power spectra of fluctuations obtained from the CPS and standard forward scattering (SFS). (From Zou et al., 1995)

of the incident X-mode wave increase strongly, and enhanced CPS by the small-scale magnetic fluctuations with a range of radial wave numbers,  $\omega_{ce}/c < q_r \leq \rho_{ce}^{-1}$ , can occur. The scattered O-mode radiation is received from the LFS in the equatorial plane. Here, the opaque region with a width of several vacuum wavelengths of the probe wave in the vicinity of the UHR is exploited as a polarization filter to reject the X-mode radiation. The radar technique can be used to make measurements with reasonable wave number resolution. The ECR layer can be used to absorb the parasitic radiation from the probe beam due to the transmitter antenna mismatch and its scattered wave by density fluctuations. The technique has been utilized on the FT-1 tokamak to demonstrate the capability of the technique for measuring small-scale magnetic fluctuations.<sup>248,267,268</sup>

## VII. APPLICATION OF COLLECTIVE SCATTERING TO THE DIAGNOSIS OF ION VELOCITY DISTRIBUTIONS THROUGH MEASUREMENTS OF MICROSCOPIC FLUCTUATIONS

### VII.A. Introduction

As noted in Sec. V, millimeter-waves and waves at higher frequencies scatter off fluctuations in the electron distribution and fluctuations in fields, while scattering off fluctuations in the ion distributions is negligible. The ions do, however, affect, and in some ranges dominate, the nature of the fluctuations in the electron population and in the fields. This is the reason why inference can be made about the ions from scattering measurements although the scattering is not directly off the ions.

When a charged particle, ion or electron, moves through the plasma, it pushes and pulls on the other charged particles in the plasma, which move to set up a shielding cloud around the particle. The extent of the cloud is approximately a Debye length,  $\lambda_D = \sqrt{T_e \epsilon_0 / n_e / q_e}$ . When the particle—call it the test particle to single it out—moves slowly, the cloud consists of both ions and electrons. When it moves faster, the electrons increasingly dominate the shielding because with their smaller mass, they respond more rapidly to changing fields. In addition to the shielding cloud, which can be described with good accuracy considering only electrostatic fields, the moving charge also excites waves in the plasma with which it has resonant interaction, that is, where  $v \cdot k = \omega$ . Here,  $v$  is the test particle velocity. Some of these waves are only properly described with a full electromagnetic description and, likewise, their interaction with the particle. The fluctuations in a plasma that a moving charge sets up can be likened to the perturbations a swan makes on the surface of a lake: Its feather plume makes a depression in the water that we can liken to the shielding cloud, and waves extend in its wake

when the swan moves—waves with which it is in resonant interaction.

Although an electron and a singly charged ion, moving with identical velocities, make identical perturbations to the electron distribution, only with opposite signs, there is an important difference; the test electron itself contributes to the perturbation in the electron distribution, while the test ion does not. When the particles are sufficiently fast, the shielding cloud consists mainly of electrons. The cloud is actually an increased average presence or absence of electrons within a Debye sphere from the test particle, essentially an electron or electron hole with a spatial extent of a Debye length. In the case of the test particle being an electron, we thus superimpose an electron hole with an extent of a Debye length on an actual electron. Viewed on a scale larger than the Debye length, the two coalesce, leaving little perturbation in the electron distribution. On this scale, the perturbations to the electron distribution are dominantly due to the presence of ions. Scattering off fluctuations on this scale is referred to as *collective* Thomson scattering and yields information about the ions. From this discussion, we might expect that ion driven fluctuations dominate over the electron-driven fluctuations if the Salpeter parameter<sup>269</sup>

$$\alpha = (\lambda_D k^\delta)^{-1} \quad (64)$$

is much greater than unity. The physical picture sketched here is essentially the content of the dressed particle approach used in several texts to derive expressions for the spectral power density of the microscopic fluctuations in a plasma.<sup>270–274</sup> For plasmas near thermal equilibrium, the fluctuation dissipation theorem can be used and yields identical results.<sup>184,275</sup> Here, we briefly describe an approach based on Klimontovich's microscopic distribution function.<sup>276</sup> This approach readily permits an electromagnetic formulation.<sup>274</sup>

### VII.B. Electromagnetic Model of Microscopic Fluctuations

The microscopic distribution function is given by

$$f^M(\mathbf{x}) = \sum_i \delta(\mathbf{x} - \mathbf{x}_i(t)) \quad , \quad \mathbf{x} = (\mathbf{r}, \mathbf{v}) \quad , \quad (65)$$

where  $\mathbf{x}_i(t)$  are the phase-space coordinates of the  $i$ 'th particle. The macroscopic distribution  $f$  and the microscopic fluctuations in the distribution  $\tilde{f}$  are given by

$$f = \langle f^M \rangle \quad , \quad \tilde{f} = f^M - f \quad . \quad (66)$$

Similar definitions hold for the microscopic and macroscopic fields. Neglecting collisions, the microscopic fluctuations satisfy the equation

$$\mathcal{L}\tilde{f} = -\tilde{\mathbf{a}} \cdot \partial_{\mathbf{v}} f^{(0)} \quad . \quad (67)$$

Integrating along unperturbed orbits (the characteristics of the operator  $\mathcal{L}$ ), we find the solution  $\tilde{f} = \tilde{f}^{(0)} + \tilde{f}^{(1)}$ , where  $\tilde{f}^{(0)}$ , the complementary function satisfying the homogeneous equation

$$\mathcal{L}\tilde{f}^{(0)} = 0, \quad (68)$$

represents the free streaming of noninteracting particles along unperturbed orbits, while

$$\tilde{f}^{(1)} = -\mathcal{L}^{-1}\{\tilde{\mathbf{a}} \cdot \partial_{\mathbf{v}} f^{(0)}\} \quad (69)$$

represents the dielectric response of the plasma to the microscopic fluctuating fields. The complementary function  $\tilde{f}^{(0)}$  is identical with the actual particle distribution at some early time minus the ensemble average. The particular integral  $\tilde{f}^{(1)}$  is zero at that time and evolves from there to account for the particle interactions ignored in  $\tilde{f}^{(0)}$ . For a more detailed discussion, see Refs. 173 and 174. Writing the current  $\tilde{\mathbf{j}}^{(1)} = q \int \mathbf{v} \tilde{f}^{(1)} d\mathbf{v}$  as the dielectric response to  $\tilde{\mathbf{E}}$ , associating  $\tilde{\mathbf{j}}^{(0)} = q \int \mathbf{v} \tilde{f}^{(0)} d\mathbf{v}$  with the current fluctuations of the free-streaming discrete particles, and inserting these expressions for currents in Maxwell's curl equations, we find

$$\mathbf{\Lambda} \tilde{\mathbf{E}} = \frac{-i}{\omega \epsilon_0} \sum_a \tilde{\mathbf{j}}^{(a0)}. \quad (70)$$

The sum is over charged-particle species (electrons and ions). The dielectric tensor,  $\boldsymbol{\epsilon} = \mathbf{I} + \sum_a \boldsymbol{\chi}^{(a)}$ , in the wave tensor  $\mathbf{\Lambda}$ , includes the susceptibilities of all charged-particle species  $a$ . Note that while the dielectric response of the ions typically could be ignored at the frequencies of the probe radiation  $i$  and the scattered radiation  $s$ , this is not the case at the generally lower frequencies of the resolved fluctuations  $\delta$ .

In the dressed particle picture,  $\tilde{f}^{(0)}$  represents the unscreened test particles, while  $\tilde{f}^{(1)}$  represents the screening clouds and waves in the wakes of the test particles. Solving for  $\tilde{\mathbf{E}}$  in Eq. (70) and making use of the relations

$$\begin{aligned} \omega \tilde{\mathbf{B}} &= \mathbf{k} \times \tilde{\mathbf{E}}, \\ \tilde{\mathbf{j}}^{(e)} &= \tilde{\mathbf{j}}^{(e0)} - i\omega \epsilon_0 \boldsymbol{\chi}^{(e)} \tilde{\mathbf{E}}, \\ \tilde{\Gamma} &= \tilde{\mathbf{j}}^{(e)}/q_e, \end{aligned}$$

and

$$\omega \tilde{n} = \mathbf{k} \cdot \tilde{\Gamma}, \quad (71)$$

we obtain the expressions for fluctuations in any of the four considered quantities,  $\tilde{n}$ ,  $\tilde{\Gamma}$ ,  $\tilde{\mathbf{B}}$ , and  $\tilde{\mathbf{E}}$ ,

$$\tilde{\alpha}_i = \hat{S}_{ik}^{(ai)} \sum_{a \neq e} \tilde{J}_k^{(a0)} + \hat{S}_{ik}^{(ei)} \tilde{J}_k^{(e0)}, \quad (72)$$

where we have introduced the fluctuation operators

$$\hat{S}_{ik}^{(E)} = \Lambda_{ik}^{-1} \frac{-i}{\omega \epsilon_0}, \quad (73)$$

$$\hat{S}_{ik}^{(B)} = \epsilon_{ijl} \frac{k_j}{\omega} \hat{S}_{lk}^{(E)}, \quad (74)$$

$$\hat{S}_{ik}^{(\Gamma i)} = -\chi_{ij}^{(e)} \Lambda_{jk}^{-1} \frac{1}{q_e}, \quad \hat{S}_{ik}^{(\Gamma e)} = \hat{S}_{ik}^{(\Gamma i)} + \delta_{ik}, \quad (75)$$

and

$$\hat{S}_k^{(na)} = \frac{k_i}{\omega} \hat{S}_{ik}^{(\Gamma a)}, \quad a = e, i. \quad (76)$$

The ensemble average of products of fluctuating quantities can now be written

$$\langle \alpha_i \beta_j \rangle = \sum_{a=e,i} \hat{S}_{ik}^{(aa)} \langle \tilde{J}_k^{(a0)} \tilde{J}_{k'}^{(a0)} \rangle \hat{S}_{jk'}^{(\beta a)*}. \quad (77)$$

Therefore, for instance, the spectral power density of the density fluctuations is given by

$$\langle nn \rangle = \hat{S}_k^{(ni)} \sum_{a=i} \langle \tilde{J}_k^{(a0)} \tilde{J}_{k'}^{(a0)} \rangle \hat{S}_{k'}^{(ni)*} + \hat{S}_k^{(ne)} \langle \tilde{J}_k^{(e0)} \tilde{J}_{k'}^{(e0)} \rangle \hat{S}_{k'}^{(ne)*}, \quad (78)$$

where the sum is over ion species.

The correlation tensor for the currents associated with the free streaming of test particles,

$$\langle \tilde{J}_k^{(a0)} \tilde{J}_{k'}^{(a0)} \rangle = q_a^2 \int v_k v_{k'} \langle \tilde{f}^{(a0)}(\mathbf{v}) \tilde{f}^{(a0)}(\mathbf{v}') \rangle d\mathbf{v} d\mathbf{v}', \quad (79)$$

can be expressed in terms of the macroscopic distribution function  $f^{(a0)}$ . We recall that  $\tilde{f}^{(a0)}$  was identical with the real particle distribution at some early time minus the ensemble average. In the real distribution, particle correlations exist because of the finite interaction between the particles. As the evolution of  $\tilde{f}^{(a0)}$  ignores particle interactions, these correlations are gradually lost. Let us assume that at time  $t'$  the correlations can be ignored. We can then find the one time correlation function

$$\begin{aligned} \langle \tilde{f}(\mathbf{x}, t') \tilde{f}(\mathbf{x}', t') \rangle &= \langle f^M(\mathbf{x}, t') f^M(\mathbf{x}', t') \rangle \\ &- f(\mathbf{x}, t') f(\mathbf{x}', t') \end{aligned} \quad (80)$$

by considering the one time ensemble average of the microscopic distribution, ignoring particle correlations,

$$\begin{aligned}
 & \langle f^M(\mathbf{x}, t') f^M(\mathbf{x}', t') \rangle \\
 &= \left\langle \sum_{i,j} \delta(\mathbf{x} - \mathbf{x}_i(t')) \delta(\mathbf{x}' - \mathbf{x}_j(t')) \right\rangle \\
 &= \left\langle \sum_{i=j} \delta(\mathbf{x} - \mathbf{x}_i(t')) \delta(\mathbf{x}' - \mathbf{x}_j(t')) \right\rangle \\
 &\quad + \left\langle \sum_i \delta(\mathbf{x} - \mathbf{x}_i(t')) \sum_{j \neq i} \delta(\mathbf{x}' - \mathbf{x}_j(t')) \right\rangle \\
 &= \delta(\mathbf{x} - \mathbf{x}') \left\langle \sum_i \delta(\mathbf{x} - \mathbf{x}_i(t')) \right\rangle \\
 &\quad + \sum_i \langle \delta(\mathbf{x} - \mathbf{x}_i(t')) \rangle \sum_{j \neq i} \langle \delta(\mathbf{x}' - \mathbf{x}_j(t')) \rangle \\
 &= \delta(\mathbf{x} - \mathbf{x}') f(\mathbf{x}, t') + \frac{N-1}{N} f(\mathbf{x}, t') f(\mathbf{x}', t') .
 \end{aligned} \tag{81}$$

In the final equality,  $N$  is the total number of particles. Ignoring the small difference between  $N$  and  $N-1$ , inserting Eq. (81) to Eq. (80), and ignoring any first-order perturbations to the equilibrium distribution, we have

$$\langle \tilde{f}(\mathbf{x}, t') \tilde{f}(\mathbf{x}', t') \rangle = \delta(\mathbf{x} - \mathbf{x}') f^{(0)}(\mathbf{x}, t') . \tag{82}$$

The spectral power density of the distribution fluctuation fluctuations, required in Eq. (79), is the spatial and temporal Fourier transform of the two-time correlation  $\langle \tilde{f}(\mathbf{x}, t) \tilde{f}(\mathbf{x}', t') \rangle$ , which we obtain by solving the differential equation

$$\mathcal{L}_{\mathbf{x}, t} \langle \tilde{f}(\mathbf{x}, t) \tilde{f}(\mathbf{x}', t') \rangle = 0 \tag{83}$$

with Eq. (82) as the initial condition. The differential operator in Eq. (83) acts on  $\mathbf{x}, t$ . This equation is obtained by multiplying Eq. (68) by  $\tilde{f}(\mathbf{x}', t')$  and taking the ensemble average. Integrating Eq. (83) and Fourier transforming, we find

$$\begin{aligned}
 \langle \tilde{f}_k^{(a0)} \tilde{f}_{k'}^{(a0)} \rangle &= (2\pi)^2 \frac{q_a^2}{|k_{\parallel}|} \int dv_{\perp} v_{\perp} \\
 &\quad \times \sum_{l=-\infty}^{\infty} c_{kl} c_{k'l}^* f^{(a0)}(v_{\perp}, v_{\parallel}) ,
 \end{aligned} \tag{84}$$

where

$$\mathbf{c}_l = \begin{Bmatrix} \frac{l\omega_{ca}}{k_{\infty}} J_l(k_{\perp} \rho) \\ -iv_{\perp} J_l'(k_{\perp} \rho) \\ v_{\parallel} J_l(k_{\perp} \rho) \end{Bmatrix}, \quad v_{\parallel} = \frac{\omega - l\omega_{ca}}{k_{\parallel}}, \tag{85}$$

where

$\parallel, \perp$  = components of vectors parallel and perpendicular to  $\mathbf{B}^{(0)}$ , respectively

$J_l$  = Bessel functions of the first kind

$\rho = v_{\perp} / \omega_{ca}$ .

In evaluating the spectral power densities of fluctuations, the main computational effort is associated with evaluating the correlation tensor for the currents associated with the free-streaming test particles and with the susceptibility tensors of the ions. These quantities are required irrespective of which of the four fluctuating quantities considered here are evaluated. The additional effort in including all four quantities in the evaluation as opposed to just one—the density fluctuations, for instance—is minor. In the analysis of fast ion CTS data from JET and current experiments at TEXTOR and ASDEX Upgrade,<sup>277–279</sup> and in making predictions for ITER (Refs. 280, 281, and 282), all quantities are retained in the computations.

### VII.C. Examples of CTS Spectra

An example of a spectrum of fluctuations where the ion-driven fluctuations, also called the ion features, dominate those driven by the electrons, the electron feature, is given in Fig. 31 showing the scattering function as a

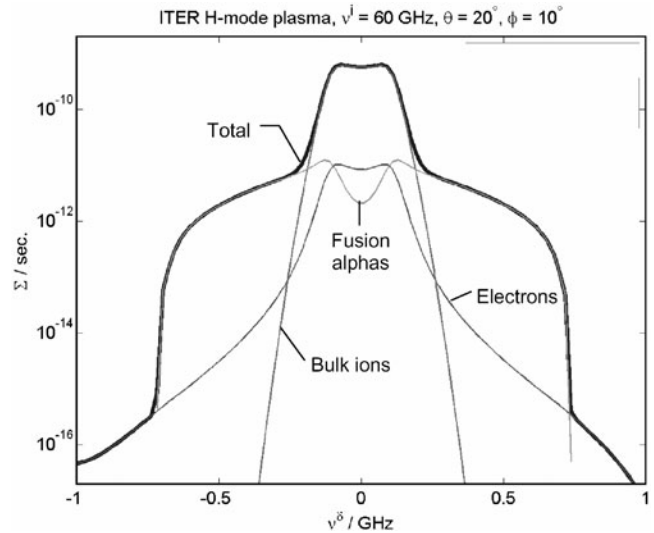


Fig. 31. Scattering function  $\Sigma$  as a function of fluctuation frequency,  $\nu^{\delta} = \nu^s - \nu^i$ , for a probe frequency of 60 GHz, a scattering geometry where  $\theta = \angle(\mathbf{k}^i, \mathbf{k}^s) = 20$  deg,  $\phi = \angle(\mathbf{k}^s - \mathbf{k}^i, \mathbf{B}^{(0)}) = 10$  deg,  $n_e = 10^{20} \text{ m}^{-3}$ ,  $B^{(0)} = 5.6 \text{ T}$ ,  $n_{\alpha} = 5 \times 10^{17} \text{ m}^{-3}$ , and the alpha particles have a classical slow-down distribution. The Salpeter parameter  $\alpha \approx 26$ .

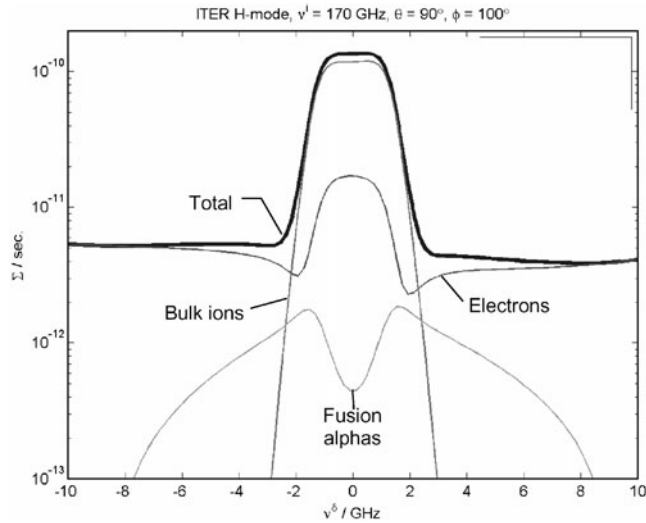


Fig. 32. Similar to Fig. 30, except that here the probe frequency is 170 GHz, the scattering angle  $\theta = 90$  deg, and the probing direction  $\phi = 100$  deg. The Salpeter parameter  $\alpha \approx 2$ .

function of fluctuation frequency for a CTS with a 60-GHz probe frequency, a scattering angle of  $\theta = \angle(\mathbf{k}^i, \mathbf{k}^s) = 20$  deg, a probing angle of  $\phi = \angle(\mathbf{k}^s - \mathbf{k}^i, \mathbf{B}^{(0)}) = 10$  deg, and ITER-relevant plasma parameters. We note that both the alpha-particle feature and the bulk ion feature clearly dominate the electron feature over the entire spectrum of frequencies where the ion features are present. On the basis of the consideration of the test electron coalescing with its shielding electron hole on scales larger than the Debye length, as discussed above, we would expect the ion features to dominate when the Salpeter parameter is much greater than unity. Here,  $\alpha \approx 26$ . The value of  $\alpha$  at which the ion features dominate of course depends on the ion density, but also on the probing direction  $\phi$ . A larger value of  $\alpha$  is required when probing is near perpendicular to the magnetic field. In Fig. 32, we show a case where the electron feature dominates the alpha feature. Here,  $\alpha \approx 2$ . The reduced Salpeter parameter is due to an increased probe frequency and increased scattering angle. The spectrum is also affected by the altered probe direction, here closer to perpendicular to the magnetic field. Generally, increased probe frequency must be compensated by reduced scattering angle to maintain dominant ion features. At the frequency of the CO<sub>2</sub> laser, the scattering angle for CTS generally needs to be  $< 0.5$  deg.

#### VII.D. Signal-to-Noise Ratio

Obtaining information on the ions from CTS also requires that the scattered signal can be distinguished from the noise background. The noise arises from the receiver electronics and from plasma emissions. In the millimeter-wave range, the latter is principally ECE. Typ-

ically, the spectral power densities of the CTS signals are much lower than those of the noise. Averaging the measured signals with noise over a finite bandwidth  $\nu_B$  and a finite time interval  $\tau$  and subtracting the noise estimated separately, e.g., in a period where the probe is off, the estimate of the signal divided by the standard deviation of the estimate of the signal is effectively the signal-to-noise ratio with which the CTS spectrum can be estimated. This postdetection signal-to-noise ratio is given by<sup>283,284</sup>

$$\frac{S}{N} = \frac{P_\nu^s}{P_\nu^s + N} \sqrt{\nu_{ch} \tau}, \quad (86)$$

where  $P_\nu^s = \partial P^s / \partial \nu^s = 2\pi \partial P^s / \partial \omega^s$  is the spectral power density of the CTS signal modeled by expression (41) in Sec. V.C and  $N$  is the spectral power density of the noise. With millimeter-wave CTS, the raw signal-to-noise ratio  $P_\nu^s / N$  can readily be 1/100, while typical channel bandwidths and integration times are 100 MHz and 10 ms, resulting in a typical postdetection signal-to-noise ratio of 10 in a typical channel.

#### VII.E. Choice of Probe Frequency

The availability of stable narrowband powerful sources of probing radiation, considerations of the signal-to-noise ratio and absorption of radiation in the plasma, and considerations of the limitations to the scattering geometry resulting from the need to distinguish the ion features from the electron feature determine the choice of probing frequency and scattering geometry. Such considerations did not enter into the first measurements of the ion temperature by CTS, which were done in radar back-scattering experiments in the ionosphere.<sup>285</sup> The narrow width of the measured spectrum, reflecting the ion thermal velocity rather than the expected electron thermal velocity, came as a surprise and sparked off the development of the theory of CTS. With the theoretical understanding in place, it became clear that in fusion plasmas the choice of probing frequency is a compromise.

The infrared CO<sub>2</sub> laser is a powerful source; however, the scattering angle has to be small leading to challenges from stray radiation entering the receiver and with spatial resolution. In the FIR, scattering angles can be in the more convenient range of 10 deg reducing both challenges found in the infrared range. However, in the FIR range the sources are weaker and more challenging to build and operate. The first measurements of the bulk ion temperature in a tokamak<sup>286</sup> were done with an optically pumped FIR D<sub>2</sub>O laser. With powerful millimeter-wave sources in the form of gyrotrons, CTS in the millimeter-wave range became a competitive option.<sup>287</sup> In the lower-frequency end of the millimeter-wave range, there are essentially no limitations on scattering geometry, the ion features always dominate, allowing the geometry to be selected to meet other objectives. In this frequency range,

the challenge is the relatively strong ECE raising the noise background. Certain millimeter-wave frequency ranges are not usable because of excessive ECE or indeed absorption of the probe and scattered radiation. For electron temperatures up to  $\sim 10$  keV in toroidal fusion plasmas with aspect ratios of 3 or more, CTS systems with the probe frequency between the fundamental- and the second-harmonic features of the ECE spectrum can be exploited.

The first fast ion measurements with CTS (Ref. 277) were done at JET with such a system. Subsequently, the temporal evolution of the fast ion population has been measured at TEXTOR with a similar system.<sup>279</sup> At higher electron temperatures, as expected in ITER, millimeter-waves can only be used for CTS at frequencies below the ECE spectrum.<sup>280</sup> Here, refraction is an additional challenge. For ITER, an operational window is predicted to exist at  $\sim 60$  GHz. This probe frequency has been found to be the most promising in a feasibility study covering millimeter-waves, FIR, and infrared.<sup>280</sup> As an interesting alternative to the CTS discussed thus far, a four-wave-mixing-based diagnostic technique for confined alpha-particle measurement has been proposed.<sup>289,290</sup> The technique involves the excitation of lower hybrid waves whose phase velocities can be “tuned” through the alpha-particle distribution. In this method, the beat wave attributes and parameters are selected such that the damping is caused primarily by the alpha particles. A four-wave-mixing or phase conjugation detection scheme is suggested to both generate and scatter off of the beat waves, thereby eliminating the need for a high-power long-pulse source since only submicrosecond-duration pulses from 100-kW level sources at  $\cong 100$  GHz are required.

## VII.F. Assessing the Information Content in CTS Data

In assessing the feasibility of a fast ion CTS system, and indeed to compare different designs for optimization, it is necessary to be able to predict what information can be inferred about the fast ions and to quantify this information.

### VII.F.1. The Global Signal-to-Noise Ratio

Consider a CTS spectrum resolved in  $N$  channels with  $l_i = (S/N)_i = E(P_i^i)/\sqrt{\text{var}(P_i^i, P_i^i)}$ , the signal-to-noise ratio in the  $i$ 'th channel or, as noted above, the ratio of the estimate of the signal in channel  $i$  to the square root of the variance of that estimate. If we split that channel in two, the signal-to-noise ratio in each new channel is  $l_i/\sqrt{2}$  assuming that the spectral power densities of signal and noise vary little over the channel. The sum of the signals in the two new channels carries the same information as the original channel. The difference between the signals in the two new channels carries a small additional amount of information.

Resolving a spectrum in more and narrower channels, each with a smaller signal-to-noise ratio, never leads to less information. It turns out that the quantity

$$L_N = \left( \sum_{i=1}^N l_i^2 \right)^{1/2} \quad (87)$$

tends asymptotically to a finite value  $L$  and in practice has essentially converged when the number of channels resolving the spectrum reasonably represent the shape of the spectrum.  $L$  thus defined is essentially a global signal-to-noise ratio for the spectrum and a measure of the amount of information in the spectrum. The noise considered here is really uncertainties (standard deviation) in the estimates of the signals in the channels. These uncertainties might actually be correlated in which case the signal-to-noise ratio of the average signal in two narrow neighboring channels is not improved by root two but by less. This reflects the fact that a complete description of the uncertainties in the estimates of the channel signal strengths is not given by the variances of the estimates of each channel but requires the complete covariance matrix for the estimates. A more general definition of the global signal-to-noise ratio is then definable as

$$L = \left( \sum_i \alpha_{ii} \right)^{1/2}, \quad (88)$$

where  $\alpha$  is the inverse of the normalized covariance

$$\alpha = \mathbf{C}^{-1}$$

and

$$C_{ij} = \frac{\text{var}(P_i^i, P_j^i)}{P_i^i P_j^i}. \quad (89)$$

Equation (88) reduces to Eq. (87) if the uncertainties in the estimates of channel signal strengths are independent.

### VII.F.2. Nuisance Parameters and Parameters of Interest

To focus on the information on fast ions, we could evaluate the global signal-to-noise ratio using only the fast ion feature in the spectrum. However, the information that can be inferred about the ion distribution depends not only on the spectral signal-to-noise ratio but also on the uncertainties in any additional information used. The CTS spectra depend on the fast ion distribution function and on a number of other plasma parameters, e.g., electron temperature, and system parameters, e.g., scattering angle. These nuisance parameters, the determination of which we assume not to be the objective of the CTS measurement, need to be estimated to extract information about the parameters of interest,



the parameters characterizing the ion distributions. If we have no prior information about the nuisance parameters, we can of course seek to estimate them from the CTS spectra, but this reduces the amount of information available for inference about the ion distributions. Prior information about the nuisance parameters, e.g., ECE measurements of the electron temperature, increases the ion information that can be extracted. Uncertainties in prior information about nuisance parameters as well as the spectral noise limit the accuracy and detail with which inference can be made about the ion distributions. Assuming optimal inference<sup>288</sup> and taking spectral noise and uncertainties in prior information into account, the uncertainties in the estimates of the ion distributions can be estimated. Here, we note that although the scattering function formally depends on the full 3-D velocity distribution, the sensitivity to variations in the distribution function in the velocity directions orthogonal to  $k^\delta$  is virtually nil, so we can conclude that in practice CTS resolves the 1-D velocity distribution in the direction of  $k^\delta$ . Our model function of the fast ions for inference from CTS thus needs only be a 1-D function. A convenient model function is a trapezoidal curve through a finite set of nodes at fixed velocities but variable heights, or rather variable phase-space densities. For numerical convenience, we round the trapezoidal curve at its bends.

### VII.F.3. Features in the Velocity Distribution That Can Be Resolved

Increasing the number of nodes with which we resolve the distribution function also increases the uncertainty in the inference about each node. The number of nodes must be less than the number of channels, and for design studies it is preferable to allow the number of channels to be sufficiently large not to affect the results. The uncertainties in the inferred nodes are generally correlated, so the covariance tensor

$$C_{ij} = \text{var}(f_i, f_j) \quad (90)$$

gives a more complete picture of the uncertainties than the variances of each node alone. Here,  $f_i$  is the phase-space density at the  $i$ 'th node. The covariance contains much more detailed information on what is resolved than can be conveyed simply with error bars on each node. If, for instance, there is a common uncertain scaling factor for all the nodes so that the absolute value of the distribution is uncertain but the relative shape is well resolved, then the error bars would all be large and not reveal that the relative shape is well resolved. This information is readily extracted from the covariance matrix by considering its eigenvectors and eigenvalues. This is, in fact, a principal component analysis of the uncertainty distribution of the inferred nodes.

### VII.F.4. The Resolving Power, A Measure of Information

As with the global signal-to-noise ratio for the spectra, we can define a global dimensionless measure of the information available on the fast ion distribution. We call it the resolving power  $L$  and define it as in Eq. (88), now for the inverse of the covariance of the inferred distribution nodes given in Eq. (90), but with the node densities  $f_i$  normalized by a target accuracy  $\Delta$ . For a sufficient number of nodes, the value of  $L$  is not changed significantly by increasing the number of nodes. If the uncertainties in the nodes are uncorrelated, then  $L^2$  is the number of nodes that can be resolved with an uncertainty of  $\Delta$ . With more nodes, the uncertainty would be greater in each node. If, in addition, all uncertainties in nodes were equal, then the uncertainty in the mean of all the nodes would be  $\Delta/L$ .

### VII.F.5. Practical Examples

The principal component analysis and the information measure given by the resolving power are useful tools in comparing different CTS systems and were used extensively in a recent study of the feasibility of measuring fast ions in ITER using CTS (Refs. 280 and 291). A sample model fusion alpha-particle distribution function from this study is given in Fig. 33. The model is resolved in 28 nodes. The outermost are not plotted here. The error bars indicate the uncertainties in the node estimates: the smaller ones when only spectral uncertainties are

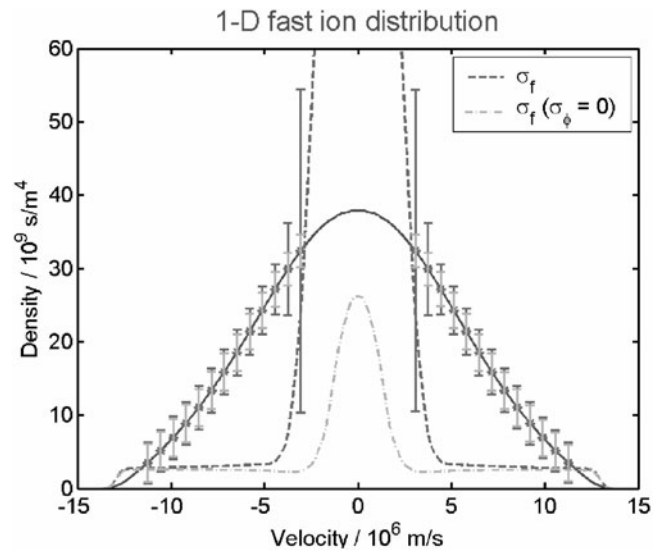


Fig. 33. Model fusion alpha-particle distribution function for ITER, showing nodes of the model function and the uncertainties in the inferences about the nodes assuming a 60-GHz CTS system.

accounted for while the larger also account for uncertainties in prior information about the nuisance parameters. For a target accuracy  $\Delta = 6 \times 10^9$  s/m<sup>4</sup>, which is the minimum accuracy in resolved nodes we were seeking for the diagnostics, the resolving power is  $L = 13$ , implying that more than 100 nodes could be resolved with an uncertainty less than the target accuracy. This is for a CTS using a 60-GHz probe frequency, a probe power of 1 MW, an integration time of 20 ms, a scattering angle of 25 deg, and a resolved direction near parallel to the magnetic field. The beams assume an LFS midplane launch of the probe and an HFS receiver viewing the plasma through a 3-cm-high, 20-cm-wide slot on the HFS. The study suggests that CTS combined with a backscattering system with probe and receiver antennas on the LFS midplane can meet the ITER measurement requirements for fusion alpha particles.

## VIII. FAST WAVE INTERFEROMETRY AND REFLECTOMETRY

### VIII.A. Introduction/Review

Classical interferometry and reflectometry employ waves near or above the plasma frequency or the electron cyclotron frequency, both depending on the electron properties, and can lead to the determination of the electron density or (less usual) the magnetic field. In the case of interferometry or reflectometry using Alfvén waves or waves in the ion cyclotron range, the propagation properties depend not only on magnetic field and ion density but also on the ion charge and mass. Phase delay measurements in that range will therefore be a way to obtain information on those quantities, ion mass being of particular interest.

Fast Alfvén wave interferometry<sup>292–294</sup> uses waves launched perpendicular to the magnetic field, with frequencies above the ion cyclotron frequency ( $\Omega_{ci}$ ) but below the ion plasma frequency ( $\omega_{pi}$ ), the electron plasma frequency ( $\omega_{pe}$ ), and the electron cyclotron frequency ( $\omega_{ce}$ ). In this range, the wave propagates at the Alfvén velocity:

$$V_a = B/(\mu_0 M_i n)^{1/2} ,$$

where

$B$  = magnetic field

$\mu_0$  = permeability constant

$M_i$  = ion mass

$n$  = ion density.

In a simplified scenario of a homogeneous plasma, if we measure the phase delay  $\phi$  across the plasma, we could

derive the density since  $\phi = 2\pi fl/V_a$ , where  $f$  is the wave frequency and  $l$  is the path length. In order to avoid the  $2\pi$  phase ambiguity, one could sweep  $f$ , determine  $d\phi/df$ , and thus obtain the density information. This measurement would, in principle, be less sensitive to vibrations than traditional interferometry; on the other hand, the spatial resolution will be worse, and the ray trajectory needs to be calculated.

This technique considers a single-species plasma. One step forward is to attempt the determination of the mass density of each species in a two-species plasma, as would be the case in deuterium-tritium (D-T) burning plasmas. For this measurement, one of the possibilities is to reflect waves in the “ion-ion hybrid resonance.”<sup>293,295,296</sup>

In the cold plasma approximation, the index of refraction of a wave propagating perpendicular to the magnetic field is given by<sup>3,295</sup>

$$n = \sqrt{R \cdot L/S} , \quad (91)$$

where

$$R = 1 - \sum_s \frac{\omega_{ps}^2}{\omega \cdot (\omega + \Omega_{cs})} , \quad (92)$$

$$L = 1 - \sum_s \frac{\omega_{ps}^2}{\omega \cdot (\omega - \Omega_{cs})} , \quad (93)$$

$$S = \frac{1}{2}(R + L) , \quad (94)$$

and  $s$  refers to the different species.

At  $L = 0$  or  $R = 0$ , we have cutoffs, whereas for  $S = 0$  we have the resonance.

For two ion species, the ion-ion hybrid cutoff occurs at  $L = 0$  and

$$\omega_{cutoff} \approx \Omega_1 f_2 + \Omega_2 f_1 , \quad (95)$$

where

$$\Omega_1 = Z_1 eB/m_1$$

$$\Omega_2 = Z_2 eB/m_2 \text{ (ion cyclotron frequencies for both species)}$$

$$f_1 = q_1 n_1/n_e$$

$$f_2 = q_2 n_2/n_e.$$

In the case of a hydrogen-deuterium plasma, Eq. (94) becomes

$$\omega_{cutoff} \approx \Omega_H(1 - \frac{1}{2} f_H) , \quad (96)$$

where  $f_H$  is the hydrogen fraction.

As in the case of microwave reflectometry, the existence of resonances could limit the access either from the LFS or from the HFS. The relevant resonances would be the ion cyclotron frequencies and the ion-ion hybrid resonance, which for a two ion species is given by

$$\frac{\omega_{p1}^2}{(\omega^2 - \Omega_1^2)} + \frac{\omega_{p2}^2}{(\omega^2 - \Omega_2^2)} \approx 0. \quad (97)$$

For a hydrogen-deuterium (H-D) plasma,

$$\omega_{resonance} = \Omega_H \sqrt{\frac{1 - f_H/2}{1 + f_H}}. \quad (98)$$

This resonance is slightly below the cutoff. A radial profile of the relevant frequencies for H-D in the DIII-D tokamak is shown in Fig. 34. We see also the familiar effect of shadow areas due to the absorption at cyclotron frequencies.

The determination of the cutoff profile (and therefore the profile of  $f_H$ ) can be performed by techniques similar to those used in microwave reflectometry: WKB approach (which can be refined with more sophisticated ray-tracing codes), frequency sweep, and numerical inversion. This works well for LFS launching but needs further analysis for HFS launching. The wave reaches first the resonance and should be damped, but the vicinity of the cutoff allows for some transparency, and a fraction of the wave could be reflected and received at the antenna. The formalism could be extended easily to additional species.<sup>295</sup> One important detail to take into account is that He nuclei as well as any fully stripped impurity will behave like deuterium ions since the relevant parameter along the formalism is the charge-to-mass ratio of the particles. In the case of D-T plasmas in a BPX, tritium with  $A/Z = 3$  will be singular, but deuterium and fully stripped impurities (in particular He) will

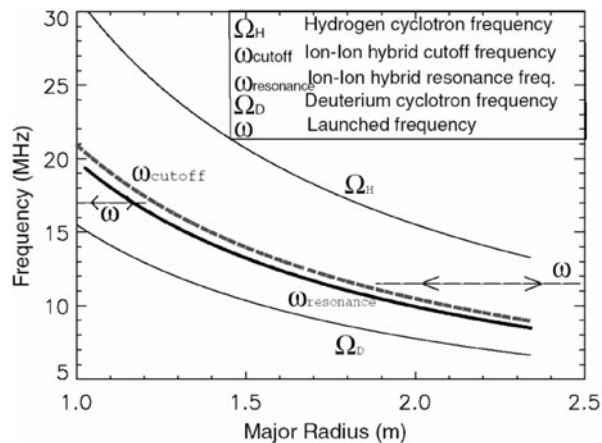


Fig. 34. Relevant frequencies (in MHz) for the DIII-D tokamak: ion-ion cutoff (dashed line), ion-ion resonance (thicker line) versus major radius for  $f_H = 44\%$ ,  $B = B_0 R_0/R$  and uniform density profile. Hydrogen and deuterium cyclotron frequencies are also shown. Possible useful launch frequencies from LFS and HFS are indicated with dashed lines with arrowheads. (From Ref. 295)

each have  $A/Z \approx 2$ ; thus,  $f_T$  can be directly determined from the diagnostic. However,  $f_D$  will require independent measurement of impurity concentrations or  $Z_{eff}$ .

On the technology side, heterodyne emitter receivers at the relevant frequencies (typically 100 MHz) can be developed at very low cost. The antenna technology is in principle simple (loop coils facing the plasma); however, in practice it would be the most critical element in the system due to its proximity to the plasma.

### VIII.B. Examples of Implementations

A measurement technique capable of determining ion mass ratio has been demanded for  $>10$  yr by the diagnostic community for its application to ITER and burning plasmas in general. However, only a few experiments focused on the fast wave interferometry/reflectometry technique have been performed over those years, mainly around the DIII-D tokamak.

The experiments at DIII-D started with proof-of-principle experiments around the mid-1990s (Refs. 293 and 294). Interferometry systems using Alfvén waves (60 MHz, 10 W launched) were able to measure the line-integrated mass density in very good agreement with standard interferometry. The main limitation at that time was the weak antenna-plasma coupling, due to the antenna design (small loops behind the wall graphite tiles), which produced frequent loss of signal and precluded operation of the system in divertor plasmas.

A new interferometry experiment, with improved antennas, was reported in 2003 (Ref. 292). This time the antenna was implemented in one of the protecting graphite tiles itself (by shaping it to a loop and taking advantage of the graphite conductivity). The system operated at 100 MHz, launching 20 mW and using a high-sensitivity heterodyne receiver. Again, the system worked well in acceptable agreement with the  $\text{CO}_2$  interferometer (significant analysis work is done in the referenced paper), and most limitations arose from the loss of signal for some scenarios. Figure 35 shows the evolution of the phase (quadrature signals) during one discharge: periods of good phase tracking and signal loss are observed. This system improved significantly the scenario range and showed that phase tracking losses were related to situations where the plasma edge moves away from the antennas (divertor plasmas) or when the edge density decreases, thus decreasing the coupling.

The first proof-of-principle experiment facing the problem of measuring the ion mix with fast wave reflectometry was also conducted in DIII-D (Refs. 295 and 296). The experiment used similar antennas (graphite loops) and electronics to that reported in the previous experiment. Operation was in the range 14 to 23 MHz, launching 20 mW from the LFS.

An overview of the results obtained is shown in Fig. 36. The discharge begins with deuterium and fully stripped impurities as main components; then, hydrogen

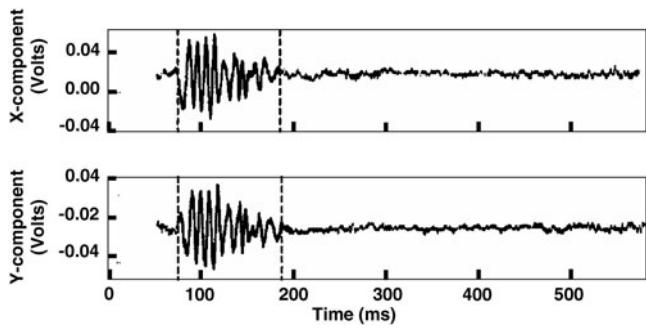


Fig. 35. Interferometry experiment in DIII-D. The quadrature phase components are shown. Phase tracking occurs between the hash marks, where both signals are nearly sinusoidal; outside this time frame the received signal is too low. (From Ref. 292)

gas puff (starting at  $t = 0.4$  s) increases  $f_H$ ;  $\omega_{cutoff}$  decreases; the reflecting point moves away from the antenna; and the reflectometer phase increases. At  $t = 0.5$  s, deuterium neutral beam injection commences, and  $f_H$  increases more gradually. The hydrogen puff ends at 0.8 s, so  $f_H$  and the reflectometer phase begin to decrease at this time.

The hydrogen concentration inferred from these measurements agrees quantitatively with the concentration inferred from fusion-reaction and spectroscopic diagnostics. A full analysis (as is done in classical microwave reflectometry) would require a broad frequency sweep in order to take into account profile evolution of both species. Also, the detailed reconstruction of  $f_H$  would require ray-tracing (or even full-wave) calculations to accurately invert the phase information.

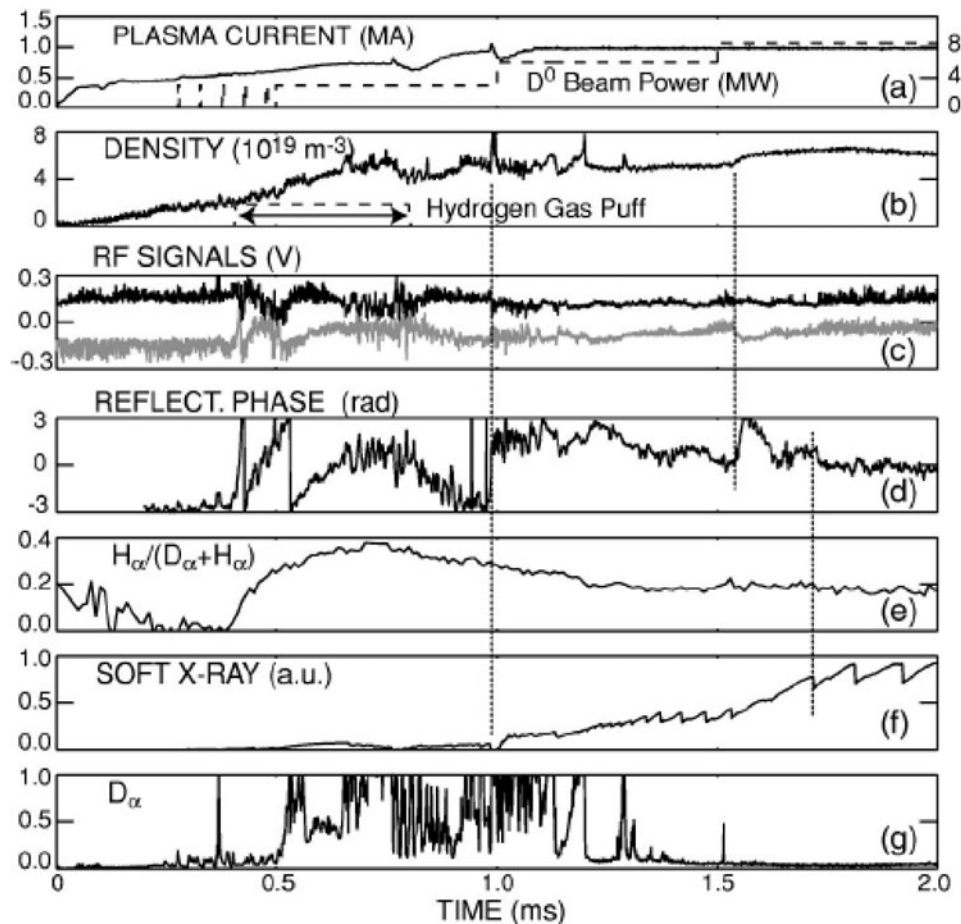


Fig. 36. Fast wave reflectometry experiment at DIII-D. Time evolution of (a) plasma current and injected beam power; (b) line-average electron density and timing of the hydrogen gas puff; (c) quadrature signal of the reflectometer diagnostic, with a dc offset introduced for clarity; (d) inferred reflectometer phase; and (e) spectroscopic measurement of the fraction of atomic hydrogen outside the plasma. Increased reflectometer phase indicates cutoff layer moving away from the antenna or increase in the hydrogen concentration  $f_H$ . The vertical lines highlight changes in the plasma conditions. LFS launching  $\omega/2\pi = 19.5$  MHz,  $B = 1.9$  T. (From Ref. 296)

Finally, impurity concentration, which affects the ratios  $n_D/n_e$  and  $n_H/n_e$ , is important and must be included in the calculations. Concerning diagnostic availability conditions, again, scenarios with large antenna-plasma gaps were difficult (loss of signal).

### VIII.C. Applicability to a BPX

As mentioned earlier, there is an urgent need for diagnostics that can measure the D-T ratio in burning plasmas. Fast wave reflectometry offers an interesting opportunity, which we will shortly discuss from the point of view of measurement interpretation and practical implementation (an illustrative analysis of the applicability of the technique to a BPX is done in Ref. 296).

Figure 37 shows the relevant frequencies for ITER compared with DIII-D. One first conclusion is that the access range is going to be narrow in frequency (which should be swept for optimum diagnostic information) and therefore in radius. From the interpretation point of view, wavelengths in ITER will be smaller, and therefore, WKB will be applicable. Warm plasma effects seem to be not very important. Launching from the HFS will have to go through the resonant hybrid layer (see Fig. 34) and therefore suffer from significant signal attenuation (which might not be a problem if more launching power or more sensitive receivers are available, provided cross-

talk signals do not dominate). The problem of antenna-plasma coupling needs to be assessed in depth. In particular, waves must overcome the evanescent layer in the low-density region at the plasma edge, and the possible impact on the measurement coming from changes on this region has to be evaluated.

Concerning fast wave interferometry, the access will be easier, the window between the ion cyclotron frequency and the ion plasma frequency is wider than its equivalent for the electrons, and this could be a way to measure the integrated mass density.

In terms of practical implementation, electronics will not be a problem given the broad range of low-cost sources and other components for the frequency range. Similarly, the data acquisition hardware will be readily available. Integration of the in-vessel components, such as the antennas, will require a deep analysis. Many of the integration issues are shared with the ion cyclotron heating antennas, in particular, the need for electrical insulators close to the plasma that might be affected by neutrons and other particles escaping from the plasma and the electromagnetic forces in the loop, which has to be very close to the plasma, during disruptions.

Some of those problems have been experienced, and overcome, recently with the active antennas for toroidal Alfvén eigenmode excitation, installed at C-Mod (Ref. 297) and JET (Ref. 298).

## IX. IMAGING AND VISUALIZATION DIAGNOSTICS

### IX.A. Introduction

Theoretical understanding of plasma equilibria and anomalous transport has been greatly extended with the help of the rapid advancement of computer technology, which, for example, has made it possible in extensive simulations to reveal elegant 3-D structures of plasma turbulence<sup>299,300</sup> and MHD fluctuations.<sup>301</sup> However, the core physics of MHD instabilities and the behavior of the turbulence remains poorly understood experimentally, which prevents the development of efficient means of MHD and turbulence suppression and improvement of plasma confinement. This is primarily due to the difficulty in diagnosing the full picture of the small-amplitude fluctuations and complex behavior of MHD phenomena in high-temperature plasmas.

As noted in Sec. II, information regarding  $\tilde{T}_e$  in the plasma core region was not available until the introduction of intensity interferometric techniques into the ECE diagnostic in 1993 (Ref. 45). More importantly, plasma fluctuation imaging diagnostics were not available until quite recently and are currently still in a relatively early stage of development.<sup>20</sup> Furthermore, quantitative analysis of the limitations<sup>113,302</sup> in conventional reflectometry (supported by experiments) has motivated the development of an imaging system based on

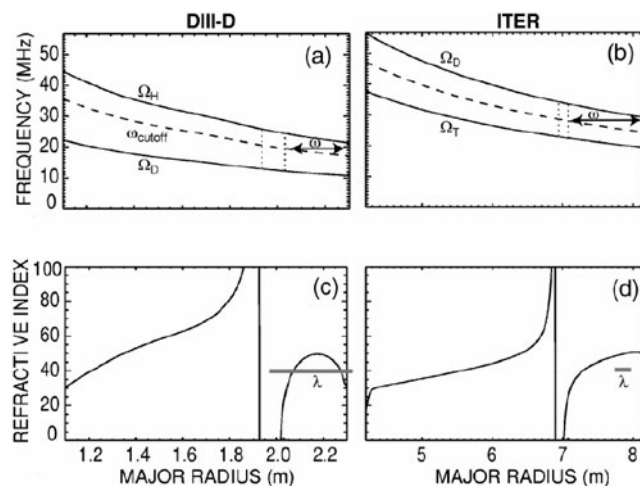


Fig. 37. Cyclotron frequencies  $\Omega_i$ , ion-ion hybrid cutoff frequency versus cutoff (dashed line), and launched frequency  $\omega$  (line with arrows) versus major radius  $R$  in (a) DIII-D and (b) ITER. The dotted vertical lines show the location of the resonance and cutoff layers, respectively. Index of refraction  $n$  versus major radius in (c) DIII-D and (d) ITER. The gray horizontal lines show the size of one wavelength when  $n = 40$  in the two devices. Typical profiles are assumed for both devices, with a uniform concentration  $f_H = 0.4$  for DIII-D and  $f_D = 0.5$  for ITER. (From Ref. 296)

reflectometry. Therefore, it is not surprising to learn that it has been impossible to conclusively verify or reject the predictions of computer simulations based on the limited experimental data. Of equal importance is the need for detailed study of the formation of transport barriers and zonal flows, which often appear to have fine-scale structures in profiles and therefore require high spatial and temporal resolution measurements.<sup>303</sup> Numerous studies have stressed the need for high-resolution imaging diagnostics, which will ultimately permit the visualization of these complicated 2-D and 3-D structures of both electron temperature and density. Examples of recent physics insights obtained through the development of novel imaging diagnostics instrumentation are contained in Ref. 304.

Sections IX.B and IX.C will discuss the significant progress that has occurred in ECEI and microwave imaging reflectometry (MIR) diagnostics. Here, much of this material is taken from Refs. 20 and 21, to which the reader is directed for more complete information.

### IX.B. Electron Cyclotron Emission Imaging

A number of development efforts have been directed toward techniques aimed at obtaining 2-D  $T_e$  profile measurements by ECE. In JET, several ECE radiometers were constructed and configured to measure the plasma along different angles.<sup>91</sup> Another way to obtain 2-D  $T_e$  profiles relies on the assumption that the plasma rotates poloidally as a rigid body; therefore, the temporal variations measured by a 1-D ECE system near the plasma midplane can be interpreted as poloidal variation.<sup>43,44</sup> Important experimental results regarding plasma equilibria<sup>91</sup> and MHD fluctuations<sup>43,44</sup> have been obtained using this approach. In the ECEI approach, the single antenna of a conventional heterodyne ECE radiometer is instead replaced by an array of antennas, using large-diameter optics to image the plasma onto the array, which transforms the 1-D radiometer into a true 2-D imaging diagnostic, thereby permitting time-resolved 2-D fluctuation measurements.

Shown in Fig. 38 is a schematic diagram outlining the principle of ECEI compared to a conventional 1-D ECE system. ECE radiation is collected and imaged onto a mixer/receiver array consisting of planar antennas with integrated Schottky diodes. The vertically arranged array elements are aligned along the E-field (vertical) direction to collect second-harmonic X-mode radiation. Large-diameter optics image the plasma emission onto the array, enabling each array element to view a distinct plasma chord. Using the one-to-one mapping of ECE frequency to major radius in tokamak plasmas allows the ECEI focal plane to be swept through the plasma by sweeping the receiver frequency of the array, thereby forming 2-D images of the  $T_e$  profile.<sup>305</sup> ECEI was developed and implemented on the TEXT-U tokamak.<sup>47,305-309</sup> This was followed by an ECEI system on the RTP tokamak<sup>310</sup> and

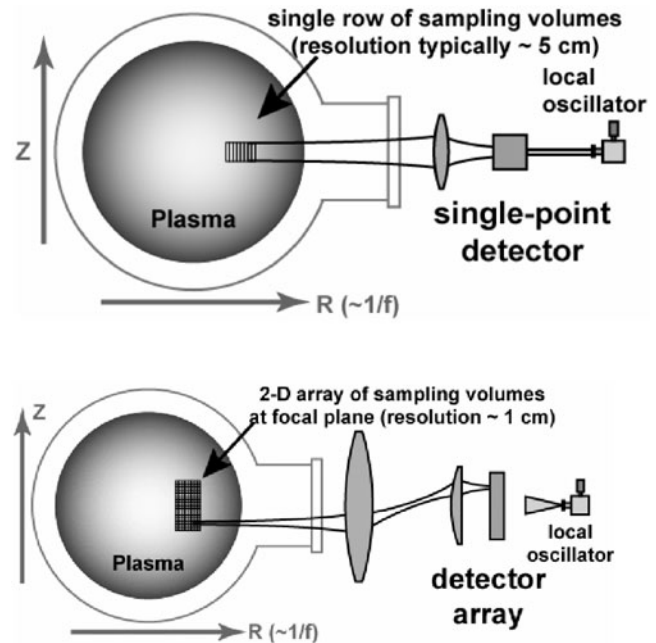


Fig. 38. (a) Conventional ECE system utilizes a single detector and wideband sweeping LO source. (b) ECEI system with a quasi-optical 1-D detector array. It is similar to the many vertical layers of a conventional ECE system. (From Ref. 21)

more recently on the TEXTOR tokamak.<sup>311</sup> ECEI systems have now also been developed and installed on mirror machines and stellarators.<sup>312,313</sup>

The success of ECEI is due, in large part, to its ability to form high-resolution  $T_e$  images. Here, the compact imaging array, the large horizontal port, and the large-aperture imaging optics all contribute to the superior spatial resolution of the ECEI system in the transverse direction of the sight lines. However, it is noted that this could be a drawback for large burning plasma devices like ITER where access is quite limited. Horizontally, the sample volume size is limited by the rf bandwidth as well as the radiation bandwidth that arises from the magnetic field gradient, Doppler broadening, and relativistic broadening.<sup>32,34</sup> In the various ECEI systems developed to date, the sample volumes were essentially 1.0-cm cubes (diameters at  $1/e$  power).

Since most of the ECEI sight lines are off axis, refraction effects become important at high densities. From ray-tracing calculations, it is found that the focusing effect of the plasma is not important; i.e., the beam waist location and spot size within the plasma are relatively unaffected, while the bending of the sight line can be quite significant. This can be corrected in the data analysis with readily obtainable density profiles in most machines since the sight lines in vacuum are accurately measured.

Turbulent temperature fluctuations are measured with ECEI using the technique of intensity interferometry.<sup>31,46,47,210,305–307,314–318</sup> One of the approaches is illustrated in Fig. 39a. Because of the natural line width of ECE radiation,<sup>10</sup> each frequency band corresponds to an extended plasma volume thickness along the measurement sight line. When the frequency bands are close to each other, the plasma volumes will be mostly overlapped, with their separation much less than the correlation length of turbulent fluctuations. Therefore, the two resultant signals have essentially the same temperature fluctuation. However, once the filters have sufficient isolation, i.e., more than  $-20$  dB at the cross point, the radiation noise of the two signals is uncorrelated.<sup>46</sup> The cross correlation between the two signals then yields the

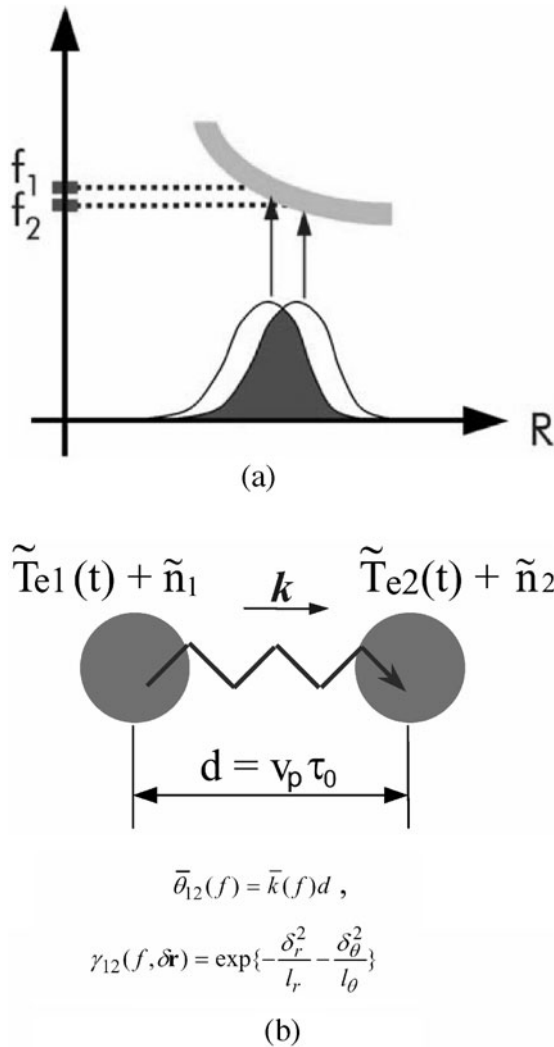


Fig. 39. (a) Correlation measurement of local electron temperature fluctuations. (From Ref. 20) (b) Two-point correlation measurement of electron temperature fluctuations.

local values of the temperature fluctuations.<sup>46,310</sup> Another approach is illustrated in Fig. 39b. Because distinct plasma volumes have uncorrelated radiation noise, the signals from two such volumes can be cross-correlated (provided their separation is not too much larger than the fluctuation correlation length) to determine the wave dispersive properties.

The need for ECEI was demonstrated through experiments on the TEXT-U tokamak. When the first  $\tilde{T}_e$  data from the plasma core were available, it was found that critical information such as the poloidal wave number and correlation length could not be obtained using conventional ECE radiometers. In addition, the relatively poor spatial resolution of conventional 1-D ECE measurements, where the beam waist was  $\sim 2$  cm near the core of the plasma, limited the sensitive wave number spectral range because of sample volume effects.<sup>31,309,314</sup> Here, the maximum wave number  $k_{mzx}$  is given by  $k_{mzx} = 2\sqrt{2}/d$ , where  $d$  is the  $1/e$  poloidal diameter of the sample volume.<sup>309</sup> These problems were solved when the high-spatial-resolution ECEI diagnostic was developed and implemented on TEXT-U, which measured the poloidal wave numbers, statistical dispersion relations, and poloidal correlation lengths of electron temperature fluctuations in the plasma core for the first time (see Refs. 47 and 310). In these measurements, the sample volumes are poloidally separated, so that poloidal wave numbers were obtained. Since the vertical slice of the sample volumes can be moved horizontally, the separation can be poloidal or radial. This is the flexibility of ECEI. However, the ECEI systems discussed above were basically 1-D systems; i.e., at each instant of time, only a single slice of the plasma is measured. This gives rise to ambiguity in the data interpretation when the sample volume separation has both poloidal and radial components.

The optical layout of the ECEI system developed for TEXTOR is shown in Fig. 40 (Ref. 21). A multifrequency heterodyne receiver is constructed for each of the imaging channels, so that 2-D maps of  $T_e$  profiles and fluctuations within the sample volume as shown in Fig. 41 can be obtained in a single discharge. For the study of  $\tilde{T}_e$  turbulence, the instrument makes it possible to simultaneously and unambiguously measure  $\langle k_r \rangle$  and  $\langle k_\theta \rangle$  (time averaged), which is essential for mode identification. In the case of  $T_e$  profiles and coherent mode phenomena such as various MHD instabilities, this allows direct observation of island/rotation without the assumption of rigid body rotation.

The 20-channel (16 are used in the experiment) dual-dipole printed circuit antenna/mixer imaging array incorporating wideband baluns and low-noise microwave preamplifiers was introduced for the new ECEI detection array. Wide rf bandwidth has been achieved using broadband antennas and a high-power 90- to 136-GHz BWO as the LO source. Owing to the improved sensitivity with dual-dipole antenna elements, the LO drive power is sufficient for the 105- to 127-GHz tunable

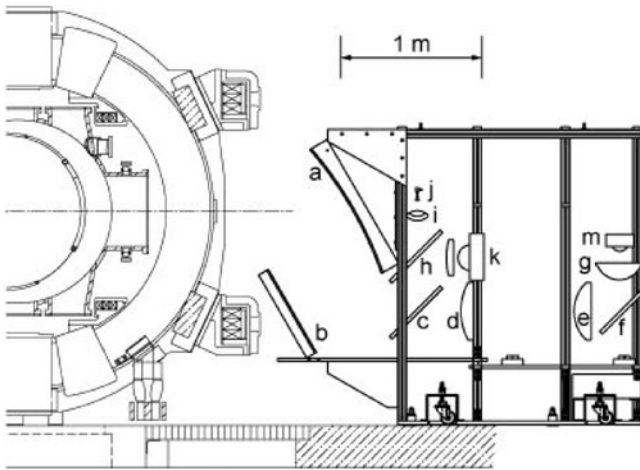


Fig. 40. Detailed schematic of the TEXTOR ECEI/MIR system: a, poloidal focusing mirror; b, toroidal focusing mirror; c, beam splitter for MIR and ECEI; d, H-plane focusing mirror for ECEI system; e, E-plane focusing mirror for ECEI system; f, flat mirror; g, moveable lens for the ECEI system focal depth change, h, beam splitter for MIR source and signal (i and j) MIR source beam and collimating lens; k, MIR detection array; m, ECEI array. (From Park et al., 2004)

bandwidth of the present system. The collected ECE radiation over a broad frequency range through the optical view is downconverted with a fixed-frequency LO to provide a wide IF bandwidth input signal. Once amplified, the input signal is then divided into eight equal parts using a printed divider designed on a microstrip transmission line. The divided signals are then mixed down, each with a distinct LO frequency ( $\sim 500$ -MHz separation ranging from  $\sim 3$  to  $\sim 7$  GHz), using low-cost balanced mixers. A total of eight different LO signals are required to downconvert the 2-D ECEI signals, with 16 LO outputs per frequency.

One of the first experimental studies of  $T_e$  fluctuations using the new ECEI system concerned  $m = 1$  oscillations (sawteeth), which are well-established MHD phenomena in tokamaks. The sequence of the sawtooth crash is clearly illustrated in Fig. 41. With the new ECEI “camera,” it was demonstrated that during the sawtooth collapse the heat from the center of the plasma flows to the outside via a small perturbation in the magnetic field confining the plasma. The measurements provide a 2-D picture of the perturbation of the magnetic field, and this makes it possible to compare the measurements in a very direct way with predictions from various theoretical models. The comparison has led to the conclusion that one model can be completely discarded,<sup>319</sup> as it cannot describe any of the details seen in the experiment. Two other models that were tested each only can describe a part of the sawtooth evolution.<sup>320,321</sup> The physical mechanisms unveiled by 2-D images now provide a target

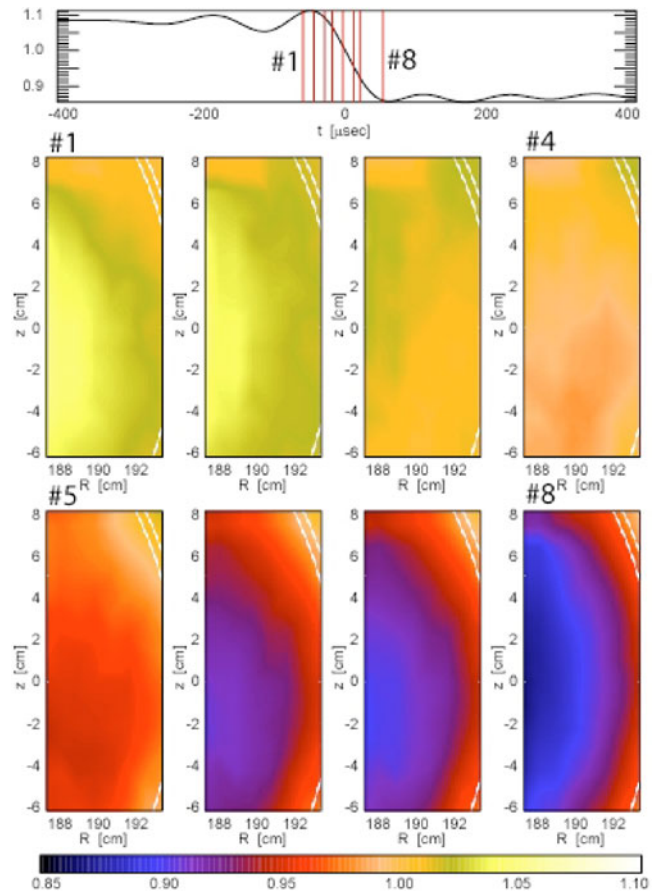


Fig. 41. Eight frames of the  $m = 1$  mode during the crash phase. The “hot  $m = 1$  mode” approaches the inversion radius before the crash at the lower field side of the magnetic configuration. Heat spreads along the inversion radius, and the cold island develops and sets in inside the inversion radius. The process is indicative of “x-point” magnetic reconnection in the partial reconnection model. Note that the double white lines represent the estimated inversion radius. (From Park et al., 2004)

for theorists to develop new models or to adjust their existing models. Hopefully, this will lead to a complete understanding of the sawtooth instability. An ECEI instrument combined with a prototype MIR system has also been developed for use on the LHD at the National Institute for Fusion Science in Japan.<sup>312,313</sup> The frequency of the second-harmonic ECE on LHD ranges from 120 to 180 GHz. Because of the large distance between the plasma and the window, an ellipsoidal mirror and a plane mirror are mounted inside the vacuum vessel and converge the ECE signals to pass through a 192-mm-diam fused-quartz vacuum window. The signals are subsequently imaged onto a detector array. An object plane located at the plasma center is 2.7 m in front of the ellipsoidal mirror.



The progress of imaging diagnostic systems based on ECE has clearly demonstrated the importance of visualization of complex multidimensional phenomena.

### IX.C. Microwave Imaging Reflectometry

As discussed in Sec. IV, the microwave reflectometry technique has been used for many years for measurement of electron density profiles and fluctuations, a usage made common because of its relatively simple implementation and its high sensitivity to the behavior of the cutoff layer.<sup>113,131,153,201,322–328</sup> Excellent reviews of this technique are given in Refs. 103, 132, 288, and 289. Despite the long-standing use of reflectometry for fluctuation measurements, however, its viability for conditions of strong turbulence and/or core measurements remains an outstanding issue.<sup>101,113,131,132,290–292,329</sup>

In the presence of density fluctuations, the reflected electromagnetic wave spectrum is broadened with a strong weighting by those fluctuations in the vicinity of the cutoff layer. In the simplest case of small-amplitude fluctuations and a 1-D plane stratified plasma permittivity,  $\varepsilon = \varepsilon_0(r) + \tilde{\varepsilon}(r)$ , with  $\tilde{\varepsilon}(r) \ll 1$ , the fluctuating component of the measured phase is given by the 1-D geometric optics approximation<sup>302</sup>

$$\tilde{\phi} = k_0 \int_0^{r_c} \frac{\tilde{\varepsilon}(r)}{\sqrt{\varepsilon_0(r)}} dr, \quad (99)$$

and the power spectrum of the reflected phase fluctuations is related to that of the density fluctuations<sup>302</sup>

$$\Gamma_{\phi}(k_r) = \pi M k_0^2 L_n \Gamma_n(k_r) / |k_r|, \quad (100)$$

where  $L_n = n/(dn/dr)_{r=r_c}$  is the density scale length,  $M = (n(\partial\varepsilon/\partial n)_{r=r_c}^2)$  (1 for O-mode and 4 for X-mode), and it was assumed that  $k_r < k_0/(k_0 L_\varepsilon)^{1/3}$ , where  $L_\varepsilon = (d\varepsilon_0/dr)_{r=r_c}^{-1}$ . One can see that the fluctuating phase of the reflected wave is dominated by the change in permittivity close to the cutoff layer, due to the factor  $1/\sqrt{\varepsilon_0(r)}$  in the integral, which becomes very large near the cutoff (as the group velocity approaches zero). Indeed, this is one of the most valuable features of reflectometry as a fluctuation diagnostic.

The 1-D geometrical optics approximation unfortunately breaks down in the case of multidimensional turbulent fluctuations, which is precisely the case of interest for magnetic fusion plasmas, which exhibit both radial and poloidal variations. In this case (under conditions of sufficiently large amplitude and/or wave number turbulence), the reflected field at the detector is a complicated interference pattern, and the spectral information about the fluctuations themselves is lost. The use of MIR to overcome this limitation has been documented through a series of experimental and theoretical studies, which have revealed the need for reflectometric imaging, together

with the failure of standard fluctuation reflectometry under such conditions.<sup>113,302,330–333</sup>

The difference between standard 1-D and 2-D reflectometry is readily apparent from Fig. 42. With 1-D fluctuations, the reflection layer will move back and forth in the radial direction, resulting in the phase changes in the reflected wave. With 2-D fluctuations, the backward field contains components from multiple fragmented wave fronts, resulting in a complicated interference pattern at the detector plane. This interference results in both amplitude and phase modulations in the detected signal, leading to a breakdown of the simple relationship between phase fluctuations and density fluctuations. This was experimentally demonstrated on TFTR where the in-phase and quadrature reflectometer components were shown to behave as two independent variables with zero mean.<sup>302</sup> Detailed numerical studies verified this interpretation and also revealed that density fluctuation information can be retrieved using data obtained with specially designed imaging reflectometers, where the virtual reflecting cutoff layer is imaged onto the detector plane.<sup>113,302</sup> In the numerical study in Ref. 302, a plane-stratified plasma is perturbed by a wide spectrum of 2-D fluctuations with random phases. The phase of the reflected wave was simulated using a range of fluctuation amplitudes and spectral widths, and the results showed (as observed experimentally) that large fluctuations cause large-amplitude modulations and random phases at the detector plane, exhibiting predictable statistical behavior of both phase and amplitude. The basic problem in extracting useful phase information from standard reflectometry data is that the measurements are usually performed at a large distance ( $r > r_b$ ) from the reflecting layer where (in the absence of optical imaging) the reflected wave front is scrambled (Fig. 42b). As a result, what is sampled is a complicated interference pattern, with characteristics that may be completely different from those of the actual plasma fluctuations under investigation. The results from this numerical work exhibit the strong dependency of reflectometer signals on the two quantities  $k_\theta$  and  $\Delta\phi$ , consistent with the expression for diffraction distance<sup>155</sup> defined as

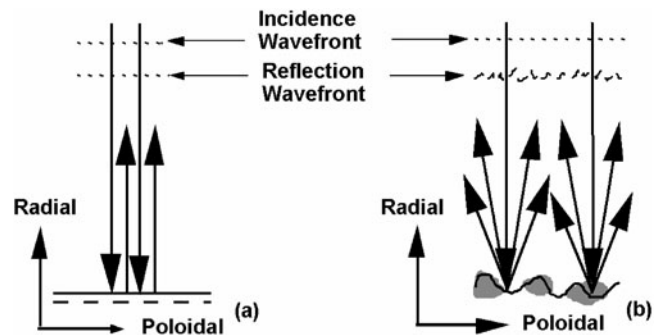


Fig. 42. Comparison of (a) 1-D and (b) 2-D reflectometry.

$$D_{diff} \approx \frac{2k_0}{[\Delta k_\theta^2(1 + \sigma_\phi^2)]},$$

where

$$\sigma_\phi \approx \langle \Delta\phi^2 \rangle^{1/2}$$

$\Delta k_\theta$  = width of the poloidal mode spectrum.

As a rough guide, one can expect interference to play a significant role in the reflected field pattern if measurements are taken beyond  $D_{diff}$ . In practice, the diffraction distance can be used as a measure of the validity of the 1-D system data.

If the reflected rays are collected by a large-aperture optical system, the spatial structure of the density fluctuations near the cutoff layer can be determined by a reconstruction of the reflected wave front at the image plane. Phase fluctuations measured at the image plane will directly correspond to density fluctuations at the cutoff layer. Additionally, the use of imaging optics enables the simultaneous sampling of an extended region of the cutoff layer by an extended array of detectors at the image plane. It is important to reiterate that the use of imaging optics extends the region of validity for reflectometry as a fluctuation diagnostic even for a single detector corresponding to a small probing beam. The use of multiple detectors to measure an extended plasma layer is a secondary benefit of the presence of imaging optics.

Shown in Fig. 43a is a schematic diagram outlining the experimental realization of reflectometric imaging based on the ECEI system shown in Fig. 40. Here, a broad area of the plasma cutoff layer is illuminated by a millimeter-wave source, and focusing optics are utilized to transform the output of the illuminating source (typically a solid-state oscillator) into an extended beam whose curved wave front is designed to roughly match the poloidal/toroidal shape of the plasma cutoff surfaces. This wave front curvature matching enhances the amplitude of the reflected waves and ensures that a sufficient fraction of the incident electromagnetic power is coupled to the MIR receiver for detection. The reflected radiation passes back through the same optics as the illuminating beam, with additional optics utilized to image the reflecting layer onto the detector array. A second millimeter-wave source provides LO power to the detector array, yielding output signals whose frequency is that of the difference frequency between the two sources. A quadrature detection system yields the fluctuating phase and amplitude signals on each array element. Unlike the ECEI system, the MIR system requires a relatively powerful probing beam to be launched through the optical system while the expected signal level at the array coming from plasma reflections is relatively small.

Proof-of-principle experiments employing the systems shown in Fig. 43a have been performed on the TEXTOR tokamak using fixed-frequency versions of both the ECE and reflectometer subsystems, confirming the

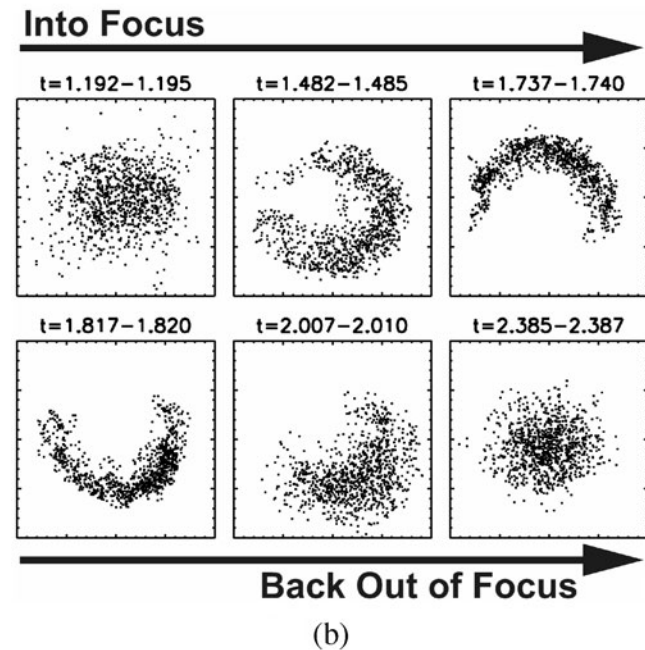
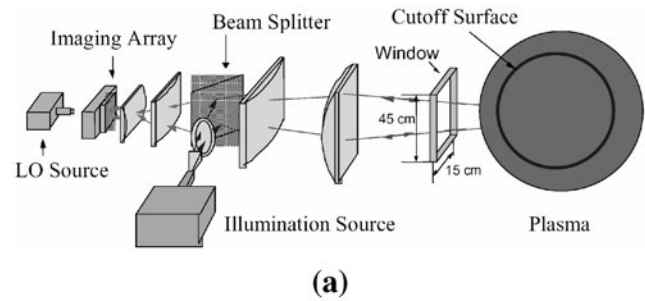


Fig. 43. (a) System configuration of an imaging reflectometry system and (b) complex polar field amplitude plot from the prototype TEXTOR-94 MIR system as the cutoff layer is swept through the focal plane of the imaging optics. Each frame represents a 3-ms time window. (From Munsat et al., 2003)

feasibility of the imaging scheme. One of the most significant results from the prototype MIR system is the demonstration of the virtual cutoff surface. In this experiment, both the probing frequency and the focal plane of the optics were held fixed, and the electron density was ramped over the course of the shot to bring the cutoff surface through and beyond the focal plane of the optics. Figure 43b shows the complex signal recorded over several 3-ms duration time windows as the cutoff surface moves outward through and beyond the optical focal plane. Both the characteristic crescent-shaped phase modulation when the cutoff is in-focus and the fill-in of the complex plot as the cutoff moves out of focus are clearly identifiable.

In addition to the detailed component tests, a comprehensive study to demonstrate the capabilities and

limitations of the MIR technique has been investigated, both theoretically and experimentally. This included a systematic laboratory study of reflectometry systems using corrugated reflecting targets of known shape to simulate the fluctuating plasma reflection layer. Each reflecting target was tested using both the MIR configuration and a standard 1-D configuration consisting of a launched Gaussian beam and a receiving horn with no optics (see Refs. 331 and 334 for the test layouts). As a reference, each surface was independently measured using a visible-laser interferometer (Leica “Laser Tracker”).

A result from this off-line study is shown in Fig. 44, in which both the MIR and 1-D instruments were used to reconstruct the phase of a target mirror with corrugations of  $k_\theta = 1.25 \text{ cm}^{-1}$ . The off-line reflectometry study, as well as the characterization of the TEXTOR imaging reflectometer, is detailed in Refs. 331 and 333. Figure 45a compares data from the 1-D configuration (located 30 cm from the target surface) to the reference measurement, and Fig. 45b compares data from the MIR instrument (located at the MIR focal plane, 235 cm from the target surface) to the reference measurement. Clearly from the plots, the MIR system faithfully reproduces the target fluctuations (at a distance consistent with actual experimental conditions) while the conventional reflectometer data become completely distorted, even at a distance of 30 cm, significantly less than the distance from plasma to horn in most fusion plasma reflectometer systems. This simple experiment demonstrates both the difficulties of interpreting conventional reflectometry data and the solutions offered by MIR techniques.

In order to quantify the degree to which the reflectometer measurements accurately reproduce the shape of the reference surface, the cross correlation was calculated between the power spectra produced by the two reflectometers and the reference curves. Cross-correlation figures were calculated for measurements taken over a wide range of  $d$ , the distance between the instrument and

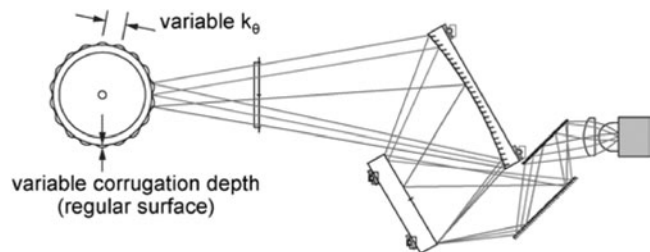


Fig. 44. Laboratory setup for MIR system testing using a corrugated target mirror. Each target was tested using both the MIR configuration (above) and a standard 1-D configuration (not shown) consisting of a launched Gaussian beam and a receiving horn with no optics. As a reference, each surface was independently measured using a visible-laser interferometer (Leica “Laser Tracker”). (From Munsat et al., 2003)

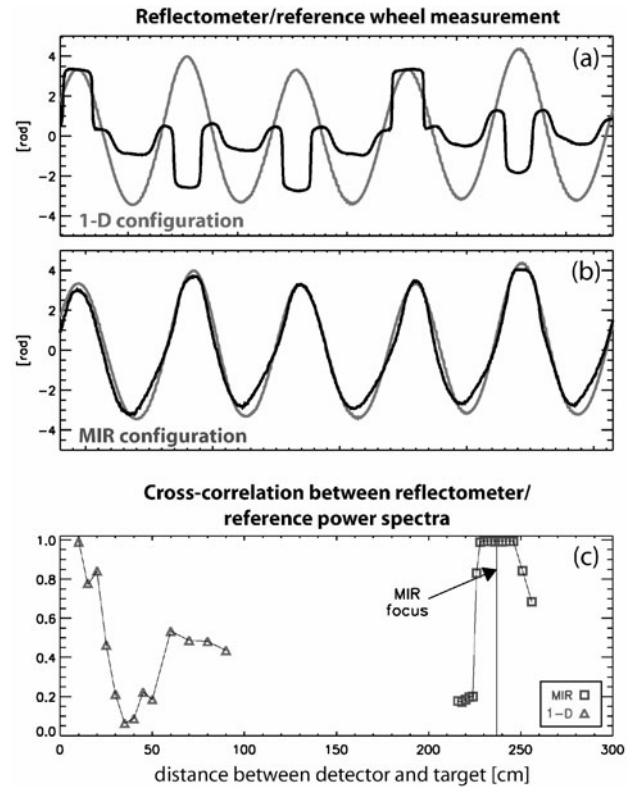


Fig. 45. Comparison of 1-D and MIR reflectometer signals, using target reflector with  $k_\theta$  of  $1.25 \text{ cm}^{-1}$ . Comparison of (a) 1-D measurement (From Munsat et al., 2003) and (b) MIR measurement to reference measurement (green curve; color online). The 1-D measurement was taken at a distance of 30 cm, and the MIR measurement was taken at a distance of 235 cm. Plot (c) is the cross correlation of the power spectra produced by the 1-D and MIR reflectometers, plotted as a function of  $d$ , the distance between the instrument and the target surface. The MIR focal plane is indicated by the vertical line at  $d = 237 \text{ cm}$ .

the target surface. These data, plotted for both the 1-D and MIR systems, are shown in Fig. 45c.

For the 1-D case, the correlation is nearly unity for  $d \sim 10 \text{ cm}$ , and falls to  $\sim 40\%$  as the distance is increased to 30 cm or more. For the MIR system, there is near-unity correlation between the signal and reference curves everywhere within  $\pm 10 \text{ cm}$  of the focal distance, with a relatively sharp falloff as the image becomes unfocused, and the recorded phase begins to exhibit phase runaway. The strong correlation over this 20-cm range represents the distance over which multiradial (multifrequency) data could be collected simultaneously with a fixed set of imaging optics. Importantly, these data are taken with the instrument located at a distance of  $> 200 \text{ cm}$  from the reflecting surface, in exactly the configuration used for TEXTOR measurements.

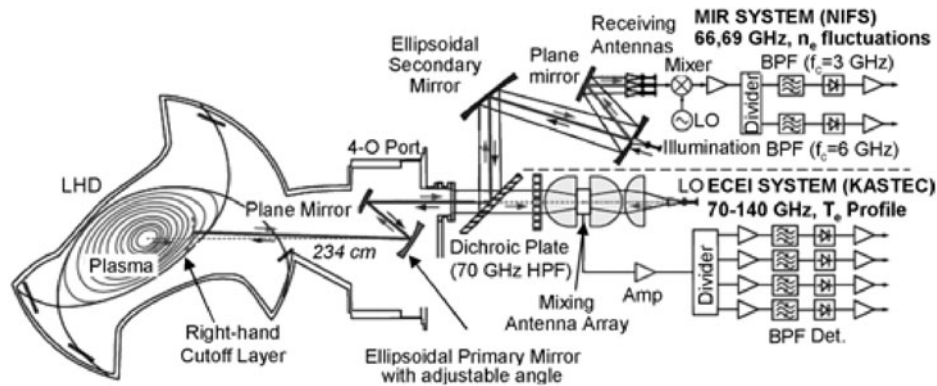


Fig. 46. Schematic of the microwave imaging system of MIR and ECEI in LHD. (From Ref. 335)

#### IX.D. Simultaneous ECEI/MIR System

To resolve the relation between anomalous transport and microturbulence, there is a need for simultaneous  $n_e$  and  $T_e$  fluctuation measurements, and successful test results on TEXTOR have enabled operation of a system to measure both fluctuations simultaneously. More recently, the development of a system for LHD has been undertaken.<sup>335</sup> Figure 46 illustrates the configuration for the combined ECEI and MIR LHD system using reflective optics and a dichroic plate to separate the ECEI and MIR signals in frequency space. The dichroic plate is essentially a high-pass optical filter whose electromagnetic wave transmission and reflection coefficients vary with frequency or polarization. The most commonly used form of dichroic plate consists of a thick metallic screen perforated with regularly spaced uniform circular holes. Detailed design criteria can be found in Refs. 336 and 337.

As noted above, a combined ECEI and MIR system has been routinely operated on the TEXTOR tokamak. While the ECEI system has been focused on physics studies of  $m = 1$  and  $m = 2$  modes, the MIR system has been undergoing changes in alignment procedures to address the validity of the imaging system beyond the laboratory tests. In this combined system, the primary components of a microwave optical system are shared between ECE and reflectometer subsystems, with each subsystem using a dedicated high-resolution multichannel detector array. The basic layout is shown in Fig. 40, including a cross section of the TEXTOR vacuum vessel, the primary focusing mirrors, and the two diagnostic subsystems. Instead of employing a dichroic plate, a 50/50 wire grid beam splitter, which may lower the sensitivity of both systems, has been used to separate the two systems.

#### IX.E. Applicability to a BPX

The large optical access required to take full advantage of MIR and ECEI almost certainly precludes their

applicability to a BPX where it is necessary to restrict neutron streaming. However, it should be stressed that in the case of reflectometric studies of fluctuations, imaging may be necessary even for a single-channel system. In addition, imaging of small regions appears feasible in a BPX. Many of these issues are expected to be answered during the development of a combined ECEI/MIR system, which is planned as one of the KSTAR tokamak baseline diagnostic instruments.<sup>338,339</sup>

### X. SUMMARY AND OUTLOOK

Microwave diagnostics are expected to play a vital role in burning plasma diagnostics. Their short wavelength (relative to rf) results in relatively modest access requirements, which is an extremely important consideration. Conversely, their long wavelength, relative to visible, makes them relatively easy to implement since it means that they can work down pipes (almost the only diagnostic that can do that). Given that microwave technology frontiers are rapidly advancing because of the numerous scientific, commercial, and military applications that demand ever-increasing levels of performance while also requiring reduced cost, an increased level of performance can be expected from microwave diagnostic systems. However, there remain a number of issues to be addressed, both in the interpretation of the measurement results and in the need for development of new microwave instruments.

ECE will continue to play an important role and will employ comparable frequency systems to those in current use. Looking toward ITER and future BPXs, important research and development focus issues include optics and beam transport, radiation hardness, and calibration. In addition, at the high temperatures expected ( $>10$  keV), there will be significant relativistic broadening leading to harmonic overlap and accessibility limitations and a degradation in the spatial resolution that can be achieved.

Departures in the electron distribution function from Maxwellian have apparently been observed on JET and TFTR at high values of additional heating,<sup>32,37</sup> which, if they occurred on ITER, would further complicate the measurement. Studies of the impact on these issues continue together with possible amelioration techniques such as the use of oblique viewing systems. As mentioned in Sec. II.D, improved calibration techniques have been shown on JET to yield improvements in both data smoothness and robustness.<sup>26</sup> The need for oblique view ECE systems will be determined from studies using the new JET system.<sup>40,340</sup> This is extremely important as it will help to determine the benefits of adding an oblique view to the ITER ECE port plug.

As discussed in Sec. III, EBE diagnostics are of importance in current physics studies of overdense plasmas (reversed field pinches, spherical tori, and higher-aspect-ratio tokamaks and stellarators that operate at high  $\beta$ ) where conventional ECE electron temperature radiometric measurements cannot be employed. However, EBE diagnostics have limited applicability for future BPXs. The exception is the possible use of EBE for diagnosing the electron temperature in the divertor region, where the plasma will be very dense and operating well into the overdense regime and the EBE antenna as the magnetic field geometry and density profile changes in the divertor.

Reflectometry is expected to play an important role on ITER. Currently, it is envisioned to have an LFS reflectometer system that probes the electron density by reflecting microwave radiation from both the O-mode and X-mode plasma cutoffs. The operating frequency ranges are 15 to 155 GHz and 76 to 220 GHz, respectively. The LFS O-mode system will be used to provide the profile in the outboard gradient region in the density range  $0.03 \times 10^{20}$  to  $3 \times 10^{20} \text{ m}^{-3}$ , while the LFS X-mode system will be used to probe the scrape-off layer profile. An HFS system employing X-mode at the left-hand cutoff will measure the core profile, while O-mode will be used to measure the density profile in the gradient region of the inner midplane. These systems will benefit greatly from ongoing advances in amplifier and detector technology.<sup>334,341–343</sup> Currently, studies are underway aimed at assessing the desirability of utilizing Doppler reflectometry on ITER (Ref. 344), which, among other quantities, can provide plasma rotation profiles.<sup>162</sup> In the data interpretation arena, as noted in Secs. IV.C and IX.C, a major issue to be resolved concerns the use of reflectometry as a fluctuation diagnostic (distinct from its use as a profile diagnostic). The use of large optical imaging systems as conceived by Mazzucato<sup>345</sup> has been shown to restore the phase fronts under the proper conditions but has the undesirable feature of requiring large optics, particularly to fully take advantage of its multichannel imaging capability. It has therefore been proposed for synthetically image density fluctuations in fusion plasmas where, under restricted conditions, it is suggested

that an image can be produced without need of a large lens.<sup>346</sup> However, this proposal remains to be demonstrated. Currently, a significant measurement need concerns the divertor region of ITER where the divertor reflectometer poses significant technological challenges in that densities up to  $10^{21} \text{ m}^{-3}$  must be probed and O-mode systems require frequencies up to  $\sim 1 \text{ THz}$  (Ref. 171). As noted by the authors, this is a major challenge to conventional reflectometer approaches. One possibility is to employ a broadband THz short pulse (i.e., to employ the ultrashort pulse reflectometer technique briefly described in Sec. IV). More details regarding millimeter-wave reflectometry on ITER may be found in Ref. 329.

Sections V, VI, and VII discussed the use of microwave CTS for the study of density fluctuations and determination of the ion distribution function (see Chapter 4, "Laser-Aided Plasma Diagnostics," by A. J. H. Donné, C. J. Barth, and H. Weisen, in this special issue of *Fusion Science and Technology*, for laser implementations). As noted in Sec. VII, gyrotron-based CTS has been proposed as a viable diagnostic for characterizing fusion-born alpha-particle distributions in ITER (Refs. 280 and 291). The case of wave number resolved scattering for the study of microturbulence is quite different. Currently, it is not planned to install on ITER a dedicated scattering system for microturbulence studies but rather to use other microwave-based diagnostics (reflectometer and ECE) systems, together with the laser-based interferometer/polarimeter systems, to obtain measurements on fluctuations. However, it continues to provide information on critical physics issues related to burning plasmas. In particular, as noted earlier, there are millimeter-wave scattering experiments on both DIII-D and NSTX aimed at providing crucial information on the effect of high- $k$  turbulence on electron transport, an understanding of which is crucial for magnetic fusion.<sup>194,195,223</sup>

Fast Alfvén wave interferometry and reflectometry were described in Sec. VIII. Here, it was noted that in terms of practical implementation, the main issues concern integration of the in-vessel components, such as the antennas. They have potential to provide useful information on ITER, but the details of the applications need to be developed.

## ACKNOWLEDGMENTS

The careful reading of the manuscript and helpful suggestions by A. Costley are gratefully acknowledged. Support from the U.S. Department of Energy and the National Natural Science Foundation of China is also acknowledged.

## REFERENCES

1. F. F. CHEN, *Introduction to Plasma Physics and Controlled Fusion*, 2nd ed., Vol. 1, Plenum Press (1979).

2. Z. SHEN, N. ITO, E. SALATA, C. W. DOMIER, Y. LIANG, N. C. LUHMANN, Jr., and A. MASE, "Frequency Selective Surface Notch Filter for Use in a Millimeter Wave Imaging System," *Proc. IEEE Antennas and Propagation Society Int. Symp.*, IEEE (2006).
3. T. H. STIX, *Waves in Plasmas*, American Institute of Physics, New York (1992).
4. T. J. M. BOYD and J. J. SANDERSON, *The Physics of Plasmas*, Cambridge Press, Cambridge (2003).
5. M. BRAMBILLA, *Theory of Plasma Waves in Homogeneous Plasmas*, p. 96, The International Series of Monographs on Physics, Oxford Science Publications (1998).
6. N. KRALL and A. W. TRIVELPIECE, *Principles of Plasma Physics*, McGraw-Hill (1973).
7. D. C. MONTGOMERY and D. A. TIDMAN, *Plasma Kinetic Theory*, McGraw-Hill (1987).
8. D. R. NICHOLSON, *Introduction to Plasma Theory*, John Wiley & Sons, New York (1983).
9. J. D. JACKSON, *Classical Electrodynamics*, Wiley & Sons (1999).
10. I. HUTCHINSON, *Principles of Plasma Diagnostics*, Cambridge University Press, Cambridge (1987).
11. N. C. LUHMANN, Jr. and W. A. PEEBLES, "Instrumentation for Magnetically Confined Fusion Plasma Diagnostics," *Rev. Sci. Instrum.*, **55**, 279 (1984).
12. H. J. HARTFUSS and M. HÄSE, in *Proc. 10th Joint Workshop Electron Cyclotron Emission and Electron Cyclotron Heating (EC-10)*, Ameland, The Netherlands (1997).
13. N. C. LUHMANN, Jr., "Instrumentation and Techniques for Plasma Diagnostics: An Overview," *Infrared and Millimeter Waves*, Academic Press, p. 1-65 (1979).
14. M. SATO et al., "Relativistic Downshift Frequency Effects on Electron Cyclotron Emission Measurement—Measurements of Electron Density in Tokamak and Electron Temperature in LHD," *Proc. 13th Joint Workshop Electron Cyclotron Emission and Electron Cyclotron Resonance Heating (EC-13)*, Nizhny Novgorod, Russia, 2004.
15. M. SATO, A. ISAYAMA, N. IWAMA, and K. KAWAHATA, "Feasibility of Electron Density Measurement Using Relativistic Downshift of Electron Cyclotron Emission in Tokamak Plasmas," *Jpn. J. Appl. Phys.*, **44**, L672 (2005).
16. C. D. REDDY and T. EDLINGTON, "Plasma Density Measurements on COMPASS-C Tokamak from Electron Cyclotron Emission Cutoffs," *Rev. Sci. Instrum.*, **67**, 462 (1996).
17. S. PREISCHE, C. EFTHIMION, and S. M. KAYE, "Oblique Electron Cyclotron Emission for Electron Distribution Studies," *Rev. Sci. Instrum.*, **68**, 409 (1997).
18. T. YAMAMOTO et al., "Electron Temperature and Density Measurements by Harmonic Electron Cyclotron Emission from Doublet-III Tokamak Plasmas," *Phys. Rev. Lett.*, **55**, 1, 83 (1985).
19. A. G. LYNN, P. E. PHILLIPS, and A. HUBBARD, "Electron Cyclotron Emission as a Density Fluctuation Diagnostic," *Rev. Sci. Instrum.*, **75**, 3859 (2004).
20. H. PARK et al., "Recent Advancements in Microwave Imaging Plasma Diagnostics," *Rev. Sci. Instrum.*, **74**, 10, 4239 (2003).
21. H. PARK et al., "Simultaneous Microwave Imaging System for Density and Temperature Measurements on TEXTOR," *Rev. Sci. Instrum.*, **75**, 10, 3787 (2004).
22. A. E. COSTLEY et al., *Phys. Rev. Lett.*, **33**, 758 (1974).
23. R. ENGELMANN and M. CURATOLO, "Cyclotron Radiation from a Rarefied Inhomogeneous Magnetoplasma," *Nucl. Fusion*, **13**, 497 (1973).
24. C. M. CELATA and D. A. BOYD, *Nucl. Fusion*, **17**, 735 (1977).
25. Y. NAGAYAMA et al., "Electron Cyclotron Emission Diagnostics in the Large Helical Device," *J. Plasma Fusion Res.*, **79**, 6, 601 (2003).
26. P. BLANCHARD et al., "Improvement of the  $T_e$  Profile on JET Measured by ECE," *Proc. 15th Conf. High Temperature Plasma Diagnostics*, San Diego, California, 2004.
27. G. BEKEFI, *Radiation Processes in Plasmas*, Wiley, New York (1966).
28. V. S. UDINTSEV, "Electron Temperature Dynamics of TEXTOR Plasmas," Dissertation, University of Utrecht, The Netherlands (2003).
29. W. H. M. CLARK, "The Precision of Electron Cyclotron Emission Measurements from DITE Tokamak," *Plasma Phys.*, **25**, 12, 1501 (1983).
30. M. BORNATICI, R. CANO, O. DE BARBIERI, and F. ENGELMANN, *Nucl. Fusion*, **23**, 1153 (1983).
31. H. HARTFUSS, T. GEIST, and M. HIRSCH, "Heterodyne Methods in Millimetre Wave Plasma Diagnostics with Applications to ECE, Interferometry and Reflectometry," *Plasma Phys. Control Fusion*, **39**, 1693 (1997).
32. E. DE LA LUNA et al., "Impact of Bulk Non-Maxwellian Electrons on Electron Temperature Measurements," *Rev. Sci. Instrum.*, **19**, 193 (2003).
33. M. BORNATICI and U. RUFFINA, "ECE Diagnostic on ITER: A Feasibility Study," *Proc. 10th Joint Workshop Electron Cyclotron Emission and Electron Cyclotron Heating*, Ameland, The Netherlands, 1997.
34. V. KRIVENSKI, "Electron Cyclotron Emission by Non-Maxwellian Bulk Distribution Functions," *Fusion Eng. Des.*, **53**, 23 (2001).
35. T. P. GOODMAN, I. KLIMANOV, A. MUECK, and V. S. UDINTSEV, "First Measurements of Oblique ECE with a Real-Time Movable Line-of-Sight on TCV," *Proc. 14th Joint Workshop Electron Cyclotron Emission and Electron Cyclotron Resonance Heating (EC-14)*, Santorini, Greece, 2006.
36. M. SATO and A. ISAYAMA, "Evaluation of ECE Spectra on the Oblique Propagation and Application to Electron Temperature Measurement in a Reactor Grade Tokamak," *Proc. 14th Joint Workshop Electron Cyclotron Emission and Electron Cyclotron Resonance Heating (EC-14)*, Santorini, Greece, 2006.
37. G. TAYLOR et al., "Electron Cyclotron Emission Measurements on High  $\beta$  TFTR Plasmas," *Proc. 9th Joint Workshop Electron Cyclotron Emission and Electron Cyclotron Heating*, Borrego Springs, California, 1995.
38. E. DE LA LUNA et al., "Recent Developments of ECE Diagnostics at JET," *Proc. 13th Joint Workshop Electron Cyclotron Emission and Electron Cyclotron Resonance Heating (EC-13)*, Nizhny Novgorod, Russia, 2004.
39. E. DE LA LUNA et al., "Diagnosing the Electron Distribution Function with Oblique Electron Cyclotron Emission on FTU," *Proc. 12th Joint Workshop Electron Cyclotron Emission and Electron Cyclotron Resonance Heating*, Aix-en-Provence, France, 2002.
40. C. SOZZI, A. BRUSCHI, A. SIMONETTO, E. DE LA LUNA, J. FESSEY, V. RICCARDO, and JET-EFDA CONTRIBUTORS, "Optical Design of the Oblique-ECE Antenna System for JET," *Proc. 23rd Symp. Fusion Technology*, Fondazione Cini, Venice, Italy, 2004.
41. C. SOZZI, A. BRUSCHI, A. SIMONETTO, E. DE LA LUNA, J. FESSEY, V. RICCARDO, and JET EFDA CONTRIBUTORS, "Optical Design of the Oblique ECE Antenna System for JET," *Fusion Eng. Des.*, **74**, 691 (2005).
42. P. BURATTI and M. ZERBINI, "A Fourier Transform Spectrometer with Fast Scanning Capability for Tokamak Plasma Diagnostics," *Rev. Sci. Instrum.*, **66**, 8, 4208 (1995).

43. E. WESTERHOF, P. SMEULDERS, and N. LOPEZ CARDOZO, "Observations of Sawtooth Postcursor Oscillations in JET and Their Bearing on the Nature of the Sawtooth Collapse," *Nucl. Fusion*, **29**, 6, 1056 (1989).
44. Y. NAGAYAMA et al., "Tomography of Full Sawtooth Crashes on Tokamak Test Fusion Reactor," *Phys. Plasmas*, **3**, 1647 (1996).
45. S. SATTLER and H.J. HARTFUSS, "Intensity Interferometry for Measurement of Electron Temperature Fluctuations in Fusion Plasmas," *Plasma Phys. Control Fusion*, **35**, 1285 (1993).
46. G. CIMA, C. WATTS, and R. F. GANDY, "Correlation Radiometry of Electron-Cyclotron Radiation in TEXT-U," *Rev. Sci. Instrum.*, **66**, 1, 798 (1995).
47. B. H. DENG et al., "ECE Imaging of Plasma  $T_e$  Profiles and Fluctuations," *Fusion Eng. Des.*, **53**, 77 (2001).
48. A. E. COSTLEY, U. GASPARINO, and W. KASPAREK, "Report on the Eighth Joint Workshop on ECE and ECRH (EC'8)," *Nucl. Fusion*, **33**, 8, 1239 (1993).
49. D. A. BOYD, F. SKIFF, and S. GULICK, "A System to Measure Suprathermal Electron Distribution Functions in Toroidal Plasmas by Electron Cyclotron Wave Absorption," *Rev. Sci. Instrum.*, **68**, 496 (1997).
50. J. F. M. VAN GELDER, H. S. MIEDEMA, A. J. H. DONNÉ, A. A. M. OOMENS, and F. C. SCHULLER, *The Electron Cyclotron Absorption Diagnostic at the Rijnhuizen Tokamak Project*, *Rev. Sci. Instrum.*, **68**, 4439 (1997).
51. A. PACHTMAN, S. M. WOLFE, and I. H. HUTCHINSON, *Nucl. Fusion*, **27**, 1283 (1987).
52. N. W. B. STONE, "Expanding Field of Far Infrared Fourier Transform Spectroscopy in the Laboratory, Industry, and the Environment," *Appl. Opt.*, **17**, 9 (1978).
53. D. H. MARTIN and E. PUPLETT, *Infrared Phys.*, **10**, 105 (1970).
54. I. H. HUTCHINSON and D. S. KOMM, *Nucl. Fusion*, **17**, 1077 (1977).
55. B. WALKER, E. A. M. BAKER, and A. E. COSTLEY, "A Fabry-Perot Interferometer for Plasma Diagnostics," *J. Phys. E.*, **14**, 832 (1981).
56. J. CHAMBERLAIN, *The Principles of Interferometric Spectroscopy*, John Wiley & Sons, Chichester, United Kingdom (1979).
57. W. R. RUTGERS and D. A. BOYD, *Phys. Lett.*, **62A**, 498 (1977).
58. G. D. TAIT, F. J. STAUFFER, and D. A. BOYD, *Phys. Fluids*, **24**, 719 (1981).
59. B. J. D. TUBBING et al., in *12th European Physical Society Conf.*, Budapest (1985).
60. P. C. EFTHIMION, V. ARUNASALAM, R. BITZER, L. CAMPBELL, and J. C. HOSEA, "A Fast-Scanning Heterodyne Receiver or Measurement of the Electron Cyclotron Emission for High-Temperature Plasmas," *Rev. Sci. Instrum.*, **50**, 949 (1979).
61. K. KAWAHATA, M. SAKAMOTO, J. FUJITA, H. MATSUO, and K. SAKAI, "Calibration Source for Electron Cyclotron Emission Measurements," *Jpn. J. Appl. Phys.*, **29**, part 1, 9, 1824 (1990).
62. N. ISEI et al., "Electron Cyclotron Emission Measurements in JT-60U," *Fusion Eng. Des.*, **53**, 213 (2001).
63. H. BINDSLEV and D. V. BARTLETT, "A Technique for Improving the Relative Accuracy of JET ECE Temperature Profiles," *Proc. 6th Joint Workshop Electron Cyclotron Emission and Electron Cyclotron Resonance Heating*, Oxford, 1987.
64. H. BINDSLEV and D. V. BARTLETT, "A Technique for Improving the Relative Accuracy of JET ECE Temperature Profiles," Internal JET Report (1988).
65. A. ISAYAMA et al., "A 20-Channel Electron Cyclotron Emission Detection System for a Grating Polychromator in JT-60U," *Rev. Sci. Instrum.*, **73**, 3, 1165 (2002).
66. A. ISAYAMA et al., "Electron Temperature Perturbations Measured by Electron Cyclotron Emission Diagnostic Systems in JT-60U," *Fusion Eng. Des.*, **53**, 129 (2001).
67. S. ISHIDA, A. NAGASHIMA, M. SATO, N. ISEA, and T. MATOBA, "Twenty-Channel Grating Polychromator Diagnostic System for Electron Cyclotron Emission Measurement in JT-60," *Rev. Sci. Instrum.*, **61**, 10, 2834 (1990).
68. M. SATO et al., "Measurements and Analysis of Electron Cyclotron Emission in JT-60U," *Fusion Eng. Des.*, **34-35**, 477 (1997).
69. R. A. OLSTAD, J. L. DOANE, C. P. MOELLER, R. C. O'NEILL, and M. DI MARTINO, "High-Power Corrugated Waveguide Components for mm-Wave Fusion Heating Systems," General Atomics (1996).
70. J. L. DOANE, "Propagation and Mode Coupling in Corrugated and Smooth Walled Circular Waveguides," *Infrared and Millimeter Waves*, K. J. BUTTON, Ed., 1985, Academic Press: New York. p. Chapter 5.
71. M. SATO, N. ISEI, and S. ISHIDA, "Grating Filter for Grating Polychromator on Measurement of Electron Temperature Profile from Second Harmonic Electron Cyclotron Emission," *J. Plasma Fusion Res.*, **71**, 748 (1995).
72. R. WINSTON, "Light Collection Within the Framework of Geometric Optics," *J. Opt. Soc. Am.*, **60**, 245 (1970).
73. M. SATO, H. YOKOMIZO, and A. NAGASHIMA, "Fourier Transform Spectrometer System on JT-60," *J. Plasma Fusion Res. Supplement*, **59**, 47 (1988).
74. A. ISAYAMA, N. IWAMA, T. SHOWA, Y. HOSODA, N. ISEI, S. ISHIDA, and M. SATO, "Maximum Entropy Estimation of Electron Cyclotron Emission Spectra from Incomplete Interferograms in ELMy H-Mode Tokamak Experiment," *Jpn. J. Appl. Phys.*, **42**, 5787 (2003).
75. N. ISEI, M. SATO, S. ISHIDA, K. UCHINO, A. NAGASHIMA, T. MATOBA, and T. OYEVAAR, "Development of 180 GHz Heterodyne Radiometer for Electron Cyclotron Emission Measurements in JT-66U," *Rev. Sci. Instrum.*, **66**, 1, 413 (1995).
76. K. KAWAHATA, T. TANAKA, T. TOKUZAWA, Y. ITO, A. EJIRIL, S. OKAJIMA, and LHD EXPERIMENTAL GROUP, "A Multichannel 118.8 mm-CH<sub>3</sub>OH Laser Interferometer for Electron Density Profile Measurements in LHD," *Proc. 28th European Physical Society Conf. Controlled Fusion and Plasma Physics*, Funchal, Portugal, 2001, ECA.
77. K. KAWAHATA, Y. NAGAYAMA, S. INAGAKI, Y. ITO, and LHD EXPERIMENTAL GROUP, "Broadband Electron Cyclotron Emission Radiometry for the Large Helical Device," *Rev. Sci. Instrum.*, **74**, 3, 1449 (2003).
78. Y. NAGAYAMA et al., "Electron Cyclotron Emission Diagnostics on the Large Helical Device," *Rev. Sci. Instrum.*, **70**, 1, 1021 (1999).
79. V. S. UDINTSEV et al., "New ECE Diagnostics for the TEXTOR-94 Tokamak," *Rev. Sci. Instrum.*, **72**, 1, 359 (2001).
80. V. S. UDINTSEV, R. JASPERS, A.J.H. DONNÉ, A. KRÄMER-FLECKEN, J.W. OOSTERBECK, M. VAN DE POL, and E. WESTERHOF, "Non-Thermal Electrons in TEXTOR-94 Tokamak Plasmas," *Proc. 27th EPS Conf. Controlled Fusion and Plasma Physics*, Budapest, 2000.
81. A. KRAEMER-FLECKEN, G. WAIDMANN, and P. C. DE VRIES, "Measurement of 3rd Harmonic of EC-Radiation at TEXTOR-94," *Proc. 10th Joint Workshop Electron Cyclotron Emission and Electron Cyclotron Resonance Heating*, Singapore, 1997, World Scientific.
82. J. F. M. VAN GELDER et al., "Heterodyne Radiometer at Rijnhuizen Tokamak Project for Electron Cyclotron Emission and Absorption Measurements," *Rev. Sci. Instrum.*, **66**, 1, 416 (1995).

83. K. EBISAWA et al., "Plasma Diagnostics for Inter-FEAT," *Rev. Sci. Instrum.*, **72**, 1, 545 (2001).
84. A. E. COSTLEY, A. MALAQUIAS, T. SUGIE, G. VAYAKIS, and C. WALKER, "ITER Diagnostics: Design Choices and Solutions," IAEA (2002).
85. G. VAYAKIS et al., "Reflectometry on ITER," *Rev. Sci. Instrum.*, **68**, 435 (1997).
86. H. HARTFUSS, "Diagnostics for Experimental Thermonuclear Fusion Reactors," *Proc. Int. Workshop Diagnostics for ITER*, Varenna, Italy, 1995, Plenum Press.
87. ITER, "ITER Physics Group: ITER Physics Basis Editors, and ITER EDA, Chapter 7: Measurement of Plasma Parameters," *Nucl. Fusion*, **39**, 12, 2541 (1999).
88. J. Y. L. MA and L. C. ROBINSON, "Night Moth Eye Window for the Millimetre and Sub-Millimetre Wave Region," *J. Mod. Opt.*, **30**, 12, 1685 (1983).
89. A. J. H. DONNÉ and A. E. COSTLEY, "Key Issues in Diagnostics for Burning Plasma Experiments," *IEEE Trans. Plasma Sci.*, **32**, 1, 177 (2004).
90. G. VAYAKIS et al., "ECE Diagnostics for RTO/RC-FEAT," *Fusion Eng. Des.*, **53**, 221 (2001).
91. D. V. BARTLETT et al., in *Proc. 14th European Conf. Controlled Fusion and Plasma Physics*, Madrid, Spain, 1987.
92. I. B. BERNSTEIN, "Waves in a Plasma in a Magnetic Field," *Phys. Rev.*, **109**, 10 (1958).
93. A. K. RAM and S. D. SCHULTZ, "Excitation, Propagation, and Damping of Electron Bernstein Waves in Tokamaks," *Phys. Plasmas*, **7**, 4084 (2000).
94. J. PREINHAELTER and V. KOPÉCKY, "Penetration of High-Frequency Waves into a Weakly Inhomogeneous Magnetized Plasma at Oblique Incidence and Their Transformation to Bernstein Modes," *J. Plasma Phys.*, **10**, 1 (1973).
95. H. P. LAQUA, H. J. HARTFUSS, and W7-AS TEAM, "Electron Bernstein Wave Emission from an Overdense Plasma at the W7-AS Stellarator," *Phys. Rev. Lett.*, **81**, 2060 (1998).
96. F. VOLPE and H. P. LAQUA, "BXO Mode-Converted Electron Bernstein Emission Diagnostic," *Rev. Sci. Instrum.*, **74**, 1409 (2003).
97. V. SHEVCHENKO et al., "Electron Bernstein Wave Studies on Compass-D and MAST," *AIP Conf. Proc.*, **694**, 359 (2003).
98. J. PREINHAELTER et al., "Influence of Antenna Aiming on ECE in MAST," *Rev. Sci. Instrum.*, **75**, 3804 (2004).
99. G. TAYLOR et al., "Efficient Coupling of Thermal Electron Bernstein Waves to the Ordinary Electromagnetic Mode on the National Spherical Torus Experiment," *Phys. Plasmas*, **12**, 052511 (2005).
100. J. PREINHAELTER et al., "EBW Simulation for MAST and NSTX Experiments," *AIP Conf. Proc.*, **787**, 349 (2005).
101. V. SHEVCHENKO et al., "EBW Emission Observations on Compass-D and MAST," *Proc. 28th EPS Conf. Controlled Fusion and Plasma Physics*, ECA, Vol. 25A, p. 1285 (2001).
102. P. K. CHATTOPADHYAY et al., "Electron Bernstein Wave Emission from an Overdense Reversed Field Pinch Plasma," *Phys. Plasmas*, **9**, 752 (2002).
103. B. JONES et al., "Controlled Optimization of Mode Conversion from Electron Bernstein Waves to Extraordinary Mode in Magnetized Plasma," *Phys. Rev. Lett.*, **90**, 165001 (2003).
104. T. MUNSAT et al., "Transient Transport Experiments in the Current-Drive Experiment Upgrade Spherical Torus," *Phys. Plasmas*, **9**, 480 (2002).
105. B. JONES, G. TAYLOR, P. C. EFTHIMION, and T. MUNSAT, "Measurement of the Magnetic Field in a Spherical Torus Plasma via Electron Bernstein Wave Emission Harmonic Overlap," *Phys. Plasmas*, **11**, 1028 (2004).
106. G. TAYLOR et al., "Enhanced Conversion of Thermal Electron Bernstein Waves to the Extraordinary Electromagnetic Mode on the National Spherical Torus Experiment," *Phys. Plasmas*, **10**, 1395 (2003).
107. S. SHIRAIWA et al., "Electron Bernstein Wave Emission Diagnostic Assisted by Reflectometry on TST-2 Spherical Tokamak," *Rev. Sci. Instrum.*, **74**, 3, 1453 (2003).
108. K. G. BUDDEN, *Radio Waves in the Ionosphere: The Mathematical Theory of the Reflection of Radio Waves from Stratified Ionised Layers*, Cambridge University Press, London (1961).
109. V. L. GINZBURG, *Propagation of Electromagnetic Waves in Plasmas*, Gordon and Breach, New York (1961).
110. F. SIMONET, "Measurement of Electron Density Profile by Microwave Reflectometry on Tokamak," *Rev. Sci. Instrum.*, **56**, 664 (1985).
111. H. BOTTOLLIER-CURTET and G. ICHTCHENCKO, "Determination of the Electron Density Profile of Petula-B," *Rev. Sci. Instrum.*, **58**, 539 (1987).
112. A. E. HUBBARD, A. E. COSTLEY, and C. W. GOWERS, "A Simple Fixed-Frequency Reflectometer for Plasma Density Profile Measurements on JET," *J. Phys. E.*, **20**, 423 (1987).
113. E. MAZZUCATO, "Microwave Reflectometry for Magnetically Confined Plasmas," *Rev. Sci. Instrum.*, **69**, 2201 (1998).
114. H. BINDSLEV, *Plasma Phys. Control Fusion*, **35**, 1093 (1993).
115. C. LAVIRON, A. J. H. DONNÉ, M. E. MANSO, and J. SANCHEZ, "Reflectometry Techniques for Density Profile Measurements on Fusion Plasmas," *Plasma Phys. Control Fusion*, **38**, 905 (1996).
116. P. VARELA et al., "Initialization of Plasma Density Profiles from Reflectometry," *Rev. Sci. Instrum.*, **66**, 4942 (1995).
117. V. ZHURAVLEV, J. SANCHEZ, and E. DE LA LUNA, "Two-Dimensional Effects of Turbulence in Density Profile Measurements by Reflectometry," *Plasma Phys. Control Fusion*, **38**, 2231 (1996).
118. L. G. BRUSKIN, A. MASE, T. TAMANO, and K. YATSU, "Application of One-Dimensional Wentzel-Kramers-Brillouin Approximation in Microwave Reflectometry of Plasma Density Profiles," *Rev. Sci. Instrum.*, **69**, 2184 (1998).
119. A. SILVA et al., "Performance of the Microwave Reflectometry Diagnostic for Density Profile Measurements on ASDEX Upgrade," *Rev. Sci. Instrum.*, **72**, 307 (2001).
120. G. WANG, L. ZENG, E. J. DOYLE, T. L. RHODES, and W. A. PEEBLES, "Improved Reflectometer Electron Density Profile Measurements on DIII-D," *Rev. Sci. Instrum.*, **74**, 1525 (2003).
121. K. W. KIM, E. DOYLE, W. A. PEEBLES, A. EJIRIL, N. C. LUHMANN, Jr., and C. L. RETTIG, "Advances in Reflectometric Density Profile Measurements on the DIII-D Tokamak," *Rev. Sci. Instrum.*, **66**, 2, 1229 (1995).
122. K. W. KIM, E. DOYLE, T. L. RHODES, W. A. PEEBLES, C. RETTIG, and N. C. LUHMANN, Jr., "Development of a Fast Solid-State High Resolution Density Profile Reflectometer System on the DIII-D Tokamak," *Rev. Sci. Instrum.*, **68**, 1, 466 (1997).
123. G. CUNNINGHAM, T. EDLINGTON, A. SILVA, and L. MENESES, "Profile Reflectometry on MAST," *Proc. 7th Int. Reflectometry Workshop Fusion Plasma Diagnostics (IRW7)*, Garching, Germany, 2005.
124. L. MENESES, L. CUPIDO, A. A. FERREIRA, S. HACQUIN, M. MANSO, and JET EFDA CONTRIBUTORS, "New Reflectometer Design for Density Profile Measurements on JET," *Rev. Sci. Instrum.*, **77** (2006).



125. Y. LIN et al., "Upgrade of Reflectometry Profile and Fluctuation Measurements in Alcator C-Mod," *Rev. Sci. Instrum.*, **70**, 1078 (1999).
126. T. ESTRADA et al., "Density Profile Measurements by AM Reflectometry in TJ-II," *Plasma Phys. Control Fusion*, **43**, 1535 (2001).
127. T. ESTRADA, J. SÁNCHEZ, V. ZHURAVLEV, E. DE LALUNA, and BRAÑAS, "Turbulence and Beam Size Effects on Reflectometry Measurements," *Phys. Plasmas*, **8**, 6, 2657 (2001).
128. G. R. HANSON et al., "Differential-Phase Reflectometry for Edge Profile Measurements on Tokamak Fusion Test Reader," *Rev. Sci. Instrum.*, **66**, 1, part 2, 863 (1995).
129. G. R. HANSON et al., "Microwave Reflectometry for Edge Density Profile Measurements on TFTR," *Plasma Phys. Control Fusion*, **36**, 12, 2073 (1994).
130. C. A. J. HUGENHOLTZ et al., "Pulsed Radar Reflectometry for the Textor Tokamak," *Rev. Sci. Instrum.*, **70**, 1034 (1999).
131. C. W. DOMIER, N. C. LUHMANN, Jr., A. E. CHOU, W.-M. ZHANG, and A. J. ROMANOWSKY, "Ultrashort-Pulse Reflectometry," *Rev. Sci. Instrum.*, **66**, 1, 399 (1995).
132. B. I. COHEN, L. L. LODESTRO, E. BICKFORD, and T. A. CASPER, "Simulations of Broadband Short-Pulse Reflectometry for Diagnosing Plasma Density and Magnetic-Field Profiles," *Plasma Phys. Control Fusion*, **40**(PII), 75 (1998).
133. Y. ROH, C. W. DOMIER, and N. C. LUHMANN, Jr., "Ultrashort Pulse Reflectometry for Density Profile and Fluctuation Measurements on SSPX," *Rev. Sci. Instrum.*, **74**, 3, 1518 (2003).
134. Y. KOGI et al., "Ultrashort-Pulse Reflectometer on LHD," *Rev. Sci. Instrum.*, **75**, 3837 (2004).
135. T. TOKUZAWA, K. KAWAHATA, T. TANAKA, and LHD EXPERIMENTAL GROUP, "Electron Density Profile Measurement Using Ka-Band Microwave Impulse Radar Reflectometer on LHD," *Nucl. Fusion*, **46**, S670 (2006).
136. C. W. DOMIER, N. C. LUHMANN, Jr., Y. ROH, H. S. MCLEAN, E. B. HOOPER, and D. N. HILL, "Ultrashort Pulse Reflectometer Performance on the Sustained Spheromak Physics Experiment," *Rev. Sci. Instrum.*, **75**, 10, 3868 (2004).
137. A. MASE et al., "Remote Experiment of Ultrashort-Pulse Reflectometry for Large Helical Device Plasmas," *Rev. Sci. Instrum.*, **77**, 10E916 (2006).
138. P. VARELA, M. MANSO, A. SILVA, CFN TEAM, and ASDEX UPGRADE TEAM, "Review of Data Processing Techniques for Density Profile Evaluation from Broadband FM-CW Reflectometry on ASDEX Upgrade," *Nucl. Fusion*, **46**, S693 (2006).
139. I. NUNES et al., "Characterization of the Density Profile Collapse of Type I ELMs in ASDEX Upgrade with High Temporal and Spatial Resolution Reflectometry," *Nucl. Fusion*, **44**, 883 (2004).
140. B. P. VAN MILLIGEN et al., "Ballistic Transport Phenomena in TJ-II," *Nucl. Fusion*, **42**, 787 (2002).
141. J. SANTOS, M. MANSO, VARELA, and J. NEUHAUSER, "Plasma Position Measurements From Ordinary FM-CW Reflectometry on ASDEX Upgrade," *Rev. Sci. Instrum.*, **74**, 1489 (2003).
142. L. ZHENG, E. J. DOYLE, T. C. LUCE, and W. A. PEEBLES, "Implementation of Reflectometry as a Standard Density Profile Diagnostic on DIII-D," *Rev. Sci. Instrum.*, **72**, 320 (2001).
143. F. WAGNER et al., *Plasma Phys. Control Fusion*, **36**, A-61 (1994).
144. M. MANSO et al., "H-Mode Studies with Microwave Reflectometry on ASDEX Upgrade," *Plasma Phys. Control Fusion*, **40**, 747 (1998).
145. T. L. RHODES et al., "Comparison of Turbulence Measurements from DIII-D Low-Mode and High-Performance Plasmas to Turbulence Simulations and Models," *Phys. Plasmas*, **9**, 5, 2141 (2002).
146. N. OYAMA and K. SHINOHARA, "Heterodyne O-Mode Reflectometer on the JT-60U Tokamak," *Rev. Sci. Instrum.*, **73**, 1169 (2002).
147. R. NAZIKIAN, G. J. KRAMER, and E. VALEO, "A Tutorial on the Basic Principles of Microwave Reflectometry Applied to Fluctuation Measurements in Fusion Plasmas," *Phys. Plasmas*, **8**, 1840 (2001).
148. B. B. AFEYANT, A. CHOU, and B. I. COHEN, "The Scattering Phase Shift due to Bragg Resonance in One-Dimensional Fluctuation Reflectometry," *Plasma Phys. Control Fusion*, **37**, 315 (1995).
149. N. L. BRETZ, "One-Dimensional Modeling of the Wavelength Sensitivity, Localization, Measurements of Plasma Fluctuations," *Phys. Fluids*, **B4**, 2414 (1992).
150. J. SANCHEZ, T. ESTRADA, and H. J. HARTFUSS, "Broadband Heterodyne Reflectometry: Application to W7AS," *Proc. 1st IAEA Technical Committee Mtg. Microwave Reflectometry on Fusion Plasma Diagnostics*, Abingdon, 1992.
151. V. V. BULANIN and D. KORNEEV, "Tokamak Plasma Cross-Detection Reflectometry," *Plasma Phys. Rep.*, **2**, 014 (1994).
152. T. L. RHODES, R. J. TAYLOR, E. J. DOYLE, N. C. J. LUHMANN, and W. A. PEEBLES, "Poloidally Asymmetric Response of Turbulence to the H-Mode on the CCT Tokamak," *Nucl. Fusion*, **12**, 1787 (1993).
153. E. MAZZUCATO and R. NAZIKIAN, "Radial Scale Length of Turbulent Fluctuations in the Main Core of TFTR Plasmas," *Phys. Rev. Lett.*, **71**, 1840 (1993).
154. G. D. CONWAY, "2D Modelling of Radial Correlation Reflectometry," *Plasma Phys. Control Fusion*, **39**, 407 (1997).
155. Y. LIN, R. NAZIKIAN, H. IRBY, and E. S. MARMAR, "Plasma Curvature Effects on Microwave Reflectometry Fluctuation Measurements," *Plasma Phys. Control Fusion*, **43**, L1 (2001).
156. J. H. IRBY, S. HORNE, I. H. HUTCHINSON, and P. C. STEK, "2D Full-Wave Simulation of Ordinary Mode Reflectometry," *Plasma Phys. Control Fusion*, **35**, 601 (1993).
157. E. Z. GUSAKOV and B. O. YAKOVLEV, "Two-Dimensional Linear Theory of Radial Correlation Reflectometry Diagnostics," *Plasma Phys. Control Fusion*, **44**, 2525 (2002).
158. E. Z. GUSAKOV and A. Y. POPOV, "Two-Dimensional Non-Linear Theory of Radial Correlation Reflectometry," *Plasma Phys. Control Fusion*, **46**, 1393 (2004).
159. L. G. BRUSKIN et al., "Application of a Stratified Plasma Model to Microwave Reflectometry of Density Fluctuations," *Plasma Phys. Control Fusion*, **47**, 1379 (2005).
160. M. HIRSCH et al., "Doppler Reflectometry for the Investigation of Propagating Density Perturbations," *Plasma Phys. Control Fusion*, **43**, 1641 (2001).
161. E. HOLZHAUER, M. HIRSCH, T. GROSSMANN, B. BAÑAS, and F. SERRA, "Theoretical and Experimental Investigation of the Phase-Runaway in Microwave Reflectometry," *Plasma Phys. Control Fusion*, **40**, 1869 (1998).
162. G. D. CONWAY, J. SCHIRMER, S. KLENGE, W. SUTTROP, E. HOLZHAUER, and ASDEX UPGRADE TEAM, "Plasma Rotation Profile Measurements Using Doppler Reflectometry," *Plasma Phys. Control Fusion*, **46**, 951 (2004).

163. E. BLANCO, T. ESTRADA, and J. SANCHEZ, "Doppler Reflectometry Studies Using a Two-Dimensional Full-Wave Code," *Plasma Phys. Control Fusion*, **48**, 699 (2006).
164. E. Z. GUSAKOV and A. V. SURKOV, "Spatial and Wavenumber Resolution of Doppler Reflectometry," *Plasma Phys. Control Fusion*, **46**, 1143 (2004).
165. A. V. SURKOV, "Nonlinear Regime of Doppler Reflectometry in Cylindrical Plasmas," *Plasma Phys. Control Fusion*, **48**, 901 (2006).
166. M. HIRSCH and E. HOLZHAUER, "Doppler Reflectometry with Optimized Temporal Resolution for the Measurement of Turbulence and Its Propagation Velocity," *Plasma Phys. Control Fusion*, **46**, 593 (2004).
167. M. HIRSCH, J. BALDZHUN, H. EHMLER, E. HOLZHAUER, and F. WAGNER, "Dynamics of Poloidal Flows and Turbulence at the H-Mode Transition in W7-AS," *Plasma Phys. Control Fusion*, **48**, S155 (2006).
168. V. V. BULANIN et al., "Plasma Rotation Evolution Near the Peripheral Transport Barrier in the Presence of Low-Frequency MHD Bursts in TUMAN-3M Tokamak," *Plasma Phys. Control Fusion*, **48**, A101 (2006).
169. P. HENNEQUIN, C. HONORÉ, A. TRUC, A. QUÉMENÉUR, and N. LEMOINE, "Doppler Backscattering System for Measuring Fluctuations and Their Perpendicular Velocity in Tore Supra," *Rev. Sci. Instrum.*, **75**, 3881 (2004).
170. T. ESTRADA, E. BLANCO, L. CUPIDO, M. MANSO, and J. SANCHEZ, "Velocity Shear Layer Measurements by Reflectometry in TJ-II Plasmas," *Nucl. Fusion*, **46**, S792 (2006).
171. G. VAYAKIS et al., "Status and Plans for Reflectometry in ITER," *Proc. 7th Int. Reflectometry Workshop for Fusion Plasma Diagnostics (IRW-7)*, Garching, Germany, 2005.
172. J. SHEFFIELD, *Plasma Scattering of Electromagnetic Radiation*, Academic Press (1975).
173. H. BINDSLEV, *Recent Developments in Theory of Wave Scattering in Plasmas*, p. 109, A. G. LITVAK, Ed., Russian Academy of Sciences, Institute of Applied Physics, Nizhny Novgorod, Russia (1996).
174. H. BINDSLEV, *J. Atmos. Terr. Phys.*, **58**, 983 (1996).
175. E. HOLZHAUER and J. H. MASSIG, "An Analysis of Optical Mixing in Plasma Scattering Experiments," *Plasma Phys.*, **20**, 867 (1978).
176. D. GRESILLON, C. STERN, A. HEMON, A. TRUC, and T. LEHNER, "Density Fluctuation Measurement by Far Infrared Light Scattering," *Physica Scripta*, **T2/2**, 459 (1982).
177. R. E. SLUSHER and C. M. SURKO, "Study of Density Fluctuations in Plasmas by Small-Angle CO<sub>2</sub> Laser Scattering," *Phys. Fluids*, **23**, 472 (1980).
178. T. TSUKISHIMA, "Measurements of the Density Fluctuations Using Microwave Scattering Method," *Diagnostics for Fusion Experiments*, p. 225, E. SINDONI and C. WHARTON, Eds., Pergamon Press, Oxford and New York (1979).
179. A. E. SIEGMAN, "The Antenna Properties of Optical Heterodyne Receivers," *Appl. Opt.*, **5**, 1588 (1966).
180. J. BROWN, *Proc. IEE*, **105C**, 343 (1958).
181. M. MORESCO and E. ZILLI, "Coherent Scattering Theory with Gaussian Beams in Plasma Diagnostics," *J. Phys. D.*, **17**, 307 (1984).
182. N. L. BRETZ, P. EFTHIMION, J. DOANE, and A. KRITZ, "X-Mode Scattering for the Measurement of Density Fluctuations on TFTR," *Rev. Sci. Instrum.*, **59**, 1539 (1988).
183. J. P. DOUGHERTY and D. T. FARLEY, "A Theory of Incoherent Scattering of Radio Waves By a Plasma," *Proc. R. Soc. London*, **A259**, 79 (1960).
184. A. G. SITENKO, *Electromagnetic Fluctuations in Plasma*, Academic Press, New York (1967).
185. D. M. SIMONICH and K. C. YEH, "A Theory of Scattering from Irregularities in a Magneto-Ionic Medium," *Radio Sci.*, **7**, 291 (1972).
186. N. L. BRETZ, "Geometrical Effects in X-Mode Scattering," *J. Plasma Phys.*, **38**, 79 (1987).
187. T. P. HUGHES and S. R. P. SMITH, "Effects of Plasma Dielectric Properties on Thomson Scattering of Millimetre Waves in Tokamak Plasmas," *J. Plasma Phys.*, **42**, 215 (1989).
188. A. TRUC et al., "ALTAIR: An Infrared Laser Scattering Diagnostic on the TORE SUPRA Tokamak," *Rev. Sci. Instrum.*, **63**, 3716 (1992).
189. P. DEVYNCK et al., "Localized Measurements of Turbulence in the TORE SUPRA Tokamak," *Plasma Phys. Control Fusion*, **35**, 63 (1993).
190. C. L. RETTIG, E. J. DOYLE, W. A. PEEBLES, K. H. BURRELL, R. J. GROEBNER, T. H. OSBORNE, and N. C. LUHMANN, Jr., "Enhanced Spatial Localization of Collective Scattering Measurements in the DIII-D Tokamak," *Rev. Sci. Instrum.*, **66**, 848 (1995).
191. C. L. RETTIG, W. A. PEEBLES, K. H. BURRELL, E. J. DOYLE, R. J. GROEBNER, N. C. LUHMANN, Jr., and R. PHILIPONA, "Edge Turbulence Reduction at the L-H Transition in DIII-D," *Nucl. Fusion*, **33**, 643 (1993).
192. C. L. RETTIG, W. A. PEEBLES, K. H. BURRELL, R. J. LA HAYE, E. J. DOYLE, R. J. GROEBNER, and N. C. LUHMANN, Jr., "Microturbulence Damping Mechanisms in the DIII-D Tokamak," *Phys. Fluids*, **B5**, 2428 (1993).
193. E. MAZZUCATO, "Localized Measurement of Turbulent Fluctuations in Tokamaks with Coherent Scattering of Electromagnetic Waves," *Phys. Plasmas*, **10**, 753 (2003).
194. D. R. SMITH et al., "Microwave Scattering System Design for  $\rho_e$  Scale Turbulence Measurements on NSTX," *Rev. Sci. Instrum.*, **75**, 3840 (2004).
195. D. R. SMITH et al., "Investigation of Electron Gyroscale Fluctuations on NSTX with a Millimeter-Wave Scattering System," *Proc. 16th High Temperature Plasma Diagnostics Conf.* Williamsburg, Virginia, 2006.
196. J. L. DOANE, "Broadband Superheterodyne Tracking Circuits for Millimeter-Wave Measurements," *Rev. Sci. Instrum.*, **51**, 317 (1980).
197. C. L. RETTIG, S. BURNS, R. PHILIPONA, W. A. PEEBLES, and N. C. LUHMANN, Jr., "Development and Operation of a Backward Wave Oscillator Based FIR Scattering System for DIII-D," *Rev. Sci. Instrum.*, **61**, 3010 (1990).
198. T. TSUKISHIMA and O. ASADA, "A Homodyne Method for Detecting Asymmetric Spectra in Electromagnetic Wave Scatterings from Plasmas," *Jpn. J. Appl. Phys.*, **17**, 2059 (1978).
199. O. ASADA, A. INOUE, and T. TSUKISHIMA, "Homodyne Method for Detecting Asymmetric Spectra," *Rev. Sci. Instrum.*, **51**, 1308 (1980).
200. D. L. BROWER, C. P. RITZ, W. A. PEEBLES, N. C. LUHMANN, Jr., and E. J. POWERS, "The Application of Homodyne Spectroscopy to the Study of Low-Frequency Microturbulence in the TEXT Tokamak," *Int. J. Infrared Millimeter Waves*, **7**, 447 (1986).
201. E. MAZZUCATO, "Small-Scale Density Fluctuations in the Adiabatic Toroidal Compressor," *Phys. Rev. Lett.*, **36**, 792 (1976).

202. R. J. GOLDSTON, E. MAZZUCATO, R. E. SLUSHER, and C. M. SURKO, "Plasma Physics and Controlled Nuclear Fusion Research," *Proc. 6th Int. Conf. Plasma Physics and Controlled Nuclear Fusion Research*, Vienna, Austria, 1977, IAEA.
203. E. MAZZUCATO, "Low-Frequency Microinstabilities in the PLT Tokamak," *Phys. Fluids*, **21**, 1063 (1978).
204. E. MAZZUCATO, "Spectrum of Small-Scale Density Fluctuations in Tokamaks," *Phys. Rev. Lett.*, **48**, 1828 (1982).
205. C. M. SURKO and R. E. SLUSHER, "Study of the Density Fluctuations in the Adiabatic Toroidal Compressor Tokamak Using CO<sub>2</sub> Laser Scattering," *Phys. Rev. Lett.*, **37**, 1747 (1976).
206. R. CANO, "A Review of Microwave Scattering on Toroidal Plasma," *Diagnostics for Fusion Experiments*, p. 177, E. S. A. C. WHARTON, Ed., Pergamon Press, Oxford (1978).
207. N. C. LUHMANN, Jr. and W. A. PEEBLES, "Laser Diagnostics of Magnetically Confined Thermonuclear Plasmas," *Laser Handbook*, p. 455, M. B. A. M. L. STITCH, Ed., Elsevier Science Publisher B.V. (1985).
208. D. L. BROWER, H. K. PARK, W. A. PEEBLES, and N. C. LUHMANN, Jr., "Multichannel Far-Infrared Collective Scattering System for Plasma Wave Studies," *Topics in Millimeter Wave Technology*, p. 83, K. J. BUTTON, Ed., Academic Press, New York (1988).
209. N. C. LUHMANN, Jr. et al., "Millimeter and Submillimeter Wave Diagnostic Systems for Contemporary Fusion Experiments," *Diagnostics for Contemporary Fusion Experiments*, p. 135, P. E. STOTT, G. GORINI, and E. SINDONI, Eds., SIF, Bologna (1991).
210. N. L. BRETZ, "Instrumentation for Microturbulence in Tokamaks," *Rev. Sci. Instrum.*, **68**, 2927 (1997).
211. P. C. LIEWER, "Measurements of Microturbulence in Tokamaks and Comparisons with Theories of Turbulence and Anomalous Transport," *Nucl. Fusion*, **25**, 543 (1985).
212. A. J. WOOTTON et al., "Fluctuations and Anomalous Transport in Tokamaks," *Phys. Fluids*, **B2**, 2879 (1990).
213. D. L. BROWER, W. A. PEEBLES, N. C. LUHMANN, Jr., and R. L. SAVAGE, "Multichannel Scattering Studies of the Spectra and Spatial Distribution of Tokamak Microturbulence," *Phys. Rev. Lett.*, **54**, 689 (1985).
214. D. L. BROWER, W. A. PEEBLES, and N. C. LUHMANN, Jr., "The Spectrum, Spatial Distribution and Scaling of Microturbulence in the TEXT Tokamak," *Nucl. Fusion*, **27**, 2055 (1987).
215. D. L. BROWER, W. A. PEEBLES, and N. C. LUHMANN, Jr., "Observation of Large-Amplitude, Narrow-Band Density Fluctuations in the Interior Region of an Ohmic Tokamak Plasma," *Phys. Rev. Lett.*, **55**, 2579 (1985).
216. D. L. BROWER, W. A. PEEBLES, S. K. KIM, N. C. LUHMANN, Jr., W. M. TANG, and P. E. PHILLIPS, "Observation of a High-Density Ion Mode on Tokamak Microturbulence," *Phys. Rev. Lett.*, **59**, 48 (1987).
217. D. L. BROWER et al., "Experimental Evidence for Ion Pressure Gradient Driven Turbulence in TEXT," *Nucl. Fusion*, **29**, 1247 (1989).
218. D. L. BROWER et al., "Experimental Evidence for Coupling of Plasma Particle and Heat Transport in the TEXT Tokamak," *Phys. Rev. Lett.*, **65**, 337 (1990).
219. D. L. BROWER et al., "Confinement Degradation and Enhanced Microturbulence as Long-Time Precursors to High-Density-Limit Tokamak Disruptions," *Phys. Rev. Lett.*, **67**, 200 (1991).
220. C. X. YU et al., "Comparison of the Density Fluctuation Spectrum and Amplitude in TEXT with Expectation for Electron Drift Waves," *Phys. Fluids*, **b4**, 381 (1992).
221. C. X. YU et al., "Tearing Instabilities and Microturbulence in TEXT," *Nucl. Fusion*, **32**, 1545 (1992).
222. R. PHILIPONA et al., "Far-Infrared Heterodyne Scattering to Study Density Fluctuations on the DIII-D Tokamak," *Rev. Sci. Instrum.*, **61**, 3007 (1990).
223. T. L. RHODES et al., "Comparison of Broad Spectrum Turbulence Measurements and Gyrokinetic Code Prediction on the DIII-D Tokamak," *Proc. 20th IAEA Fusion Energy Conf.*, Vilmoura, Portugal, 2004, IAEA.
224. N. L. BRETZ, R. NAZIKIAN, W. BERGIN, M. DIESSO, J. FEIT, and M. MCCARTHY, "Instrumental Aspects of Extraordinary Mode Scattering on TFTR," *Rev. Sci. Instrum.*, **61**, 3031 (1990).
225. K. L. WONG, N. L. BRETZ, T. S. HAHM, and E. SYNKOWSKI, "Short Wavelength Fluctuations and Electron Heat Conductivity in Enhanced Reversed Shear Plasmas," *Phys. Lett.*, **A236**, 339 (1997).
226. D. E. EVANS, M. VON HELLERMANN, and E. HOLZHAUER, "Fourier Optics Approach to Far Forward Scattering and Related Refractive Index Phenomena in Laboratory Plasmas," *Plasma Phys.*, **24**, 819 (1982).
227. W. R. KLEIN and B. D. COOK, "Unified Approach to Ultrasonic Light Diffraction," *IEEE Trans. Sonics Ultrasonics*, **SU-14**, 123 (1967).
228. D. E. EVANS, E. J. DOYLE, D. FRIGIONE, M. VON HELLERMANN, and A. MURDOCH, "Measurement of Long Wavelength Turbulence in a Tokamak by Extreme Far Forward Scattering," *Plasma Phys.*, **25**, 617 (1983).
229. H. W. H. VAN ANDEL, A. BOILEAU, and M. VON HELLERMANN, "Study of Microturbulence in the TEXTOR Tokamak Using CO<sub>2</sub> Laser Scattering," *Plasma Phys. Control Fusion*, **29**, 49 (1987).
230. K. MATSUO, H. NITTA, Y. SONODA, K. MURAOKA, M. AKAZAKI, and RFC-XX-M GROUP, "Identification and Role of Low-Frequency Microinstability in RFC-XX-M Studied by the Fraunhofer-Diffraction Method," *J. Phys. Soc. Jpn.*, **56**, 150 (1987).
231. C. X. YU, J. X. CAO, X. M. SHEN, and Z. S. WANG, "Diffraction of Electromagnetic Wave by a Damped Plasma Wave," *Plasma Phys. Control Fusion*, **30**, 1821 (1988).
232. A. R. THOMPSON, J. M. MORAN, and G. W. SWENSON, Jr., *Interferometry and Synthesis in Radio Astronomy*, Wiley and Sons, New York (1986).
233. L. E. SHARP, "The Measurement of Large-Scale Density Fluctuations in Toroidal Plasmas from the Phase Scintillation of a Probing Electromagnetic Wave," *Plasma Phys.*, **25**, 781 (1983).
234. R. NAZIKIAN and L. E. SHARP, "CO<sub>2</sub> Laser Scintillation Interferometer for the Measurement of Density Fluctuations in Plasma Confinement Devices," *Rev. Sci. Instrum.*, **58**, 2086 (1987).
235. B. W. JAMES and C. X. YU, "Diffraction of Laser Radiation by a Plasma Wave—The Near Field and Far Field Limiting Cases," *Plasma Phys.*, **27**, 557 (1985).
236. J. HOWARD and L. E. SHARP, "Diffraction Analysis of Forward-Angle Scattering in Plasmas," *Plasma Phys. Control Fusion*, **34**, 1133 (1992).
237. H. WEISEN, "Imaging Methods for the Observation of Plasma Density Fluctuations," *Plasma Phys. Control Fusion*, **28**, 1147 (1986).
238. H. WEISEN, C. HOLLENSTEIN, and R. BEHN, "Turbulent Density Fluctuations in the TCA Tokamak," *Plasma Phys. Control Fusion*, **30**, 309 (1988).
239. H. WEISEN, "The Phase Contrast Method as an Imaging Diagnostic for Plasma Density Fluctuations," *Rev. Sci. Instrum.*, **59**, 1544 (1988).

240. A. D. PILIYA, *Phys. Tech. Phys.*, **11**, 1680 (1966).
241. K. M. NOVIK and A. D. PILIYA, "Enhanced Microwave Scattering in Plasmas," *Plasma Phys. Control Fusion*, **36**, 357 (1993).
242. I. FIDONE, "Enhanced Incoherent Scattering at the Upper-Hybrid Resonance. I. Cold Plasma Theory," *Phys. Fluids*, **16**, 1680 (1973).
243. I. FIDONE and G. GRANATA, "Enhanced Incoherent Scattering at the Upper-Hybrid Resonance. II. Warm Plasma Theory," *Phys. Fluids*, **16**, 1685 (1973).
244. E. Z. GUSAKOV and A. D. PILIYA, "The Possibility of Determining the Spatial Spectrum of Plasma Oscillations by the Method of Enhanced Scattering of Microwave," *Sov. Tech. Phys. Lett.*, **18**, 325 (1992).
245. B. BRUSEHABER, E. Z. GUSAKOV, M. KRAMER, and A. D. PILIYA, "Enhanced Microwave Scattering with Time-Flight Resolution," *Plasma Phys. Control Fusion*, **36**, 997 (1994).
246. B. BRUSEHABER and M. KRAMER, "Enhanced Microwave Pulse Backscattering off Externally Excited Low-Hybrid Waves," *Plasma Phys. Control Fusion*, **37**, 497 (1995).
247. B. BRUSEHABER and M. KRAMER, "Study of RADAR-Enhanced Scattering on a Magnetized RF Discharge," *Plasma Phys. Control Fusion*, **39**, 389 (1997).
248. D. G. BULYGINSKIY et al., "RADAR Upper Hybrid Resonance Scattering Diagnostics of Small-Scale Fluctuations and Waves in Tokamak Plasmas," *Phys. Plasmas*, **8**, 2224 (2001).
249. A. D. GURCHENKO, E. Z. GUSAKOV, M. M. LARIONOV, K. M. NOVIK, A. N. SAVEL'EV, V. L. SELENIN, and A. Y. STEPANOV, "Spectra of Enhanced Scattering by Spontaneous Density Fluctuations in a Tokamak," *Plasma Phys.*, **30**, 807 (2004).
250. V. I. ARKHIPENKO, V. N. BUDNIKOV, E. Z. GUSAKOV, V. L. SELENIN, and L. V. SIMONCHIK, "Measurement of the Wavelength of Plasma Fluctuations by the Correlation Enhanced Scattering Method," *Tech. Phys. Lett.*, **19**, 20 (1993).
251. E. Z. GUSAKOV, N. M. KAGANSKAYA, M. KRAEMER, and V. L. SELENIN, "Correlation Enhanced-Scattering Diagnostics of Small Scale Plasma Turbulence," *Plasma Phys. Control Fusion*, **42**, 1033 (2000).
252. A. B. ALTUKHOV, E. Z. GUSAKOV, M. A. IRZA, M. KRAMER, B. LOREANZ, and V. L. SELENIN, "Investigations of Short-Scale Fluctuations in a Helicon Plasma by Cross-Correlation Enhanced Scattering," *Phys. Plasmas*, **12**, 022310 (2005).
253. A. D. GURCHENKO et al., "Correlation Upper Hybrid Resonance Scattering Diagnostics of Small Scale Turbulence in FT-1 Tokamak," *Proc. 29th EPS Conf. Controlled Fusion and Plasma Physics*, Budapest, 2000.
254. E. Z. GUSAKOV, N. M. KAGANSKAYA, M. A. LVOV, and V. L. SELENIN, in *Proc. 1996 Int. Conf. Plasma Physics (Japan Society of Plasma Science and Nuclear Fusion Research)*, Nagoya, Japan, 1996.
255. E. Z. GUSAKOV, N. M. KAGANSKAYA, M. KRAEMER, P. MORSINCHIK, and V. L. SELENIN, "Experiments on Interferometric Enhanced Scattering in a Plasma with a Nonuniform Magnetic Field," *Tech. Phys. Lett.*, **24**, 806 (1998).
256. E. Z. GUSAKOV, N. M. KAGANSKAYA, M. KRAEMER, P. MORCINCZY, and V. L. SELENIN, "Interferometer Enhanced Scattering Diagnostics of Small-Scale Plasma Waves," *Plasma Phys. Control Fusion*, **41**, 899 (1999).
257. A. R. THOMPSON, *J. Plasma Phys.*, **5**, 225 (1971).
258. T. LEHNER, J. M. RAX, and X. L. ZOU, "Linear Mode Conversion by Magnetic Fluctuations in Inhomogeneous Magnetized Plasmas," *Europhys. Lett.*, **8**, 759 (1989).
259. F. A. HASS and D. E. EVANS, "Proposal for Measuring Magnetic Fluctuations in Tokamaks by Thomson Scattering," *Rev. Sci. Instrum.*, **61**, 3541 (1990).
260. X. L. ZOU, L. LAURENT, and J. M. RAX, "Scattering of an Electromagnetic Wave in a Plasma Close to a Cut-Off Layer. Application to Fluctuation Measurements," *Plasma Phys. Control Fusion*, **33**, 903 (1991).
261. L. VAHALA, G. VAHALA, and N. BRETZ, "Electromagnetic Wave Scattering from Magnetic Fluctuations in Tokamaks," *Phys. Fluids*, **B4**, 619 (1992).
262. L. G. BRUSKIN, A. MASE, and T. TAMANO, "Two-Dimensional Microwave Scattering by Fluctuations of Plasma Density and Magnetic Field," *Plasma Phys. Control Fusion*, **37**, 255 (1995).
263. X. L. ZOU, L. COLAS, M. PAUME, M. CHAREAU, L. LAURENT, P. DEVYNCK, and D. GRESILLON, "Internal Magnetic Turbulence Measurement in Plasma by Cross Polarization Scattering," *Phys. Rev. Lett.*, **75**, 1090 (1995).
264. L. COLAS et al., "Internal Magnetic Fluctuations and Electron Heat Transport in the TORE SUPRA Tokamak: Observation by Cross-Polarization Scattering," *Nucl. Fusion*, **38**, 903 (1998).
265. Y. KOGI et al., "Cross-Polarization Scattering from Low-Frequency Electromagnetic Waves in the GAMMA-10 Tandem Mirror," *Rev. Sci. Instrum.*, **70**, 991 (1999).
266. E. Z. GUSAKOV, "Theory of Cross-Polarization Scattering from Magnetic Fluctuations in the Upper Hybrid Resonance," *Proc. 25th EPS Conf. Controlled Fusion and Plasma Physics*, Prague, 1998.
267. D. G. BULYGINSKIY et al., "Observation of Cross Polarization Scattering in the Upper Hybrid Resonance and New Possibilities for Tokamak Magnetic Turbulence Diagnostics," *Proc. 25th Conf. Controlled Fusion and Plasma Physics*, Prague, 1998.
268. A. D. GURCHENKO, E. Z. GUSAKOV, M. M. LARIONOV, K. M. NOVIK, V. L. SELENIN, and A. YU. STEPANOV, "Experiments on Cross-Polarization Scattering in the Upper Hybrid Resonance Region," *Plasma Phys. Report*, **31**, 521 (2005).
269. E. E. SALPETER, *Phys. Rev.*, **1**, 1528 (1960).
270. M. N. ROSENBLUTH and N. ROSTOKER, *Phys. Fluids*, **5**, 776 (1962).
271. N. ROSTOKER and M. N. ROSENBLUTH, "Test Particles in a Completely Ionized Plasma," *Phys. Fluids*, **3**, 1 (1960).
272. A. G. SITENKO and Y. A. KIROCHKIN, *Sov. Phys. Uspekhi*, **9**, 430 (1966).
273. R. E. AAMODT and D. A. RUSSELL, *Nucl. Fusion*, **32**, 745 (1992).
274. S. C. CHIU, *Phys. Fluids B.*, **3**, 1374 (1991).
275. A. G. SITENKO, *Fluctuations and Non-Linear Wave Interactions in Plasma*, Academic Press, New York (1982).
276. Y. L. KLIMONTOVICH, *Kinetic Theory of Nonideal Gases and Nonideal Plasmas*, Pergamon Press, Oxford (1982).
277. H. BINDSLEV, J. A. HOEKZEMA, J. EGEDAL, J. A. FESSEY, T. P. HUGHES, and J. S. MACHUZAK, *Phys. Rev. Lett.*, **83**, 3206 (1999).
278. S. MICHELSEN et al., "Fast Ion Millimeter Wave Collective Thomson Scattering Diagnostics on TEXTOR and ASDEX Upgrades," *Rev. Sci. Instrum.*, **75**, 10, 3634 (2004).

279. H. BINDSLEV et al., "Fast-Ion Dynamics in the TEXTOR Tokamak Measured by Collective Thomson Scattering," *Phys. Rev. Lett.*, **97**, 205005 (2006).
280. H. BINDSLEV et al., *Rev. Sci. Instrum.*, **75**, 3598 (2004).
281. F. MEO et al., "Design of the Collective Thomson Scattering Diagnostic for International Thermonuclear Experimental Reactor at the 60 GHz Frequency Range," *Rev. Sci. Instrum.*, **75**, 3585 (2004).
282. J. EGEDAL, H. BINDSLEV, R. V. BUDNY, and P. WOSKOV, "Impact of Beam Ions on  $\alpha$ -Particle Measurements by Collective Thomson Scattering in ITER," *Nucl. Fusion*, **45**, 191 (2005).
283. H. Z. CUMMINS and H. L. SWINNEY, *Progress in Optics*, North-Holland, Amsterdam (1970).
284. T. BLACKMAN and J. W. TUKEY, *The Measurement of Power Spectra*, Dover, New York (1959).
285. K. L. BOWLES, "Vertical-Incidence Scatter from the Ionosphere at 41 Mc/sec," *Phys. Rev. Lett.*, **1**, 454 (1958).
286. R. BEHN et al., *Phys. Rev. Lett.*, **62**, 2833 (1989).
287. P. WOSKOBONIKOW, "Development of Gyrotrons for Plasma Diagnostics," *Rev. Sci. Instrum.*, **57**, 8, 2113 (1986).
288. H. BINDSLEV, *Rev. Sci. Instrum.*, **70**, 1093 (1999).
289. R. J. UMSTATTD, C. W. DOMIER, N. C. LUHMANN, Jr., and B. I. COHEN, "A Four Wave Mixing Based Diagnostic for Confined Alpha Particles," *Bull. Am. Phys. Soc.* (1996).
290. R. J. UMSTATTD, C. W. DOMIER, N. C. LUHMANN, Jr., and B. I. COHEN, "An Optical Mixing Based Confined Alpha Particle Diagnostic," *Rev. Sci. Instrum.*, **68**, 439 (1997).
291. H. BINDSLEV, F. MEO, and S. B. KORSHOLM, "ITER Fast Ion Collective Thomson Scattering Feasibility Study and Conceptual Design" (2003).
292. G. W. WATSON and W. W. HEIDBRINK, "Density Interferometer Using the Fast Alfvén Wave," *Rev. Sci. Instrum.*, **74**, 1605 (2003).
293. H. IZEKI, R. I. PINSKER, S. C. CHIU, and J. S. DE GRASSIE, "Fast Wave Propagation Studies in the DIII-D Tokamak," *Phys. Plasmas*, **3**, 2306 (1996).
294. H. IZEKI, J. S. DE GRASSIE, R. I. PINSKER, and R. T. SNIDER, "Plasma Mass Density, Species Mix, and Fluctuation Diagnostics Using a Fast Alfvén Wave," *Rev. Sci. Instrum.*, **68**, 478 (1997).
295. G. W. WATSON, W. W. HEIDBRINK, K. H. BURRELL, and G. J. KRAMER, "Plasma Species Mix Diagnostic Using Ion-Ion Hybrid Layer Reflectometry," *Plasma Phys. Control Fusion*, **46**, 471 (2004).
296. W. W. HEIDBRINK, G. W. WATSON, and K. H. BURRELL, "Ion Species Mix Measurements in DIII-D and International Thermonuclear Experimental Reactor Using Ion-Ion Hybrid Layer Reflectometry," *Rev. Sci. Instrum.*, **75**, 3862 (2004).
297. J. A. SNIPES, D. SCHMITTDIEL, A. FASOLI, R. S. GRANETZ, and R. R. PARKER, "Initial Active MHD Spectroscopy Experiments Exciting Stable Alfvén Eigenmodes in Alcator C-Mod," *Plasma Phys. Control Fusion*, **46**, 611 (2004).
298. D. D. TESTA, A. FASOLI, and E. SOLANO, "Diagnosis and Study of Alfvén Eigenmodes Stability in JET," *Rev. Sci. Instrum.*, **74**, 1694 (2003).
299. J. CANDY et al., *Phys. Plasmas*, **6**, 1822 (1999).
300. Z. LIN, T. S. HAHM, W. W. LEE, W. M. TANG, and R. B. WHITE, "Transport Reduction by Zonal Flows: Massively Parallel Simulations," *Science*, **281**, 1835 (1998).
301. W. PARK et al. in *Proc. 16th Int. Conf. Fusion Energy*, Montreal, 1996, IAEA.
302. E. MAZZUCATO, "Microwave Imaging Reflectometry for the Visualization of Turbulence in Tokamaks," *Nucl. Fusion*, **41**, 203 (2001).
303. N. J. LOPES CARDOZO et al., "Instrumentation for Magnetically Confined Fusion Plasma Diagnostics," *Rev. Sci. Instrum.*, **55**, 279 (1994).
304. A. J. H. DONNÉ, "New Physics Insights Through Diagnostics Advances," *Plasma Phys. Control Fusion*, **48**, 12B, B483 (2006).
305. B. H. DENG et al., "ECE Imaging of Electron Temperature and Electron Temperature Fluctuations," *Rev. Sci. Instrum.*, **72**, 301 (2001).
306. B. H. DENG, D. L. BROWER, G. CIMA, C. W. DOMIER, N. C. LUHMANN, Jr., and C. WATTS, "Mode Structure of Turbulent Electron Temperature Fluctuations in the Texas Experimental Tokamak Upgrade," *Phys. Plasmas*, **5**, 4117 (1998).
307. B. H. DENG, "Electron Cyclotron Emission Imaging Diagnostics of  $T_e$  Profiles and Fluctuations," *Phys. Plasmas*, **8**, 5, 2163 (2001).
308. V. BRAVENEC and A. J. WOOTTON, "Effects of Limited Spatial Resolution on Fluctuations Measurements," *Rev. Sci. Instrum.*, **66**, 802 (1995).
309. R. P. HSIA, B. H. DENG, W. R. GECK, C. LIANG, C. W. DOMIER, and N. C. LUHMANN, Jr., "Hybrid ECE Imaging Array System for TEXT-U," *Rev. Sci. Instrum.*, **68**, 488 (1997).
310. B. H. DENG et al., "Electron Cyclotron Emission Imaging Diagnostic System for Rijnhuizen Tokamak Project," *Rev. Sci. Instrum.*, **70**, 998 (1999).
311. B. H. DENG, C. W. DOMIER, N. C. LUHMANN, Jr., A. J. H. DONNÉ, and M. J. VAN DE POL, "Electron Cyclotron Emission Imaging Diagnostic on TEXTOR," *Rev. Sci. Instrum.*, **72**, 368 (2001).
312. A. MASE et al., "ECE-Imaging Work on GAMMA 10 and LHD," *Fusion Eng. Des.*, **53**, 87 (2001).
313. A. MASE et al., "Application of Millimeter-Wave Imaging System to LHD," *Rev. Sci. Instrum.*, **72**, 1, 375 (2001).
314. G. CIMA et al., "Core Temperature Fluctuations and Related Heat Transport in the Texas Experimental Tokamak-Upgrade," *Phys. Plasmas*, **2**, 3, 720 (1995).
315. B. H. DENG et al., "Imaging of Core Electron Temperature Fluctuations of Tokamak Plasmas," *IEEE Trans. Plasma Sci.*, **30**, 1, 72 (2002).
316. C. WATTS et al., "Poloidal Asymmetry and Gradient Drive in Core Electron Density and Temperature Fluctuations on the Texas Experimental Tokamak-Upgrade," *Phys. Plasmas*, **3**, 2013 (1996).
317. C. L. RETTIG et al., "Electron Temperature Fluctuation Measurements and Techniques in the DIII-D Tokamak," *Rev. Sci. Instrum.*, **68**, 484 (1997).
318. G. CIMA et al., "Fusion Energy and Design," *Proc. 7th Int. Toki Conf. Plasma Physics and Controlled Nuclear Fusion*, Toki, Japan, 1997.
319. J. A. WESSON, "Quasi-Interchange Model," *Plasma Phys. Control Fusion*, **28**, 243 (1986).
320. H. PARK et al., "Observation of the High Field Side Crash and Heat Transfer During Sawtooth Oscillation in Magnetically Confined Plasmas," *Phys. Rev. Lett.*, **96**, 19 (2006).
321. H. PARK et al., "Comparison Study of 2-D Images of Temperature Fluctuations During the Sawtooth Oscillation with Theoretical Models," *Phys. Rev. Lett.*, **96**, 19 (2006).
322. E. MAZZUCATO, "Small-Scale Density Fluctuations in the Adiabatic Toroidal Compressor," *Bull. Am. Phys. Soc.*, **20**, 1241 (1975).
323. A. E. COSTLEY, "Diagnostics for Contemporary Fusion Experiments," *Proc. Int. School of Plasma Physics*, p. 113, (ISPP-9), Piero Caldirola, 1991.

324. J. L. DOANE, E. MAZZUCATO, and G. L. SCHMIDT, "Plasma Density Measurements Using FM-CW Millimeter Wave Radar Techniques," *Rev. Sci. Instrum.*, **52**, 12 (1981).
325. E. MAZZUCATO and R. NAZIKIAN, "Microwave Reflectometry for the Study of Density Fluctuations in Tokamak Plasmas," *Plasma Phys. Control Fusion*, **33**, 261 (1991).
326. E. MAZZUCATO and R. NAZIKIAN, "Scale Length of Turbulent Fluctuations in the Main Core of TFTR Plasmas," *Phys. Rev. Lett.*, **71**, 1840 (1993).
327. B. I. COHEN, B. B. AFEYAN, A. E. CHOU, and N. C. LUHMANN, Jr., "Computation Study of Ultra-Short-Pulse Reflectometry," *Plasma Phys. Control Fusion*, **37**, 329 (1995).
328. E. MAZZUCATO et al., "Turbulent Fluctuations in TFTR Configurations with Reversed Magnetic Shear," *Phys. Rev. Lett.*, **77**, 15, 3145 (1996).
329. G. VAYAKIS et al., "Status and Prospects for MM-Wave Reflectometry in ITER," Fusion Special Issue *Nucl. Fusion*, **46**, S836 (2006).
330. E. MAZZUCATO et al., "Fluctuation Measurements in Tokamaks with Microwave Imaging Reflectometry," *Phys. Plasmas*, **9**, 5, 1955 (2002).
331. T. MUNSAT et al., "Microwave Imaging Reflectometer for TEXTOR," *Rev. Sci. Instrum.*, **74**, 1426 (2003).
332. H. PARK et al., "Characteristics of the Textor Microwave Imaging Reflectometry System," *Proc. 29th EPS Conf. Plasma Physics and Controlled Fusion*, Montreux, Switzerland, 2002.
333. T. MUNSAT, E. MAZZUCATO, H. PARK, C. W. DOMIER, N. C. LUHMANN, Jr., A. J. H. DONNÉ, and M. VAN DE POL, "Laboratory Characterization of an Imaging Reflectometer System," *Plasma Phys. Control Fusion*, **45**, 4, 469 (2003).
334. T. DE GRAAUW and F. P. HELMICH, "Herschel-HIFI: The Heterodyne Instrument for the Far Infrared," *Proc. Symp. "The Promise of the Herschel Space Observatory"*, Toledo, Spain, 2001.
335. S. YAMAGUCHI, Y. NAGAYAMA, S. PAVLICHENKO, Y. INAGAKI, Y. KOGI, and A. MASE, "Microwave Imaging Reflectometry in LHD," *Rev. Sci. Instrum.*, **77**, 10E930 (2006).
336. P. SIEGEL, R. R. J. DENGLER, and J. C. CHEN, *IEEE Microwave and Guided Wave Lett.*, **1**, 8 (1991).
337. H. H. JAVADI and P. H. SIEGEL, "JPL New Technology Report," pp. 1–8, JPL (2001).
338. G. S. LEE et al., "Design and Construction of the KSTAR Tokamak," *Nucl. Fusion*, **41**, 1515 (2001).
339. Y.-K. OH, "Status of the KSTAR Project," *Proc. KPS 2006 Fall Symp.*, Exco, Daegu, Korea, 2006.
340. C. SOZZI et al., "The Multichannel Extension of the Martin-Puplett Interferometer for Perpendicular and Oblique ECE Measurements on Jet," *Proc. 14th Joint Workshop Electron Cyclotron Emission and Electron Cyclotron Resonance Heating (EC-14)*, Santorni, Greece, 2006.
341. I. MEHDI, E. SCHLECHT, G. CHATTOPADHYAY, and P. H. SIEGEL, "THz Local Oscillator Sources," *Proc. Far-Infrared and Submillimeter and Millimeter Detector Technology Workshop*, Monterey, California, 2002.
342. R. GAIER et al., "Amplifier Technology for Astrophysics," *Proc. Far-Infrared and Submillimeter and Millimeter Detector Technology Workshop*, Monterey, California, 2002.
343. P. H. SIEGEL, "THz Technology," *IEEE Trans. Microwave Theory Techniques*, **50**, 3, 910 (2002).
344. "Task on ITER Reflectometry," CIEMAT (2005).
345. E. MAZZUCATO, "Microwave Imaging Reflectometry for the Measurement of Turbulent Fluctuations in Tokamaks," *Plasma Phys. Control Fusion*, **46**, 1271 (2004).
346. G. J. KRAMER, R. NAZIKIAN, and E. J. VALEO, "Simulation of Optical and Synthetic Imaging Using Microwave Reflectometry," *Plasma Phys. Control Fusion*, **46**, 695 (2004).
347. "ITER Design Description Document Diagnostics, 5.5.F Microwave," DDD 5.5F, N 55 DDD 6 01-06-01 W 0.3, ITER.